AGU PUBLICATIONS

Geochemistry, Geophysics, Geosystems

RESEARCH ARTICLE

10.1002/2014GC005570

Key Points:
- Abbot Ice Shelf is underlain by E-W rift basins created at ~90 Ma
- Amundsen shelf shaped by subsidence, sedimentation, and passage of the ice sheet
- Bellingshausen plate boundary is located near the base of continental slope and rise

Correspondence to:
J. R. Cochran,
jrc@ldeo.columbia.edu

Citation:
Cochran, J. R., K. J. Tinto, and R. E. Bell (2015), Abbot Ice Shelf, structure of the Amundsen Sea continental margin and the southern boundary of the Bellingshausen Plate seaward of West Antarctica, *Geochem. Geophys. Geosyst.*, *16*, 1421–1438, doi:10.1002/2014GC005570.

Received 5 SEP 2014
Accepted 9 APR 2015
Accepted article online 15 APR 2015
Published online 22 MAY 2015

The copyright line for this article was changed on 5 JUN 2015 after original online publication.

Abbot Ice Shelf, structure of the Amundsen Sea continental margin and the southern boundary of the Bellingshausen Plate seaward of West Antarctica

James R. Cochran[1], Kirsty J. Tinto[1], and Robin E. Bell[1]

[1]Lamont-Doherty Earth Observatory of Columbia University, Palisades, New York, USA

Abstract Inversion of NASA Operation IceBridge airborne gravity over the Abbot Ice Shelf in West Antarctica for subice bathymetry defines an extensional terrain made up of east-west trending rift basins formed during the early stages of Antarctica/Zealandia rifting. Extension is minor, as rifting jumped north of Thurston Island early in the rifting process. The Amundsen Sea Embayment continental shelf west of the rifted terrain is underlain by a deeper, more extensive sedimentary basin also formed during rifting between Antarctica and Zealandia. A well-defined boundary zone separates the mildly extended Abbot extensional terrain from the deeper Amundsen Embayment shelf basin. The shelf basin has an extension factor, β, of 1.5–1.7 with 80–100 km of extension occurring across an area now 250 km wide. Following this extension, rifting centered north of the present shelf edge and proceeded to continental rupture. Since then, the Amundsen Embayment continental shelf appears to have been tectonically quiescent and shaped by subsidence, sedimentation, and the advance and retreat of the West Antarctic Ice Sheet. The Bellingshausen Plate was located seaward of the Amundsen Sea margin prior to incorporation into the Antarctic Plate at about 62 Ma. During the latter part of its independent existence, Bellingshausen plate motion had a clockwise rotational component relative to Antarctica producing convergence across the north-south trending Bellingshausen Gravity Anomaly structure at 94°W and compressive deformation on the continental slope between 94°W and 102°W. Farther west, the relative motion was extensional along an east-west trending zone occupied by the Marie Byrd Seamounts.

1. Introduction

The Bellingshausen Sea and Amundsen Sea continental margins of West Antarctica (Figure 1) have developed in very different manners. The Bellingshausen margin, east of 90°W–95°W, was a convergent margin throughout much of the Mesozoic with oceanic crust subducting beneath Antarctica [e.g., *Suarez*, 1976; *Pankhurst*, 1982; *Leat et al*., 1995]. Through the Cenozoic, segments of the Antarctic-Phoenix Ridge have successively collided with the subduction zone, beginning near 85°W and proceeding northeast along the Antarctic Peninsula [*Herron and Tucholke*, 1976; *Barker*, 1982]. As each section of the ridge axis reached the trench, both spreading and subduction ceased in that segment and the margin became passive. In contrast, the Amundsen Sea continental margin, west of 90°W–95°W, is a rifted continental margin formed by continental rifting and the separation of Zealandia (Chatham Rise and the Campbell Plateau) from Antarctica beginning at about 90 Ma [e.g., *Larter et al*., 2002; *Eagles et al*., 2004a, 2004b]. The difference in the origin of the two sectors is reflected in seafloor spreading magnetic anomalies that become younger away from the Amundsen margin, while anomalies seaward of the Bellingshausen margin become younger toward the margin (Figure 1).

The Amundsen continental margin may also have been impacted by interactions between the Antarctic Plate and the Bellingshausen Plate, a region of seafloor extending from the ridge axis toward the Antarctic margin which moved independently of the Antarctic Plate from ~83 to ~61 Ma [*Stock and Molnar*, 1987; *Cande et al*., 1995]. The nature and location of the Bellingshausen Plate's southern boundary is uncertain. Suggestions for this boundary's location range from within the oceanic crust seaward of the margin to well up onto the Amundsen continental shelf [*Stock et al*., 1996; *Larter et al*., 2002; *Wobbe et al*., 2012; *Gohl et al*., 2013a].

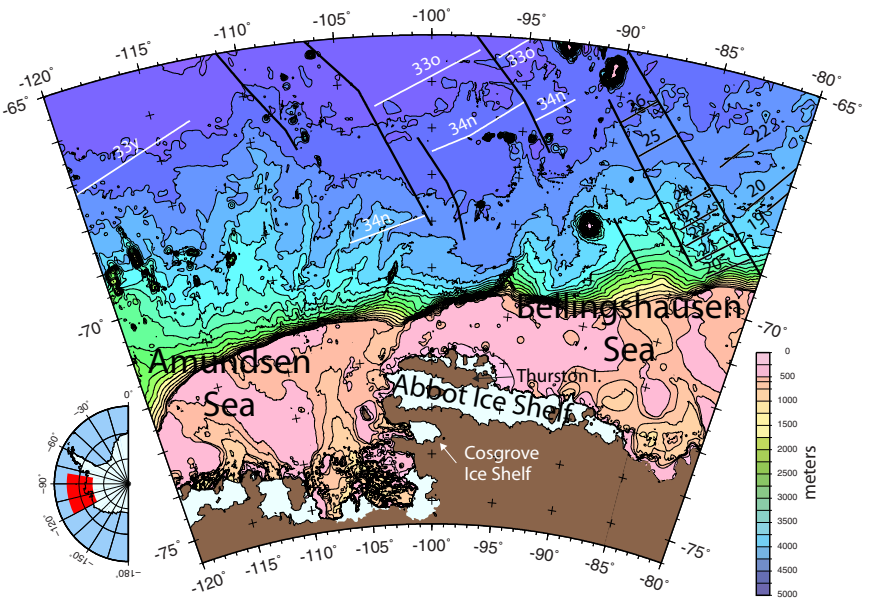

Figure 1. Bathymetric map of the Antarctic continental margin in the region near the Abbot Ice Shelf showing seafloor spreading magnetic anomalies and fracture zones. Magnetic anomalies generated at the Bellingshausen-Pacific Ridge following rifting between Zealandia and Antarctica are shown in white. Magnetic anomalies generated at the now subducted Antarctic-Phoenix Ridge are shown in black. Fracture zones and marine magnetic anomaly correlations are from *Cande et al*. [1982] and *Larter et al*. [2002]. Bathymetry is from the International Bathymetric Chart of the Southern Oceans (IBCSO) [*Arndt et al*., 2013]. Color scale for bathymetry is shown on right. Inset on left shows location on the West Antarctic coast.

The Abbot Ice Shelf extends for 450 km along the coast of West Antarctica between 103°W and 89°W, straddling the boundary between the Bellingshausen and Amundsen continental margins (Figure 1). Thurston Island bounds the northern side of the ice shelf to the west of 95°30′W. The eastern portion of the ice shelf opens onto the Bellingshausen Sea continental shelf between several small islands, while the western edge faces the Amundsen Sea Embayment (Figure 1). Numerous islands and ice rises suggest a complex bathymetry beneath the Abbot.

Cochran et al. [2014] carried out an inversion of NASA Operation IceBridge airborne gravity data over the Abbot Ice shelf (Figure 2) for bathymetry and investigated the implications of their results for ocean/ice interactions and the stability of the ice shelf. Here we will use the bathymetry obtained from the inversion, which indicates that the western half of the ice shelf overlies a fault-bounded extensional terrain, along with existing geophysical observations from the West Antarctic margin, to investigate the structure of the Amundsen Sea continental margin and the location and nature of the southern boundary of the former Bellingshausen Plate.

2. Bathymetry Beneath the Abbot Ice Shelf

NASA's Operation IceBridge (OIB) program obtained 10 north-south, low-altitude airborne geophysical lines across the Abbot Ice Shelf and an east-west line along the axis of the ice shelf during the 2009 OIB Antarctic campaign (Figure 2). Spacing between the north-south flights varied from 30 to 54 km with a mean separation of 39.2 km.

Instrumentation on the OIB lines included a laser altimeter [*Krabill et al*., 2002], a variety of ice-penetrating radars [*Leuschen*, 2011], and a Sander AIRGrav gravimeter [*Argyle et al*., 2000; *Sander et al*., 2004; *Cochran and Bell*, 2010]. A major advantage of the AIRGrav system over other airborne gravimeters is that it is able to collect high-quality data during draped flights [*Studinger et al*., 2008]. Flights during OIB surveys are flown at a nominal height of 1500 feet (457 m) above the Earth's surface.

Free-air gravity anomalies measured on OIB flights over the Abbot Ice Shelf are shown in map view in Figure 2. Anomalies range from 80 to −61 mGal. Large positive gravity anomalies of up to 72 mGal are consistently found over Thurston Island. Anomalies reach 77 mGal over Dustin Island, at the edge of the ice shelf

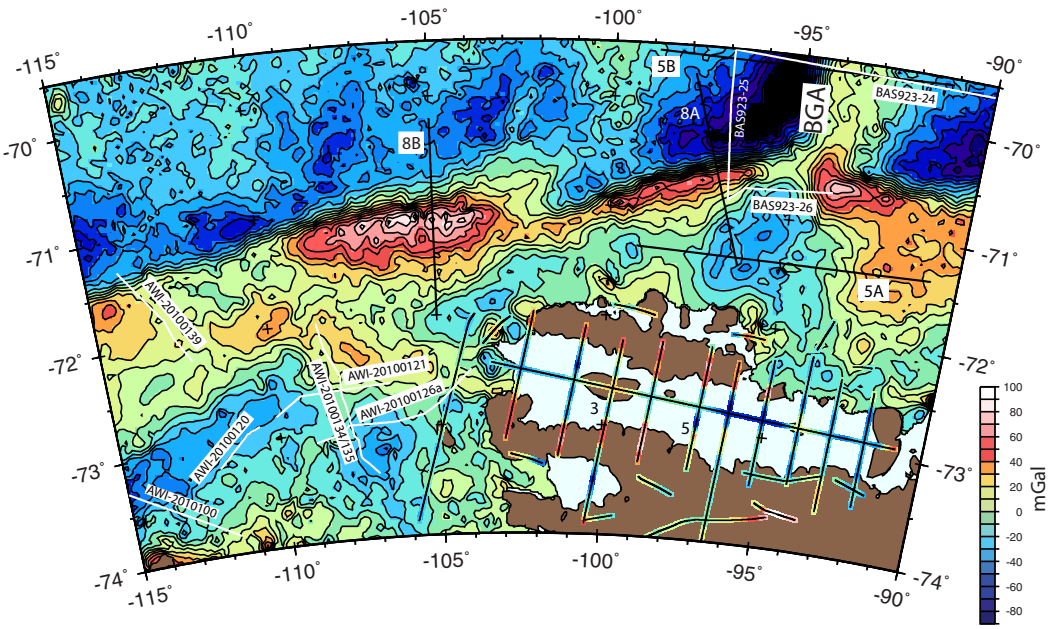

Figure 2. Free-air gravity anomalies from Operation IceBridge flights over the Abbot Ice Shelf plotted along flight lines. Gravity anomalies in offshore areas are satellite-derived free-air anomalies from *McAdoo and Laxon* [1997] contoured at 10 mGal intervals. Color scale for airborne and satellite gravity anomalies is shown on right. Numbers along the flight lines identify profiles shown in Figure 3. Black lines offshore show the location of bathymetry and gravity profiles shown in Figures 5 and 8. White lines show the location of BAS and AWI seismic lines [*Larter et al.*, 1999; *Cunningham et al.*, 2002; *Gohl et al.*, 2013b] discussed in the text. BGA is Bellingshausen Gravity Anomaly.

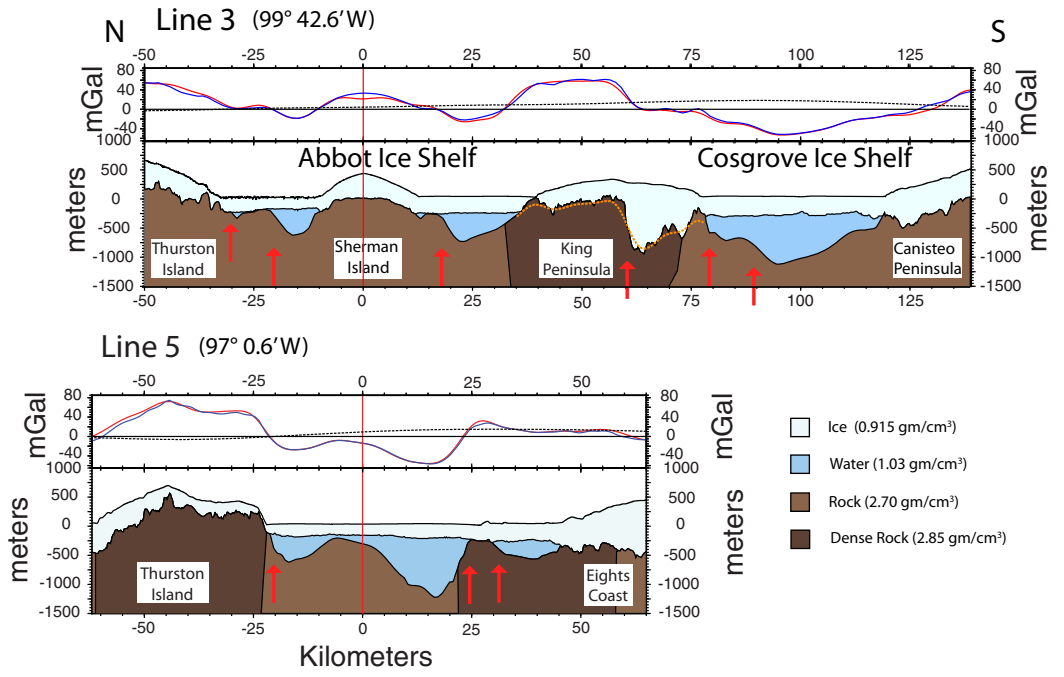

Figure 3. Airborne geophysical lines 3 and 5 from *Cochran et al.* [2014] across Abbot and Cosgrove ice shelves. Location of profiles is shown in Figure 2. For each profile, the top panel shows the observed free-air gravity in red and the anomaly predicted by the inversion in blue. Bottom panels show the observed upper and lower ice surfaces from laser altimeter and radar measurements, respectively, and the upper surface of the solid Earth. Where ice is grounded, the Earth's surface is determined from radar measurements. Where ice is floating, the bathymetry is determined from inversion of gravity anomalies. Vertical red lines show where the profile crosses the line flown along the axis of the ice shelf (Figure 2). The longitude of that location is noted. Red arrows show the location of faults mapped in Figure 4. Note that actual faults will be steeper than shown here because of the filter applied to the gravity data. The orange dashed line shows the results of filtering the bed imaged by radar beneath the King Peninsula with a 9.8 km filter, which is the spatial equivalent of the 70 s filter applied to the gravity data. The dashed line in the top panel of each profile shows the gravity effect of Moho relief when the shallow structure is assumed to be locally compensated.

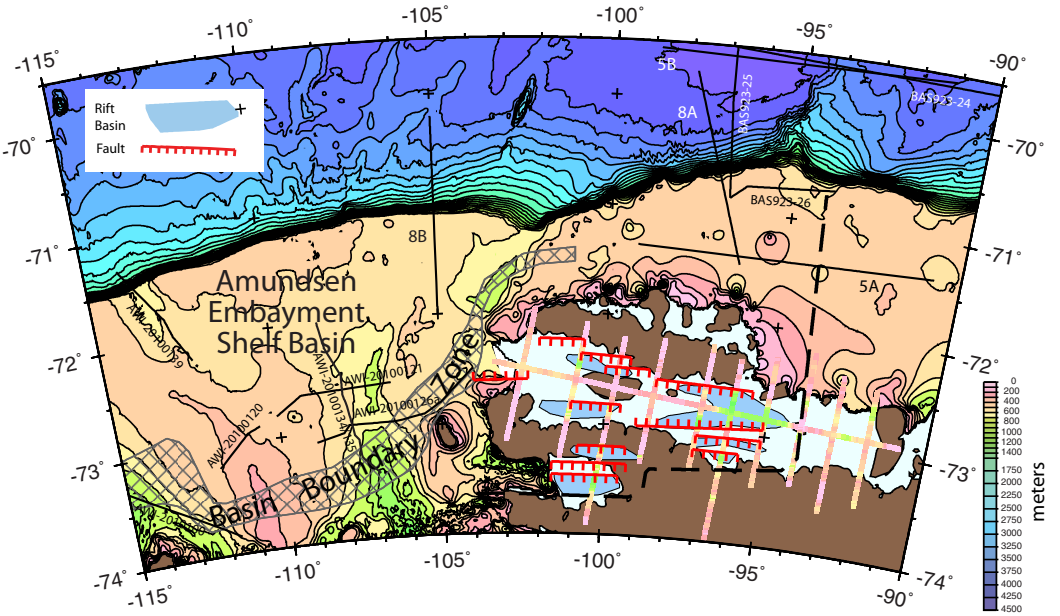

Figure 4. Basins, faults, and the spatial extent of rifting under Abbot and Cosgrove ice shelves from inversion of Operation IceBridge gravity data. Gravity-derived bathymetry and radar-determined bed are shown along flight lines. Offshore marine bathymetry is from the International Bathymetric Chart of the Southern Oceans (IBCSO) [*Arndt et al*., 2013] contoured at 100 m intervals to 1500 and 250 m intervals for greater depths. Heavy dashed black line shows the limit of rifting beneath Abbot and Cosgrove ice shelves. Cross-hatched area shows the basin boundary zone separating exposed or lightly sedimented basement from a deep, thickly sedimented basin. Black lines offshore show the location of bathymetry and gravity profiles shown in Figures 5 and 8 and the location of BAS and AWI seismic lines [*Larter et al*., 1999; *Cunningham et al*., 2002; *Gohl et al*., 2013b] discussed in the text.

immediately east of Thurston Island, and positive anomalies are found at the other islands (Sherman, Johnson, and Farwell) flown over within the Abbot. An east-west band of large positive anomalies with maximum amplitudes of 50–80 mGal also extends along the King Peninsula on the mainland. This band of positive gravity extends offshore into the ice shelf east of 98°W with a reduced amplitude and dies out near 94°E. The rest of the ice shelf is characterized by negative free-air anomalies, generally in the range of −15 to −35 mGal. Southeast of Thurston Island, large negative anomalies of −55 to −60 mGal are found over the northern and central part of the ice shelf from 97°W to 94.5°W.

Cochran et al. [2014] undertook an inversion of the gravity data for bathymetry beneath the ice shelf in two dimensions along individual flight lines using Geosoft GMSys^{TM} software. The software does iterative forward modeling using the technique of *Talwani et al*. [1959]. Laser altimeter and radar data obtained on the same flight as the gravity were used to define the surface and base of the ice. The bed was kept fixed where it is observed in the radar data, while the bathymetry in water-covered areas (where the seafloor cannot be imaged with radar) was varied to obtain the best match to the observed gravity. *Cochran et al*. [2014] discuss the inversion and the geologic data used to constrain densities in great detail. They also show profiles of the results along each flight line. We show profiles along two lines, one (Line 3) over the western portion of the ice shelf and one (Line 5) over its central portion, in Figure 3 and all of the results in map form in Figure 4.

It is difficult to quantify the uncertainty in the bathymetry determinations. Estimates for the uncertainty of two-dimensional inversions along flight lines, based on comparison with known bathymetry and crossings with other lines, range from ±50 to ±100 m depending on the distance from constraints [e.g., *Tinto and Bell*, 2011]. A three-dimensional gravity inversion, with sparse geologic constraints, for bathymetry beneath the Larsen C Ice Shelf [*Cochran and Bell*, 2012] was compared with seismic reflection data [*Brisbourne et al*., 2014] at 87 sites and a standard error of 59.0 m was determined [*Cochran et al*., 2014].

Cochran et al. [2014] did not include a sediment layer in their inversion. A simple Bouguer slab calculation implies that each 100 m of sediment with density 2.2 g/cm^3 will lead to a seafloor depth overestimate of ∼30 m. Depths obtained from the inversion will lie between the actual seafloor and crystalline basement

depths [*Cochran et al*., 2014]. This will affect the modeled water depth, but not the shape of the basins or our interpretation of their tectonic origin.

The inversion software adjusts a single surface, in this case the rock-water interface, to obtain the best possible match between the observed and calculated gravity anomalies. It therefore assumes a flat Moho. The gravity effect along the airplane trajectory of Moho relief assuming local compensation of the two profiles in Figure 3 is shown as a dashed line on the gravity panel of each line. The calculation assumes that an unloaded (no ice) crustal section at sea level has a thickness of 27 km. The relative narrowness of the individual basins, combined with the effects of upward continuation to the flight altitude, results in the gravity effect of Moho relief beneath the basins merging into a very broad low anomaly reaching a maximum amplitude of ~18 mGal over the Cosgrove Ice Shelf on Line 3 and ~15 mGal over the southern Abbot on Line 5. The very broad nature of the Moho gravity effect means that the shape and amplitude of the gravity anomaly over the individual basins results primarily from the shallow structure and thus that the Moho relief will have minimal effect on the bathymetry resulting from the inversion.

Also, extensive geophysical study of the East African Rift System has shown that early stage continental rifts are not locally compensated. Rather, the faults bounding these asymmetric rifts are listric, curving with depth to sole out in a ductile lower crust [e.g., *Rosendahl*, 1987; *Morley et al*., 1992; *Lambiase and Bosworth*, 1995; *Karner et al*., 2000]. As a result, crustal extension and thinning is spread over an area extending beyond the surface rift basin resulting in a broader and lower Moho signal than shown in Figure 3.

3. Tectonic Setting of the Abbot Ice Shelf

The bathymetry beneath the ice shelf to the west of ~98°W (Figure 3, Line 3), determined from inversion of the OIB gravity data, consists of a series of east-west trending basins. These basins are asymmetric with a steep slope bounding one side and we interpret them as fault-bounded half grabens (Figures 3 and 4). Our interpretation of an extended terrain beneath the Abbot Ice Shelf is supported by the observation that the OIB airborne radar images a deep, asymmetric basin under the King Peninsula that appears fault bounded on the north and takes the form of a half graben (Figure 3, Line 3). The northern wall of that basin is steeper than the walls of the gravity-delineated basins, but the gravity-determined slopes are reduced as a result of the 70 s filter applied to the gravity data. If we filter the radar-determined bed with the spatial equivalent of the gravity filter, the basin on the King Peninsula has slopes very similar to those in the basins identified from the gravity inversion (Figure 3, Line 3).

Faults and basins identified from the gravity modeling are shown in Figure 4. The southern margin of Thurston Island is bounded by an en echelon set of faults. In the western portion of the ice shelf, the structure takes the form of a series of south-facing half grabens forming 10–20 km wide topographic basins. This pattern continues south across the King Peninsula to the Cosgrove Ice Shelf, which also appears to be underlain by a half graben (Figure 3, Line 3).

East of about 98°, the tectonic pattern under the ice shelf changes to a broad 1200 m deep basin bounded by inward-facing faults (Figure 3, Line 5). Shallower small, fault-bounded basins are located along the southern margin of the ice shelf. The footwalls of the faults bounding these basins on the north form linear ridges associated with changes in ice thickness and/or create linear rows of ice rises and ice rumples on the ice shelf surface (Figure 3, Line 5) [*Cochran et al*., 2014]. Extension in this area does not extend south of the Abbot Ice Shelf as it does farther west.

A possible alternative explanation for the basins beneath the Abbot Ice Shelf is that they are erosional features carved out by an advancing ice sheet. Broad, deep troughs have been imaged beneath many of the major ice streams of Antarctica [e.g., *Ross et al*., 2012; *Wright et al*., 2014; *Fricker et al*., 2014]. These troughs extend across the continental shelf seaward of the present edge of the ice sheet toward the shelf break [e.g., *Wellner et al*., 2001, 2006; *Nielsen et al*., 2005; *Nitsche et al*., 2007].

However, there are a number of observations that imply that the basins underlying the Abbot and Cosgrove ice shelves did not form in this manner. First, there are no significant ice streams feeding into either the Abbot or Cosgrove ice shelves [*Swithinbank et al*., 2004]. Also, the asymmetric shape of the basins is not typical of glacial troughs, but is diagnostic of tectonically formed half grabens. The asymmetric nature of the

gravity-inferred basins is supported by the extremely asymmetric nature of the basin imaged by radar beneath the King Peninsula (Figure 3).

In addition, the very linear nature of the E-W-trending sets of ice rises in the southern Abbot between 98°W and 94°W is much more characteristic of tectonic activity than erosion. We interpret them as resulting from the impingement of the footwall rims of half graben basins onto the base of the ice shelf. In addition, these small closed basins are perpendicular to the flow of ice into the Abbot ice shelf from the mainland and do not feed into the deeper main basin to the north, as they would if they were erosional features.

Our interpretation of the Abbot basins as formed by rifting is also supported the presence of east-west oriented intrusive dikes on southern Thurston Island [e.g., *Storey et al*., 1991; *Leat et al*., 1993], implying north-south extension.

The last known igneous event on Thurston Island was the emplacement of a suite of E-W trending, coast-parallel dikes [e.g., *Storey et al*., 1991; *Leat et al*., 1993]. These dikes were intruded prior to about 90 Ma [*Leat et al*., 1993] into 120–155 Ma plutonic rocks [*Grunow et al*., 1991] and imply north-south regional extension during that time interval. Rifting between Zealandia and Antarctica began shortly before 90 Ma with north-south extension [*Larter et al*., 2002; *Eagles et al*., 2004a]. The extensional terrain identified beneath the Abbot Ice Shelf to the west of 94°W thus appears to be a rift active at the time of that opening.

The extensional terrain ends abruptly near 94°W at Johnson Island. The bathymetry inferred beneath the ice shelf on Lines 9 and 10, located east of 94°W between Johnson and Farwell Islands, is shallower with gentler slopes and shows no features suggesting an eastward continuation of the basins underlying the western portion of the ice shelf (Figure 4) [*Cochran et al*., 2014].

4. Structure of the Amundsen Sea Continental Margin

The abrupt eastern end of the rifted terrain beneath the ice shelf at 94°W coincides with the change from a former subduction continental margin toward the east to a rifted continental margin toward the west. The 94°W boundary of the rifted terrain is aligned with a prominent linear north-south-trending feature in the satellite gravity field. This offshore lineation extends from 61°S to the continental margin [*McAdoo and Marks*, 1992; *McAdoo and Laxon*, 1997] and separates northward-younging seafloor spreading magnetic anomalies created by the separation of Zealandia and Antarctica from southward-younging anomalies created at the now subducted Phoenix-Antarctic ridge [e.g., *Weissel et al*., 1977; *Mayes et al*., 1990; *McCarron and Larter*, 1998; *Larter et al*., 2002] (Figure 1). The southernmost portion of the lineation was named the Bellingshausen Gravity Anomaly (BGA) by *Gohl et al*. [1997a] (Figure 2).

Prior to the rifting of Zealandia off Antarctica, the BGA lineation was a portion of a Cretaceous ridge-trench transform separating the Charcot Plate and the Pacific Plate [*Eagles et al*., 2004a]. Rifting nucleated along the transform at about 90 Ma, perhaps at an intratransform spreading center [*Bird and Naar*, 1994] or by propagation of the Charcot-Pacific Ridge across the transform. This rifting propagated westward, splitting Chatham Rise and Campbell Plateau off Antarctica [*Larter et al*., 2002; *Eagles et al*., 2004a].

The mid-Cretaceous rift terrain beneath the present Abbot Ice Shelf to the west of 94°W implies that the rifting initially extended southward into the present Antarctic continent. After a limited amount of extension south of Thurston Island, rifting centered north of the island where it led to lithospheric rupture and the establishment of a spreading center.

The eastern boundary of rifting at 94°W can be traced across the continental shelf north of the Abbot Ice Shelf as a gradient in the free-air gravity anomalies from higher anomalies in the east to lower in the west (Figures 2 and 5a). Figure 5a shows a simple model of a bathymetry and gravity profile on the continental shelf near 71°30′S. Bathymetry is from IBCSO [*Arndt et al*., 2013] and the gravity anomalies are from *McAdoo and Laxon* [1997]. The IBCSO grid is based on shipboard measurements and is thus independent of the gravity data, which comes from satellite altimetry. Sediment depth at the eastern end of the profile is constrained by faint "basement" reflectors identified on seismic line BAS923-26 along the outer continental shelf (Location shown in Figures 2 and 4) published by *Cunningham et al*. [2002]. Depth to crystalline basement in the model increases from 2.5 km in the east to a maximum of 6 km north of Thurston Island. This transition, centered near 94°W, marks the boundary from the nonrifted, formerly subducting margin in the

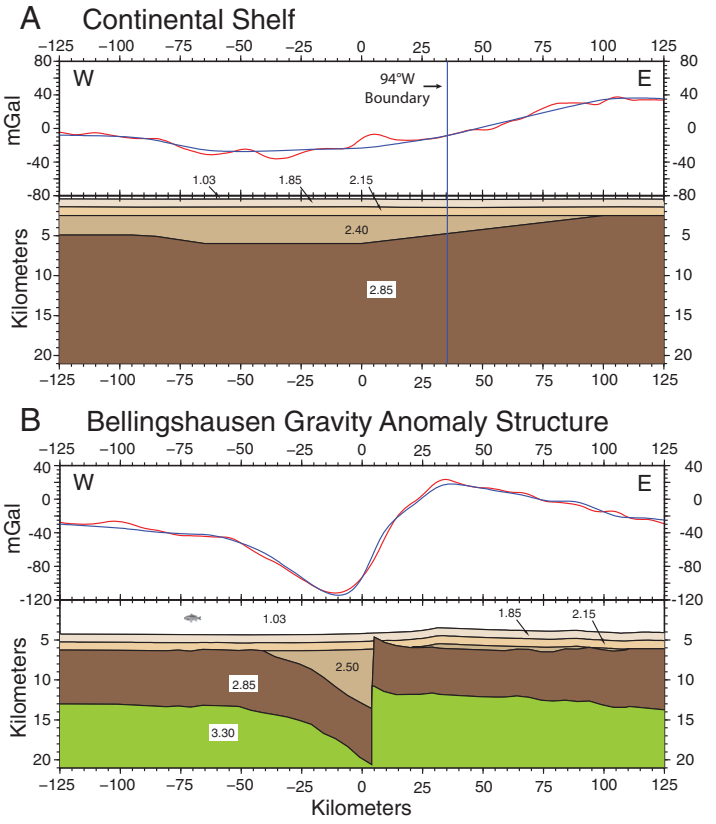

Figure 5. (a) Two-dimensional gravity model of a west-to-east bathymetry and free-air gravity profile on the continental shelf near 71°24′S. Location is shown in Figures 2 and 4. Observed gravity anomalies are in red and model anomalies are in blue. Assumed densities in g/cm^3 are shown. The model illustrates that gravity anomalies on the shelf near 95°W can be explained by a transition from relatively shallow basement in the east to deeper, rifted basement to the west. (b) Two-dimensional gravity model of a west-to-east bathymetry and free-air gravity profile across the BGA structure near 69°34′S. Location is shown in Figures 2 and 4. Depth to the top of the crust was taken from BAS seismic reflection profile BAS923-24 [*Cunningham et al*., 2002] where basement is visible on that profile. The BAS seismic profile is nearly coincident with our line (Figures 2 and 4). Observed gravity anomalies are in red and model anomalies are in blue. Assumed densities in g/cm^3 are shown. *Gohl et al*. [1997a] obtained a very similar result from modeling a shipboard seismic and gravity profile across the BGA. For both models, bathymetry is from IBCSO [*Arndt et al*., 2013] and gravity is from *McAdoo and Laxon* [1997].

east to the rifted margin in the west. The 6 km depth to basement calculated to the west of the transition is within the range observed farther west under the Amundsen Sea Embayment continental shelf [*Gohl et al*., 2013b].

A characteristic feature of the Amundsen Sea Embayment is that the inner shelf has exposed or lightly sedimented basement that deepens dramatically seaward across a zone (shown as a cross-hatched area in Figure 4) that is well defined by seismic [*Lowe and Anderson*, 2002; *Graham et al*., 2009; *Gohl et al*., 2013b] and magnetic [*Gohl et al*., 2013a] data. The boundary is marked by a prominent scarp with 2 s twtt (two-way travel time) of relief on seismic line AWI20100134/135 (Location shown in Figures 2 and 4) [*Gohl et al*., 2013b]. The landward edge of the basin boundary zone from 113°W to 107°W at ~73°40′S is aligned with the southern margin of the rift under Cosgrove Ice Shelf (Figures 4 and 7). This basin edge appears to mark the southern extent of the Cretaceous rifting related to separation between Antarctica and Zealandia and formation of the continental margin.

East of 107°W, the basin boundary zone bends to north, and separates the slightly extended crust of the Cosgrove and Abbot rifts to the east from the more highly extended and subsided crust under the Amundsen Embayment continental shelf to the west (Figure 4). This north-south portion of the shelf basin boundary zone must have served as an accommodation zone during rifting, bounding and connecting offset rift segments [e.g., *Bosworth*, 1985, 1994; *Burgess et al*., 1988; *Ebinger*, 1989a, 1989b]. The N-S offset in the boundary zone near 113°W probably is another accommodation zone separating slightly offset segments of the original rift.

Multichannel seismic (MCS) reflection lines across the continental shelf of the embayment presented by *Gohl et al*. [2013b] show ~4.5 s twtt of sediment beneath the central shelf decreasing to ~ 3.5 s twtt near the shelf break. Reflectors within the sediments show a distinct northward dip throughout the shelf. *Gohl et al*. [2013b] utilized velocity information from ocean bottom seismometer (OBS) seismic refraction lines to construct a depth transect across the continental shelf at about 108°W that shows basement at about 4.5 km below sea level near the shelf edge, increasing to a maximum of about 7 km beneath the central shelf before shallowing abruptly across the shelf basin boundary zone to outcrop in the inner shelf.

The deep basin extends westward to at least 113°W, where seismic line AWI-20100139 (location shown on Figures 2 and 4) shows 4.5 s twtt of sediment [*Gohl et al*., 2013b]. West of the possible accommodation zone at 113°W, the continental shelf becomes narrower, perhaps reflecting less crustal extension. West of 118°W, the shelf edge curves sharply to the south (Figure 1) and the continental shelf narrows to about 150 km wide west of 120°W. The western boundary of the deep Amundsen Embayment Shelf Basin thus appears to be in that region between 113°W and 120°W.

Gohl et al. [2007] utilized seismic and gravity data to produce a map of Moho depth under the Amundsen Sea Embayment. Their depth to Moho is about 24 km to the east of 112°W, decreasing to 23 km at about 115°W and 22 km in the westernmost embayment with very little north-south variation landward of the shelf break along a given longitude. *Kalberg and Gohl* [2014] discuss a seismic refraction line (AWI-2010100) in the western Amundsen Embayment (location shown in Figures 2 and 4) that determined the depth to Moho from the middle of the basin boundary zone onto the region of exposed basement and showed it to increase landward from 24 to 27 km, consistent with the gravity calculation of 22 km in the basin seaward of the seismically determined Moho depths [*Gohl et al*., 2007]. An average depth of 6 km to the top of the crystalline crust combined with the 22–24 km depth to the Moho implies a mean thickness of 16–18 km for the crust beneath the Amundsen Embayment Shelf Basin.

Winberry and Anandakrishnan [2004] and *Chaput et al*. [2014] used receiver function analyses to determine crustal thicknesses of 25–31 km beneath stations in the West Antarctica Rift System with a thinner crust of 17–25 km beneath the Ross Sea and within narrow troughs. Other published estimates of the crustal thickness onshore from the Amundsen Sea are based on gravity data and are in the range of 24–30 km [e.g., *Block et al*., 2009; *Jordan et al*., 2010; *Bingham et al*., 2012]. The gravity-based thickness estimates do not include a sediment layer. However, *Anandakrishnan and Winberry* [2004] report less than 300 m of sediment at the *Winberry and Anandakrishnan* [2004] stations, except at the Bentley Subglacial Trench, where 550 ± 150 m of sediment was noted. Other studies, using both seismic [*Anandakrishnan et al*., 1998] and gravity [*Bell et al*., 1998; *Studinger et al*., 2001] techniques have also found patchy to thin ($<\sim$300 m) sediments through most of the West Antarctic Rift System with thicker ($>$1 km) sediments in narrow (20–35 km wide) fault-bounded basins, which are often associated with the onset of ice streams. Thus, the gravity calculations also appear to represent reasonable estimates of the crystalline crust thickness.

Assuming an initial crustal thickness of 27 km consistent both with those calculations and with the seismically determined thickness just landward of the shelf basin [*Kalberg and Gohl*, 2014], the extension parameter, β [*McKenzie*, 1978], for the shelf basin varies from 1.5 to 1.7. This is a relatively modest amount of thinning, similar to that determined by *Steckler et al*. [1998] for the southern Gulf of Suez, a failed rift that was abandoned at a relatively early stage in the development of the Red Sea [e.g., *Garfunkel and Bartov*, 1977; *LePichon and Francheteau*, 1978; *Cochran*, 1983; *Bosworth and McClay*, 2001]. The width of extended crust is wider in the Amundsen Sea Embayment and thus the total amount of extension is greater. The area of extended crust under the Amundsen Sea Embayment shelf is presently about 250 km wide, so β values of 1.5–1.7 imply that about 80–100 km of extension has occurred in this region. If the prerift crustal thickness was greater, perhaps 35 km which has been inferred for the Ellsworth and Whitmore Mountains [*Studinger et al*., 2002; *Studinger and Bell*, 2007; *Jordan et al*., 2010] and for the portion of East Antarctica between the Transantarctic Mountains and Wilkes Subglacial Basin [*Ferraccioli et al*., 2001], β becomes 1.95–2.2, which is still modest compared to the thinning necessary for lithospheric rupture. *Gaulier et al*. [1988] reported a crustal thickness of 5–8 km beneath the northern Red Sea, where organized seafloor spreading is just beginning [*Cochran*, 2005]. Seismic experiments on the adjacent Arabian and Nubian shields gave crustal thicknesses of 32–44 km [e.g., *Makris et al*., 1983; *Mooney et al*., 1985; *Prodehl*, 1985; *Gettings et al*., 1986], resulting in β values of 4–8.8. After this initial episode of extension, rifting in the Amundsen Sea

Embayment jumped or centered to the north of the present shelf where the major episode of rifting and lithospheric rupture occurred.

Gohl et al. [2007, 2013a] defined NE-SW and WNW-ESE trending sets of magnetic anomalies on the continental shelf that they ascribed to magmatism accompanying continental rifting and to activity along the southern boundary of the Bellingshausen Plate, respectively. However, MCS profiles [*Gohl et al*., 2013b] show no disturbance in the sediments, including immediately above the basement where it is visible, where the profiles pass over either set of magnetic anomalies. Thus, it is unlikely that the magnetic anomalies result from tectonic events postdating the rifting. Some of the magnetic anomalies may result from structures present in the prerift basement, a Mesozoic magmatic arc complex related to the subduction zone that was north of Zealandia at that time. Similar amplitude magnetic anomalies, also subparallel to the margin, are observed along the Antarctic Peninsula [*Renner et al*., 1985; *Golynsky et al*., 2001] where they have been interpreted as arising from Cretaceous-aged intrusions into the crust [e.g., *Ferraccioli et al*., 2006; *Yegorova et al*., 2011; *Yegorova and Bakhmutov*, 2013].

Dalziel [2006], *Muller et al*. [2007], and *Eagles et al*. [2009b] all suggested that the West Antarctic Rift System (WARS) might extend to the Pacific at some location between the Amundsen Sea Embayment and the Antarctic Peninsula. *Gohl et al*. [2013a] proposed that a zone of negative magnetic anomalies extending NNE-SSW from 72°S to 73.5°S between 106°W and 108°W indicate the presence of a rift basin beneath the Amundsen Sea Embayment formed between 50 and 30 Ma as a branch of the WARS.

Gohl et al. [2013b] showed east-west seismic lines across the shelf to illustrate the proposed basin. The eastern boundary of the hypothesized basin is formed by the basin boundary zone that separates the extended and subsided crust of the continental shelf basin from the thicker, less extended crust of the Abbot Rift region (Figure 4). On *Gohl et al*.'s [2013b] seismic line AWI-20100126a (location shown on Figures 2 and 4), the deepest sediment unit (ASS-1), which they assign a Cretaceous age and consider to consist of the pre and syn-rift sediment sequence, is truncated against the flank of the basin boundary zone. Reflectors within the overlying unit (ASS-2), assigned a Late Cretaceous-Oligocene age [*Gohl et al*., 2013b], continue across the entire length of the profile and are not offset at the boundary zone. This implies that the relief of the basin boundary zone was created during rifting and that it was not reactivated by Cenozoic WARS faulting.

Gohl et al. [2013b] show a consistent pattern of northward (seaward) dip on seismic reflectors throughout the Amundsen Sea Embayment. The apparent shallowing of seismic reflectors used to define the western edge of their proposed WARS basin begins where the seismic line used to define it (AWI-20100120/AWI-20100120-121 [*Gohl et al*., 2013b]) (location shown on Figures 2 and 4) changes course to run more to the southwest rather than east-west across the basin [*Gohl et al*., 2013b]. This means that the line then runs diagonally updip on the northward-dipping reflectors, resulting in the shallowing interpreted indicating as the western rift boundary. MCS line AWI-20100139 [*Gohl et al*., 2013b] near 113°W (location shown on Figures 2 and 4), to the west of the hypothesized basin, shows ~4.5 s twtt of sediment, which is virtually identical to the thickness shown by lines within it. Thus, it is difficult to identify or delineate a NNE-SSW oriented WARS rift basin beneath the Amundsen Sea Embayment.

Bingham et al. [2012] used radar, gravity, and magnetic data to define a rifted basin 500–600 km to the east of the Amundsen Sea Embayment. This Ferrigno Rift appears a more likely continuation of the WARS toward the continental margin in the Bellingshausen Sea, where it may have intersected with the subduction zone that was present to the west of the Antarctic Peninsula for much of the Cenozoic [e.g., *Eagles et al*., 2009a]. The Ferrigno Rift is a narrow (10–30 km wide), deep basin (maximum depth of ~1500 m below sea level) with well-defined, steeply dipping flanks [*Bingham et al*., 2012], which resembles other narrow rifted basins observed within the WARS.

In summary, a Cretaceous rift underlies the Abbot Ice Shelf. This rift formed the easternmost segment of the continental rifting that separated Zealandia from Antarctica. Extension beneath the ice shelf is relatively minor as rifting centered north of Thurston Island early in the rift process. The Abbot rift is bounded on the west by an extensive sedimentary basin beneath the continental shelf of the Amundsen Sea Embayment that formed during the same Cretaceous rifting. The Abbot Rift and the Amundsen Embayment Shelf Basin are separated by a well-defined boundary zone that must originally been a transfer or accommodation zone between rift segments. The Amundsen Embayment Shelf Basin crust underwent more extension than the crust beneath the Abbot Rift, but again the extension shifted north of the present shelf and proceeded to

seafloor spreading by magnetic chron 34 (~83 Ma) (Figure 1). It appears that the both the Abbot Rift and the Amundsen Embayment continental shelf have been tectonically quiescent since the initiation of seafloor spreading. The main factors shaping the development of the shelf since 83 Ma have been subsidence, sedimentation and the advance and retreat of the West Antarctic Ice Sheet.

5. Southern Boundary of the Bellingshausen Plate

The Bellingshausen Plate was a small tectonic plate that existed in the southeastern Pacific Ocean to the north of West Antarctica between about 83 and 61 Ma, when it was incorporated into the Antarctic Plate [e.g., *Stock and Molnar*, 1987; *Cande et al*., 1995; *McAdoo and Laxon*, 1997; *Larter et al*., 2002; *Eagles et al*., 2004a, 2004b]. *Stock and Molnar* [1987] first proposed the existence of the Bellingshausen Plate to explain differing fracture zone trends on either side of the Antipodes Fracture Zone on the Pacific-Antarctic Ridge during the Late Cretaceous and earliest Tertiary. *Cande et al*. [1995] confirmed the necessity for an independent Bellingshausen Plate and were able to define magnetic chron 27 (~61 Ma) as when it was incorporated into the Antarctic Plate during a major reorganization of the spreading system.

Although the existence of an independent Bellingshausen Plate during that time interval has been confirmed, only the northern and eastern boundaries have been well delineated. The northern boundary is defined by the chron 27 magnetic anomaly. *McAdoo and Laxon* [1997] identified an approximately north-south lineation in the ERS-1 satellite gravity field near 94°W that includes the BGA as the eastern boundary of the Bellingshausen Plate. The western boundary is not well defined, although *Heinemann et al*. [1999] suggest that a short north-south trending graben imaged on seismic reflection lines at ~126.4°W may be a portion of it. The location and nature of the southern boundary of the Bellingshausen Plate has remained uncertain and a subject of discussion. *Stock et al*. [1996] suggest that the Bellingshausen Plate may have been entirely oceanic and thus have formed seaward of the continental margin after rifting between Zealandia and Antarctica. *Wobbe et al*. [2012] modeled a very wide "Bellingshausen Plate Boundary Zone" along the Antarctic margin, often extending from mid-shelf well out into the deep ocean. *Gohl et al*. [2007, 2013a] and *Gohl* [2012] postulated a distributed or shifting plate boundary on the continental shelf of the Amundsen Sea made up of several WNW-ESE trending geophysical lineations including the Abbot Ice Shelf and a rift beneath Pine Island Glacier.

The BGA structure in the deep ocean north of the Abbot Ice Shelf consists of a north-south trending high-low gravity couple with a maximum peak to peak amplitude of about 140 mGal (Figures 2 and 5b). Seismic reflection and gravity data show that the gravity low overlies a sediment filled trough, which gravity modeling implies extends to a depth of 11–13 km [*Gohl et al*., 1997a] (Figure 5b). *Gohl et al*. [1997a] argue that the BGA was the site of convergence between the Bellingshausen and Phoenix Plates prior to both of those plates being incorporated into the Antarctic Plate. Kinematic models based on reconstruction of seafloor spreading magnetic anomalies [*Larter et al*., 2002; *Eagles et al*., 2004b, 2004a; *Wobbe et al*., 2012] also imply significant convergence across the BGA structure and it is generally accepted as a portion of the eastern boundary of Bellingshausen Plate.

The tectonic boundary beneath the Abbot Ice Shelf at 94°W between the rift basin to the west and unextended crust to the east is directly in line with the BGA structure (Figure 4). *Cunningham et al*. [2002] interpret the BGA structure as continuing onto the continental shelf at 94°W. This conclusion is based on modeling of a bathymetry, seismic reflection and gravity line (BAS923-26) extending from about 97°W to 94°W at 70°40′S on the outermost continental shelf (Figures 2 and 4). Their model shows a trough with 13–17 km of sediment beneath the continental shelf that they interpret as a continuation of the BGA structure. However, the profile that they model intersects the shelf edge gravity high at both ends of their line (Figure 2). The shelf edge gravity high is part of an edge effect gravity anomaly resulting from superposition of the shallow density contrast of water versus sediment/crust and the deeper contrast of mantle versus crust across the margin (Figure 6). The shape and width of the anomaly can be affected by the steepness of the margin (Figure 6b), by the presence of thick sediments (Figure 6c) or by tectonic structures such as the outer shelf basement high observed in portions of the Amundsen Embayment margin [*Gohl et al*., 2013b]. However, a gravity high at the shelf edge paired with a gravity low on the continental rise is a ubiquitous feature of continental margins. The gravity and bathymetry profile at 71°30′S, shown in Figure 5a is located

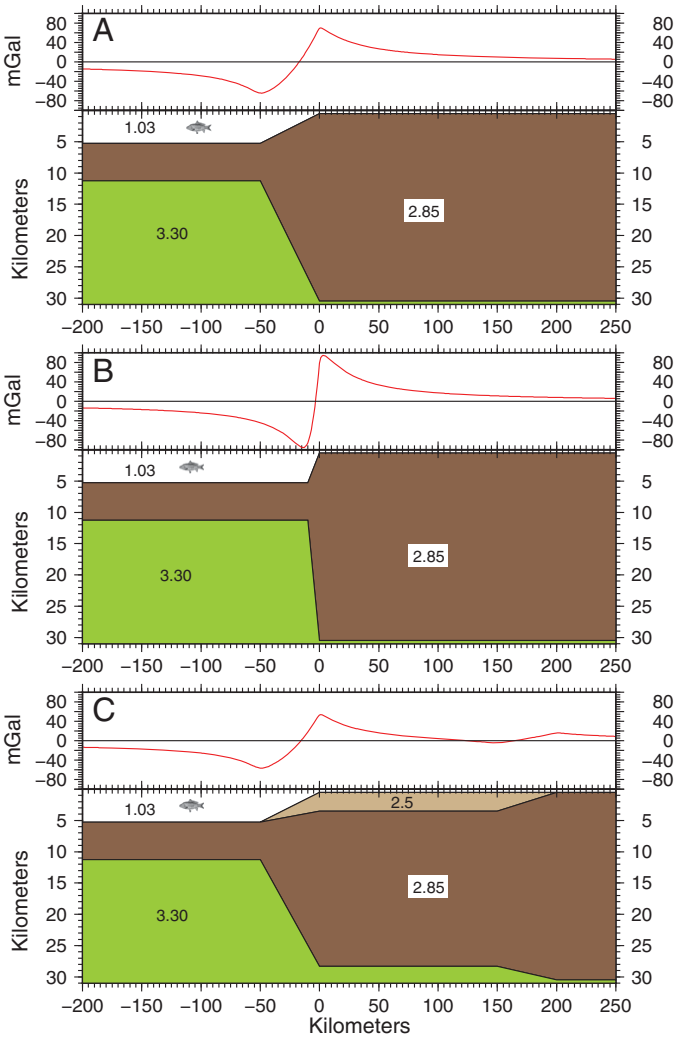

Figure 6. Gravity models illustrating the isostatic edge effect gravity anomaly ubiquitously found at continental margins. (a) The calculated gravity anomaly for a generic margin with a 50 km wide ocean-continent transition. (b) The effect of changing the width of the transition and (c) the effect of thick sediment beneath the continental shelf. Densities assumed for the calculations in g/cm^3 are shown. All of the profiles are everywhere in local isostatic equilibrium.

south of the shelf edge gravity high. It shows a broad step in the gravity anomalies that can be modeled as a transition from the shallower basement of the former convergent margin in the east to deeper basement of the rifted margin in the west (Figure 5a). This boundary served as a transform fault while rifting was active in the Abbot Rift. The BGA structure, which formed later as the result of compressive deformation, does not extend into the continental crust of the continental shelf.

The BGA gravity low swings to the west near 70°S and merges with the continental rise gravity low portion of the continental margin edge effect anomaly (Figures 2 and 7b) which is deeper and better developed here than farther to the west (Figures 2, 7b, and 8). This well-developed gravity low extends WSW from 95°W to 102°W where there is an offset to the north in both the shelf edge (Figure 7a) and in the continental margin gravity anomaly (Figure 7b). The margin from 95°W to 102°W has a steep continental slope and a narrow, poorly developed continental rise (Figure 8a). A seismic reflection line (BAS923-25) across the margin near 97°W (location shown in Figures 2 and 4) shows intense deformation beneath the continental slope [*Larter et al*., 1999]. On this line, the basement deepens toward the margin and the sedimentary section includes a sequence that thickens toward the margin with diverging reflectors that *Larter et al*. [1999] argue was deposited as the crust was flexed down toward the margin. These sediments become highly contorted and then acoustically opaque approaching the margin [*Larter et al*.,

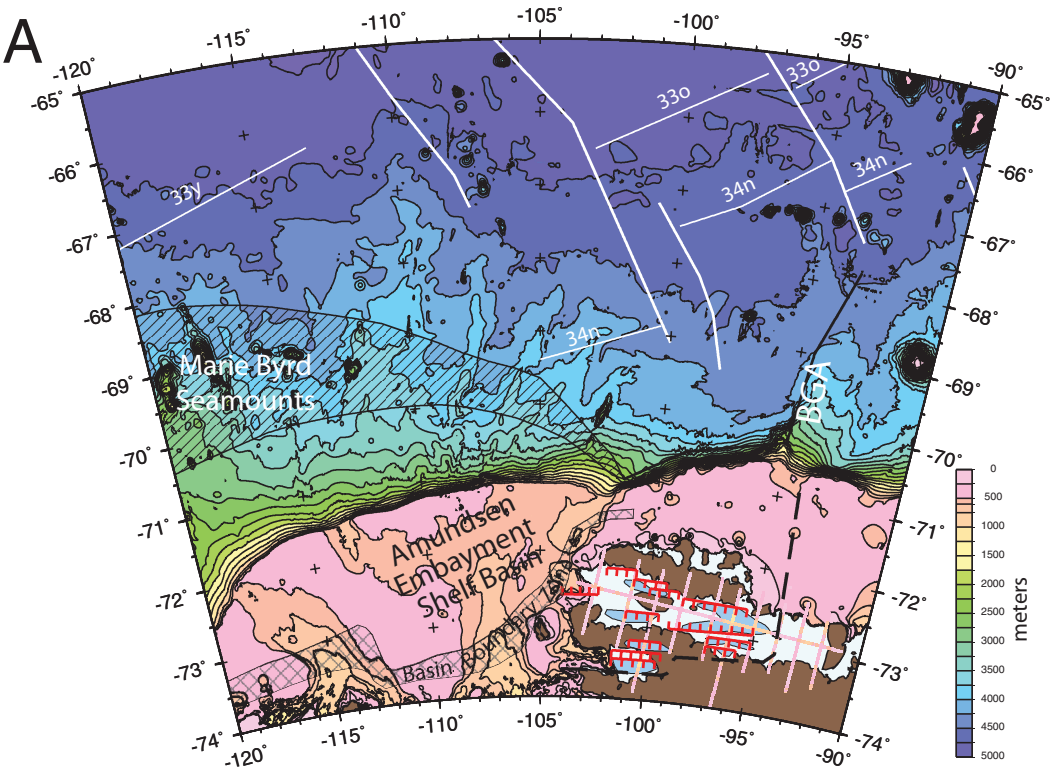

Figure 7 a. Tectonic synthesis of the Amundsen Embayment continental margin resulting from our analysis of bathymetry beneath the Abbot Ice Shelf. Subice bed from radar and bathymetry from inversion of gravity anomalies are shown along OIB flights. Offshore bathymetry is from IBCSO [*Arndt et al*., 2013]. Color scale for bathymetry is shown on right. Rift basins beneath Abbot and Cosgrove ice shelves are shown in blue with faults in red. Black dashed line shows the extent of rifting. Cross-hatched area on the continental shelf shows the transition or hinge zone from exposed or lightly sedimented basement on the landward side to a thickly sedimented basin under the outer shelf. Hachured area north of the shelf edge shows the portion of the southern boundary of the Bellingshausen Plate that underwent diffuse extension and solid black line shows the convergent portion of the southern boundary. Fracture zones and marine magnetic anomaly correlations are from *Cande et al*. [1982] and *Larter et al*. [2002]. BGA is the Bellingshausen Gravity Anomaly.

1999; *Cunningham et al*., 2002]. *Larter et al*. [1999] interpret this as evidence of compressive deformation.

Compressive deformation along the continental margin between 95°W and 102°W is consistent with kinematic reconstructions of the development of the region based on marine magnetic anomalies [*Larter et al*., 2002; *Eagles et al*., 2004a] which imply a component of clockwise rotation between the Bellingshausen and Antarctic plates from about 74 to 62 Ma, when the Bellingshausen Plate was absorbed into the Antarctic Plate. *Larter et al*. [2002] determined a Bellingshausen/Antarctica stage pole for the time interval between magnetic anomaly chrons 32n.1r and 28r (71.5–63.8 Ma) at 73.64°S, 101.04°W. This pole is shown by a red dot in Figure 9. This relative motion results in convergence along the eastern portion of the southern boundary of the Bellingshausen Plate with the Antarctic Plate and extension between the two plates to the west (Figure 9). The transition in the relative motion between the two plates was located near 102°W (Figure 9).

The BGA structure lies along the western side of what was at that time a triangular shaped salient of the Antarctic Plate (Figure 9). This is the last remnant of the Charcot Plate, a small plate that separated from the Phoenix Plate in the mid-Cretaceous [*McCarron and Larter*, 1998; *Larter et al*., 2002], probably in a manner similar to the segmentation of the Farallon Plate into the Rivera, Cocos, and Nazca plates [e.g., *Menard*, 1978; *Atwater*, 1989; *Lonsdale*, 2005]. Charcot Plate lithosphere was subducted beneath Antarctica until about the time of magnetic Chron 34 (~83 Ma), when subduction stalled during the breakup of Zealandia and Antarctica, with the remaining fragment captured by Antarctica [*Larter et al*., 2002].

In Figure 9, we follow *Eagles et al*. [2004a] in showing a Bellingshausen-Phoenix ridge segment to the east of the Charcot salient. The triple junction at the western end of that segment migrated along the transform toward and probably into the subduction zone in response to the creation of Bellingshausen lithosphere to the north.

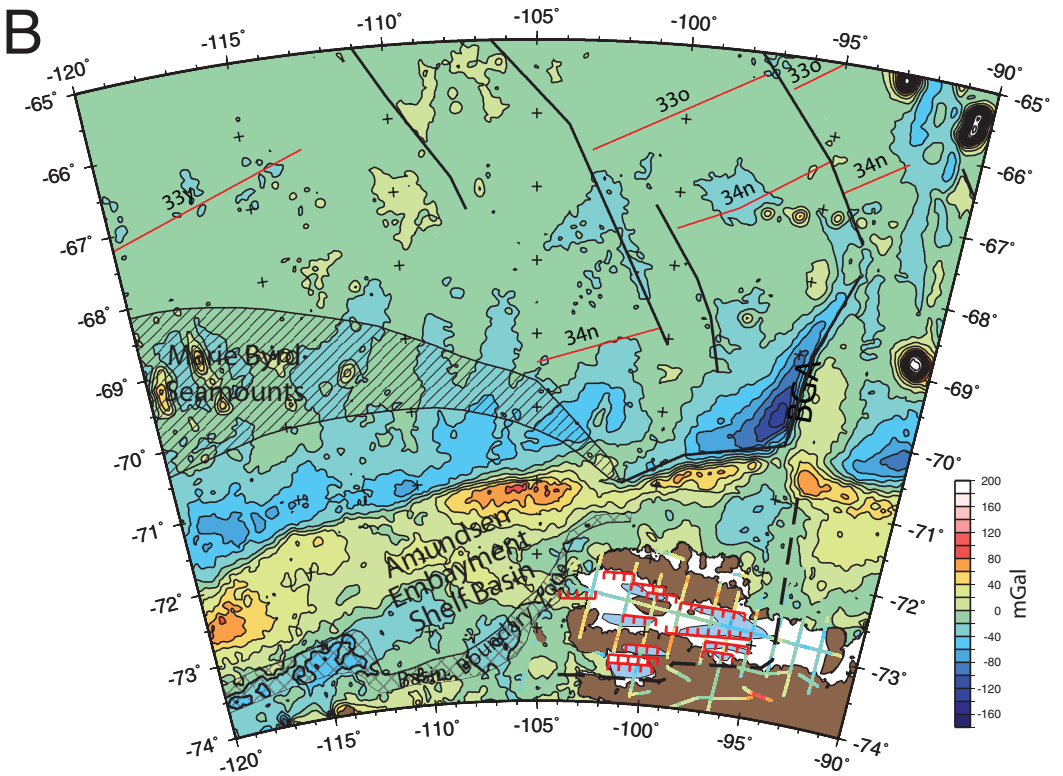

Figure 7b. Tectonic synthesis of the Amundsen Embayment continental margin in the context of regional gravity anomalies. Free-air gravity anomalies from OIB flights are plotted along flight lines. Gravity anomalies in offshore areas are satellite-derived free-air anomalies from *McAdoo and Laxon* [1997] contoured at 20 mGal intervals. Color scale for airborne and satellite gravity anomalies is shown on right. Otherwise, as in Figure 7a.

The character of the continental margin changes at ~102°W, where *Larter et al.*'s [2002] rotation pole predicts a change from compression to the east to extension to the west. The continental slope to the west of 102°W is gentler than to the east with a broader, well-developed rise (Figure 8b). The difference in morphology is reflected in the shelf edge gravity high, which has a sharper seaward slope to the east of 102°W than to the west (Figure 8). Seismic lines crossing the slope and rise to the west of 103°W [*Cunningham et al.*, 2002; *Gohl et al.*, 2013b; *Kalberg and Gohl*, 2014; *Uenzelmann-Neben and Gohl*, 2014] show no signs of the compression and intense deformation evident at 97°W.

Extension to the west of 102°W appears to have been diffuse and to have occurred in the area of the Marie Byrd Seamounts. The Marie Byrd Seamounts extend for 800 km from about 112°W to 130°W in an east-west band between 68°S and 71°S. Alkali basalts dredged from Hubert Miller Seamount (69°17′S, 121°20′W), Haxby Seamount (69°07′S, 123°35′W), and Seamount C (69°12′S, 117°30′W) gave $^{40}Ar/^{39}Ar$ ages of 65–56 Ma [*Kipf et al.*, 2014], during and slightly after the last stages of independent Bellingshausen Plate motion.

Kipf et al. [2014] proposed, on the basis of a HIMU component in the rocks recovered from the Marie Byrd Seamounts, that the lavas erupted at the Marie Byrd Seamounts are derived from Cretaceous plume material underplating the West Antarctica lithosphere that was transported by "continental insolation flow" [*King and Anderson*, 1995, 1998] into the upper mantle of the adjacent oceanic areas. Whatever the source of the lava, lithospheric extension is required to cause it to ascend and be erupted. We suggest that this extension resulted from rotation of the Bellingshausen plate relative to the Antarctic plate with diffuse extension through the region occupied by the Marie Byrd seamounts. Seismic reflection lines through the seamounts [*Gohl et al.*, 1997b; *Nitsche*, 1998; *Uenzelmann-Neben and Gohl*, 2012] show very rough basement and contorted sediments, described by *Gohl et al.* [1997b] as "almost chaotic" north of 71°S. Seafloor spreading anomalies are not recognized in the region of the Marie Byrd Seamounts (Figures 7a and 7b), even though they are found on the conjugate margin and presumably were originally present. These observations imply

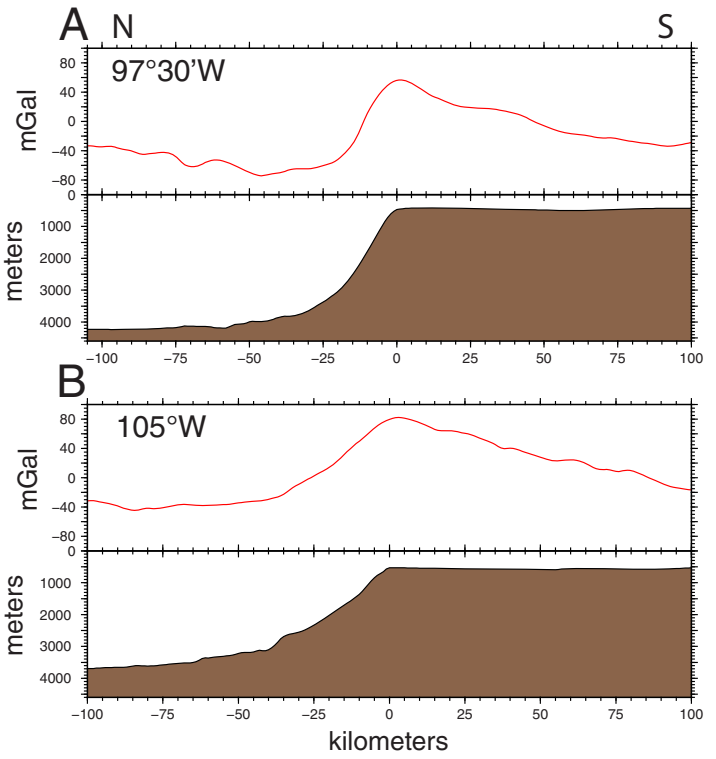

Figure 8. Bathymetry and free-air gravity profiles across the Amundsen Sea continental margin at 97°30′W and at 105°W. Location is shown in Figures 2 and 4. Origin of the horizontal scale is set at the shelf break on each profile. Note the change between the two profiles in steepness of the continental slope and of the shelf edge gravity high. Bathymetry is from IBCSO [*Arndt et al*., 2013] and gravity is from *McAdoo and Laxon* [1997]. North is to the left.

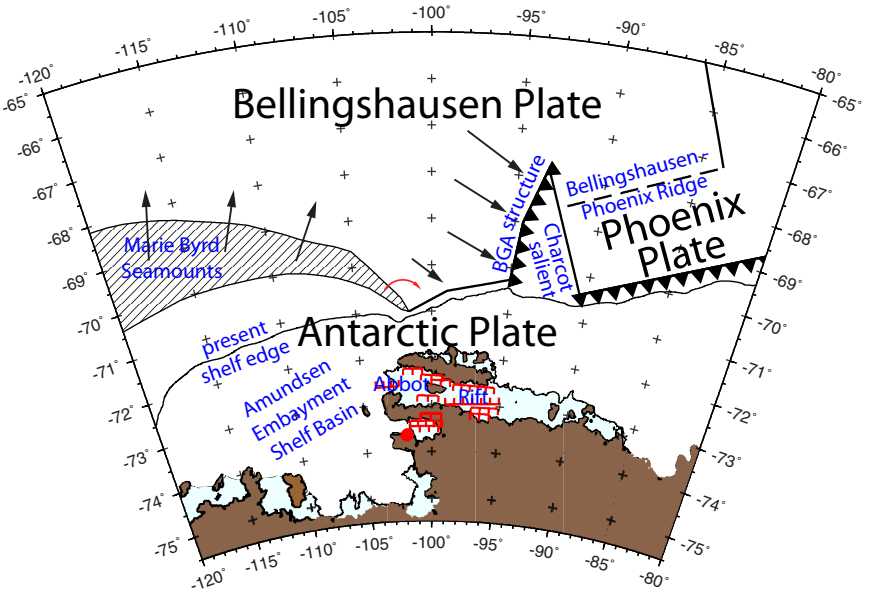

Figure 9. Sketch showing plate interactions near the end of the Bellingshausen Plate's independent existence. The Bellingshausen-Antarctic pole for this time, at 73.64°S, 101.04°W [*Larter et al*., 2002], is shown by a red dot. Motion between the two plates about this pole resulted in diffuse extension to the west of ~102°W in an area (shown as hachured) that includes the Marie Byrd Seamounts. The relative motion to the east of ~102 W was convergent with incipient subduction beneath the Bellingshausen Gravity Anomaly structure, which forms the western side of a triangular salient of the Antarctic Plate (see text). Following *Eagles et al*. [2004a], we show a Bellingshausen-Phoenix Ridge segment to the east of this salient with subduction of Phoenix Plate lithosphere along the continental margin to the east of ~90°W.

tectonic disruption and magmatic overprinting of the original oceanic crust. We interpret this disruption as resulting from extension and the resulting volcanism between the Bellingshausen and Antarctic plates across a broad, diffuse plate boundary (Figures 7 and 9). Extension decreased to the east as the diffuse plate boundary approached the pole (Figure 9), so that magmatism was eventually cut off at the eastern end of the Marie Byrd Seamounts near 112°W.

6. Conclusions

1. Inversion of NASA Operation IceBridge gravity data shows that the portion of the Abbot Ice Shelf to the west of 94°W is underlain by an extensional rifted terrain formed at about 90 Ma in the early stages of rifting between Antarctica and Zealandia. A rift also underlies Cosgrove Ice Shelf to the south. After a limited amount of extension south of Thurston Island, rifting centered north of the island where it led to lithospheric rupture and the establishment of a spreading center.
2. The Amundsen Sea Embayment continental shelf is underlain by a sedimentary basin, also formed by rifting between Zealandia and Antarctica. The crustal extension factor, β, is 1.5–1.7 implying that 80–100 km of extension occurred in a region that is now 250 km wide. Following this extension, rifting shifted to a location north of the present shelf edge and proceeded to continental rupture and seafloor spreading. We interpret geophysical data from the region to show that, since that time, the Amundsen Embayment shelf has been tectonically quiescent and has not been affected by Bellingshausen-Antarctic interactions or by the West Antarctic Rift System. The main factors controlling the geologic development of the Amundsen continental shelf since the Late Cretaceous appear to be subsidence, sedimentation and the advance and retreat of the West Antarctic Ice Sheet.
3. The southern boundary of the former Bellingshausen Plate is located at the base of the continental slope from 94°W to 102°W and is marked by a zone of compression of the sediments underlying the slope. West of 102°W, the boundary swings away from the continental margin and becomes a diffuse zone of extension and magmatic activity encompassing the Marie Byrd Seamounts. These seamounts extend for 800 km from about 112°W to 130°W in an east-west band between 68°S and 71°S. Basalts recovered from three of the seamounts have been dated as erupted between 65 and 56 Ma [*Kipf et al*., 2014], dates that straddle the end of independent Bellingshausen Plate motion.

Acknowledgments
The NASA Operation IceBridge airborne data and the inversions for bathymetry used in this paper are archived by the National Snow and Ice Data Center and are available at http://nsidc.org/data/icebridge. The GMT software package [*Wessel and Smith*, 1998] was used extensively in data analysis and preparation of figures. This work was supported by NASA grants NNX09AR49G, NNX10AT69G, and NNX13AD25A. We thank Karsten Gohl and two anonymous reviewers for comments and suggestions that greatly improved the manuscript and Frank Nitsche for valuable comments on an earlier draft.

References

Anandakrishnan, S., and J. P. Winberry (2004), Antarctic subglacial sedimentary layer thickness from receiver function analysis, *Global Planet. Change*, *42*, 167–176, doi:10.1016/j.gloplacha.2003.10.005.
Anandakrishnan, S., D. D. Blankenship, R. B. Alley, and P. L. Stoffa (1998), Influence of subglacial geology on the position of a West Antarctic ice stream from seismic observations, *Nature*, *394*, 62–65.
Argyle, M., S. Ferguson, L. Sander, and S. Sander (2000), AIRGrav results: A comparison of airborne gravity data with GSC test site data, *Leading Edge*, *19*, 1134–1138.
Arndt, J. S., et al. (2013), The International Bathymetric Chart of the Southern Ocean (IBCSO) Version 1.0—A new bathymetric compilation covering circum-Antarctic waters, *Geophys. Res. Lett.*, *40*, 3111–3117, doi:10.1002/grl.50413.
Atwater, T. M. (1989), Plate tectonic history of the northeast Pacific and western North America, in *The Eastern Pacific Ocean and Hawaii, The Geology of North America*, vol. N, edited by E. L. Winterer, D. M. Hussong, and R. W. Decker, pp. 21–72, Geol. Soc. Am., Boulder, Colo.
Barker, P. F. (1982), The Cenozoic subduction history of the Pacific margin of the Antarctic Peninsula: Ridge crest-trench interactions, *J. Geol. Soc. London*, *139*, 787–801.
Bell, R. E., D. D. Blankenship, C. A. Finn, D. L. Morse, T. A. Scambos, J. M. Brozena, and S. M. Hodge (1998), Influence of subglacial geology on the onset of a West Antarctic ice stream from aerogeophysical observations, *Nature*, *394*, 58–62.
Bingham, R. G., F. Ferraccioli, E. C. King, R. D. Larter, H. D. Pritchard, A. M. Smith, and D. G. Vaughan (2012), Inland thinning of West Antarctic Ice Sheet steered along subglacial rifts, *Nature*, *487*, 468–471, doi:10.1038/nature11292.
Bird, R. T., and D. F. Naar (1994), Intratransform origins of mid-ocean ridge microplates, *Geology*, *22*, 987–990.
Block, A. E., R. E. Bell, and M. Studinger (2009), Antarctic crustal thickness from satellite gravity: Implications for the Transantarctic and Gamburtsev Subglacial Mountains, *Earth Planet. Sci. Lett.*, *288*, 194–203, doi:10.1016.j.epsl.2009.0222.
Bosworth, W. (1985), Geometry of propagating continental rifts, *Nature*, *316*, 625–627.
Bosworth, W. (1994), A model for the three-dimensional evolution of continental rift basins, north-east Africa, *Geol. Rundsch*, *83*, 671–688.
Bosworth, W., and K. McClay (2001), Structural and stratigraphic evolution of the Gulf of Suez Rift, Egypt: A synthesis, in *Peri-Tethys Memoir 6: Peri-Thetyan Rift/Wrench Basins and Passive Margins*, edited by P. A. Ziegler et al., pp. 567–606, Mus. Natl. d'Histoire Nat., Paris.
Brisbourne, A. M., A. M. Smith, E. C. King, K. W. Nicholls, P. R. Holland, and K. Makinson (2014), Seabed topography beneath Larsen C Ice Shelf from seismic soundings, *Cryosphere*, *8*, 1–14, doi:10.5194/tc-8-1-2014.
Burgess, C. F., B. R. Rosendahl, S. Sander, C. A. Burgess, J. Lambiase, S. Derksen, and N. Meader (1988), The structural and stratigraphic evolution of Lake Tanganyika: A case study of Continental Rifting, in *Triassic-Jurassic Rifting: Continental Breakup and the Origin of the Atlantic Ocean and Passive Margins*, edited by W. Manspeizer, pp. 859–881, Elsevier, Amsterdam.
Cande, S. C., E. M. Herron, and B. R. Hall (1982), The early Cenozoic tectonic history of the southeast Pacific, *Earth Planet. Sci. Lett.*, *57*, 63–74.

Cande, S. C., C. A. Raymond, J. M. Stock, and W. F. Haxby (1995), Geophysics of the Pitman Fracture Zone and Pacific-Antarctic plate motions during the Cenozoic, *Science*, *270*, 947–953.
Chaput, J., R. C. Aster, A. Huerta, X. Sun, A. Lloyd, D. A. Wiens, A. A. Nyblade, S. Anandakrishnan, J. P. Winberry, and T. Wilson (2014), The crustal thickness of West Antarctica, *J. Geophys. Res.*, *119*, 378–395, doi:10.1002/2013JB010642.
Cochran, J. R. (1983), A model for the development of the Red Sea, *Am. Assoc. Pet. Geol. Bull.*, *67*, 41–69.
Cochran, J. R. (2005), Northern Red Sea: Nucleation of an oceanic spreading center within a continental rift, *Geochem. Geophys. Geosyst.*, *6*, Q03006, doi:10.1029/2004GC000826.
Cochran, J. R., and R. E. Bell (2010), *IceBridge Sander AIRGrav L1B Geolocated Free Air Gravity Anomalies, V01.5, Digital Media*, Natl. Snow and Ice Data Cent., Boulder, Colo.
Cochran, J. R., and R. E. Bell (2012), Inversion of IceBridge gravity data for continental shelf bathymetry beneath the Larsen ice shelf, Antarctica, *J. Glaciol.*, *58*, 540–552, doi:10.3189/2012JoG11J033.
Cochran, J. R., S. S. Jacobs, K. J. Tinto, and R. E. Bell (2014), Bathymetric and oceanic controls on Abbot Ice Shelf thickness and stability, *The Cryosphere*, *8*, 877–889, doi:10.5194/tc-8–877-2014.
Cunningham, A. P., R. D. Larter, P. F. Barker, K. Gohl, and F. O. Nitsche (2002), Tectonic evolution of the Pacific margin of Antarctica: 2. Structure of Late Cretaceous—Early Tertiary plate boundaries in the Bellingshausen Sea from seismic reflection and gravity data, *J. Geophys. Res.*, *107*(B12), 2346, doi:10.1029/2002JB001897.
Dalziel, I. W. D. (2006), On the extent of the active West Antarctic Rift System, in *Proceedings of Workshop on Frontiers and Opportunities in Arctic Geosciences: Terra Antarctica Reports no. 12*, edited by C. S. Siddoway and C. A. Ricci, pp. 193–202, Terra Antarct. Publ., Siena, Italy.
Eagles, G., K. Gohl, and R. D. Larter (2004a), High-resolution animated tectonic reconstruction of the South Pacific and West Antarctic Margin, *Geochem. Geophys. Geosyst.*, *5*, Q07002, doi:10.1029/2003GC000657.
Eagles, G., K. Gohl, and R. D. Larter (2004b), Life of the Bellingshausen Plate, *Geophys. Res. Lett.*, *31*, L07603, doi:10.1029/2003GL019127.
Eagles, G., K. Gohl, and R. D. Larter (2009a), Animated tectonic reconstruction of the Southern Pacific and alkaline volcanism at its convergent margins since Eocene times, *Tectonophysics*, *464*, 21–29, doi:10.1016/j.tecto.200710.005.
Eagles, G., R. D. Larter, K. Gohl, and A. P. M. Vaughan (2009b), West Antarctic Rift System in the Antarctic Peninsula, *Geophys. Res. Lett.*, *36*, L21305, doi:10.1029/2009GL040721.
Ebinger, C. J. (1989a), Geometric and kinematic development of border faults and accommodation zones, Kivu-Rusizi Rift, Africa, *Tectonics*, *8*, 117–134.
Ebinger, C. J. (1989b), Tectonic development of the western branch of the East African rift system, *Bull. Geol. Soc. Am.*, *101*, 885–903.
Ferraccioli, F., F. Coren, E. Bozzo, C. Zanolla, S. Gandolfi, I. Tabacco, and M. Frezzotti (2001), Rifted(?) crust at the East Antarctic Craton margin: Gravity and magnetic interpretation along a traverse across the Wilkes Subglacial Basin margin, *Earth Planet. Sci. Lett.*, *192*, 407–421.
Ferraccioli, F., P. C. Jones, A. P. M. Vaughan, and P. T. Leat (2006), New aerogeophysical view of the Antarctic Peninsula: More pieces, less puzzle, *Geophys. Res. Lett.*, *33*, L05310, doi:10.1029/2005GL024636.
Fricker, H. A., S. P. Carter, R. E. Bell, and T. A. Scambos (2014), Active lakes of Recovery Ice Stream, East Antarctica: A bedrock-controlled subglacial hydrological system, *J. Glaciol.*, *60*, 1015–1030, doi:10.3189/2014JoG14J063.
Garfunkel, Z., and Y. Bartov (1977), The tectonics of the Suez Rift, *Bull. Geol. Surv. Isr.*, *71*, 44 p.
Gaulier, J. M., X. LePichon, N. Lyberis, F. Avedik, L. Geli, I. Moretti, A. Deschamps, and S. Hafez (1988), Seismic study of the crust of the northern Red Sea and Gulf of Suez, *Tectonophysics*, *153*, 25–54.
Gettings, M. E., H. R. Blank, W. D. Mooney, and J. H. Healy (1986), Crustal structure of southwestern Saudi Arabia, *J. Geophys. Res.*, *91*, 6491–6512.
Gohl, K. (2012), Basement control on past ice sheet dynamics in the Amundsen Sea Embayment, West Antarctica, *Palaeogeogr. Palaeoclim., Palaeoecol.*, *335*, 35–41, doi:10.1016.jpaleo.2011.02.022.
Gohl, K., F. O. Nitsche, and H. L. Miller (1997a), Seismic and gravity data reveal Tertiary interplate subduction in the Bellingshausen Sea, southeast Pacific, *Geology*, *25*, 371–374.
Gohl, K., F. O. Nitsche, K. Vanneste, H. Miller, N. Fechner, L. Oszko, C. Hubscher, E. Weigelt, and A. Lambrecht (1997b), Tectonic and sedimentary architecture of the Bellingshausen and Amundsen Sea Basins, SE Pacific, by seismic profiling, in *The Antarctic Region: Geological Evolution and Processes*, edited by C. A. Ricci, pp. 719–723, Terra Antarct., Siena, Italy.
Gohl, K., et al. (2007), Geophysical survey reveals structures in the Amundsen Sea embayment, West Antarctica, in *Proceedings of the 10th International Symposium of Antarctic Earth Sciences, USGS Open File Rep. 2007-1047*, edited by A. K. Cooper and C. R. Raymond, USGS and the National Academies, Wash.
Gohl, K., A. Denk, G. Eagles, and F. Wobbe (2013a), Deciphering tectonic phases of the Amundsen Sea Embayment shelf, West Antarctica, from a magnetic anomaly grid, *Tectonophysics*., *585*, 113–123, doi:10.1016/j.tecto.2012.06.036.
Gohl, K., G. Uenzelmann-Neben, R. D. Larter, C. D. Hillenbrand, K. Hochmuth, T. Kalberg, E. Weigelt, B. Davy, G. Kuhn, and F. O. Nitsche (2013b), Seismic stratigraphic record of the Amundsen Sea Embayment from pre-glacial to recent times: Evidence for a dynamic West Antarctic ice sheet, *Mar. Geol.*, *344*, 115–131, doi:10.1016/j.margeo.2013.06.011.
Golynsky, A. V., et al. (2001), ADMAP: Magnetic anomaly map of the Antarctic, in *British Antarctic Survey Miscellaneous Series*, sheet 10, scale 1:10,000,000, edited by P. Morris and R. von Frese, British Antarctic Survey, Cambridge, U. K. [Available at http://www.geology.ohio-state.edu/geophys/admap.]
Graham, A. G. C., R. D. Larter, K. Gohl, C. D. Hillenbrand, J. A. Smith, and G. Kuhn (2009), Bedform signature of a West Antarctic palaeo-ice stream reveals a multi-temporal record of flow and substrate control, *Quat. Sci. Rev.*, *28*, 2774–2793, doi:10.1016/j.quascirev.2009.07.003.
Grunow, A. M., D. V. Kent, and I. W. D. Dalziel (1991), New paleomagnetic data from Thurston Island: Implications for the tectonics of West Antarctica and Weddell Sea opening, *J. Geophys. Res.*, *96*, 17,935–17,954.
Heinemann, J., J. M. Stock, R. Clayton, K. Hafner, S. C. Cande, and C. A. Raymond (1999), Constraints on the proposed Marie Byrd Land-Bellingshausen plate boundary from seismic reflection data, *J. Geophys. Res.*, *104*, 25,321–25,330.
Herron, E. M., and B. E. Tucholke (1976), Seafloor magnetic patterns and basement structure in the southeastern Pacific, in *Initial Reports of the Deep Sea Drilling Project*, vol.35, edited by C. D. Hollister and C. Craddock, pp. 263–278, U.S. Gov. Print. Off., Washington, D. C.
Jordan, T. A., F. Ferraccioli, D. G. Vaughan, J. W. Holt, H. Corr, D. D. Blankenship, and T. H. Diehl (2010), Aerogravity evidence for major thinning under the Pine Island Glacier region (West Antarctica), *Bull. Geol. Soc. Am.*, *122*, 714–726, doi:10.1130/B26417.1.
Kalberg, T., and K. Gohl (2014), The crustal structure and tectonic development of continental margin of the Amundsen Sea Embayment, West Antarctica: Implications from geophysical data, *Geophys. J. Int.*, *198*, 327–341, doi:10.1093/gji/ggu118.

Karner, G. D., B. R. Byamungu, C. J. Ebinger, A. B. Kampunzu, R. K. Mukasa, J. Nyakaana, E. N. T. Rubondo, and N. M. Upcott (2000), Distribution of crustal extension and regional basin architecture of the Albertine rift system, East Africa, *Mar. Pet. Geol.*, *17*, 1131–1150.

King, S. D., and D. L. Anderson (1995), An alternative mechanism to flood basalt formation, *Earth Planet. Sci. Lett.*, *136*, 269–279, doi: 10.1016/0012–821X(95)00205-Q.

King, S. D., and D. L. Anderson (1998), Edge driven convection, *Earth Planet. Sci. Lett.*, *160*, 289–296, doi:10.1016/S0012–821X(98)00089-2.

Kipf, A., F. Hauff, R. Werner, K. Gohl, P. Van den Bogaard, K. Hoernle, D. Maicher, and A. Klugel (2014), Seamounts off the West Antarctic margin: A case for non-hotspot deriven intraplate volcanism, *Gondwana Res.*, *25*, 1660–1679, doi:10.1016/j.gr.2013.06.013.

Krabill, W., W. Abdalati, E. R. Frederick, S. S. Manizade, C. F. Martin, J. G. Sonntag, R. N. Swift, R. H. Thomas, and J. G. Yungel (2002), Aircraft laser altimetry measurement of elevation changes of the Greenland Ice Sheet: Techniques and accuracy assessment, *J. Geodyn.*, *34*(3–4), 357–376.

Lambiase, J. J., and W. Bosworth (1995), Structural controls on sedimentation in continental rifts, in *Hydrocarbon Habitat in Rift Basins*, edited by J. J. Lambiase, pp. 117–144, Geol. Soc., London, U. K.

Larter, R. D., A. P. Cunningham, P. F. Barker, K. Gohl, and F. O. Nitsche (1999), Structure and tectonic evolution of the West Antarctic continental margin and Bellingshausen Sea, *Korean J. Polar Sci.*, *10*, 125–133.

Larter, R. D., A. P. Cunningham, P. F. Barker, K. Gohl, and F. O. Nitsche (2002), Tectonic evolution of the Pacific margin of Antarctica: 1. Late Cretaceous tectonic reconstructions, *J. Geophys. Res.*, *107*(B12), 2345, doi:10.1029/2000JB000052.

Leat, P. T., B. C. Storey, and R. J. Pankhurst (1993), Geochemistry of Palaeozoic-Mesozoic Pacific rim orogenic magmatism, Thurston Island area, West Antarctica, *Antarct. Sci.*, *5*, 281–296.

Leat, P. T., J. H. Scarrow, and I. L. Millar (1995), On the Antarctic Peninsula batholith, *Geol. Mag.*, *132*, 399–412.

LePichon, X., and J. Francheteau (1978), A plate tectonic analysis of the Red Sea—Gulf of Aden Area, *Tectonophysics*, *46*, 369–406.

Leuschen, C. (2011), *IceBridge MCoRDS L1B Geolocated Radar Echo Strength Profiles, V01.3, Digital Media*, Natl. Snow and Ice Data Cent., Boulder, Colo.

Lonsdale, P. (2005), Creation of the Cocos and Nazc plates by fission of the Farallon plate, *Tectonophysics*, *404*, 237–264, doi:10.1016/j.tecto.2005.05.011.

Lowe, A. L., and J. B. Anderson (2002), Reconstruction of the West Antarctic ice sheet in Pine Island Bay during the Last Glacial Maximum and its subsequent retreat history, *Quat. Sci. Rev.*, *21*, 1879–1897.

Makris, J., A. Allam, T. Moktar, A. Basahel, G. A. Dehghani, and M. Bazari (1983), Crustal Structure in the northwestern region of the Arabian Shield and its transition to the Red Sea, *Bull Fac. Sci. King Abdulaziz Univ.*, *6*, 435–447.

Mayes, C. L., L. A. Lawver, and D. T. Sandwell (1990), Tectonic history and new isochron chart of the South Pacific, *J. Geophys. Res.*, *95*, 8543–8567.

McAdoo, D. C., and S. W. Laxon (1997), Antarctic tectonics: Constraints from an ERS-1 satellite marine gravity field, *Science*, *276*, 556–560, doi:10.1126/science.276.5312.556.

McAdoo, D. C., and K. M. Marks (1992), Gravity fields of the Southern Ocean from Geosat data, *J. Geophys. Res.*, *97*, 3247–3260.

McCarron, J. J., and R. D. Larter (1998), Late Cretaceous to early Tertiary subduction history of the Antarctic Peninsula, *J. Geol. Soc. London*, *155*, 255–268, doi:10.1144/gsjgs.155.2.0255.

McKenzie, D. P. (1978), Some remarks on the development of sedimentary basins, *Earth Planet. Sci. Lett.*, *40*, 25–32.

Menard, H. W. (1978), Fragmentation of the Farallon Plate by pivoting subduction, *J. Geol.*, *86*, 99–110.

Mooney, W. D., M. E. Gettings, H. R. Blank, and J. H. Healy (1985), Saudi Arabian seismic-refraction profiles: A traveltime interpretation of crustal and upper mantle structure, *Tectonophysics*, *111*, 173–246.

Morley, C. K., W. A. Wescott, D. M. Stone, R. M. Harper, S. T. Wigger, and F. M. Karanja (1992), Tectonic evolution of the northern Kenyan Rift, *J. Geol. Soc. London*, *149*, 333–348.

Muller, R. D., K. Gohl, S. C. Cande, B. A. Goncharov, and A. V. Golynsky (2007), Eocene to Miocene geometry of the West Antarctic Rift System, *Aust. J. Earth Sci.*, *54*, 1033–1045, doi:10.1080.06120090701615691.

Nielsen, T., L. De Sanatis, K. I. T. Dahlgren, A. Kuijpers, J. S. Laberg, A. Nygard, D. Praeg, and M. S. Stoker (2005), A comparison of the NW European margin with other glaciated margins, *Mar. Pet. Geol.*, *22*, 1149–1183, doi:10.1016/j.marpetgeo.2004.12.007.

Nitsche, F. O. (1998), Bellingshausen- und Amundsenmeer: Entwicklung eines Sedimentationsmodells, *Ber. Polarforschung*, *258*, 1–144.

Nitsche, F. O., S. S. Jacobs, R. D. Larter, and K. Gohl (2007), Bathymetry of the Amundsen Sea continental shelf: Implications for geology, oceanography and glaciology, *Geochem. Geophys. Geosyst.*, *8*, Q10009, doi:10.1029/2007GC001694.

Pankhurst, R. J. (1982), Rb-Sr geochronology of Graham Land, Antarctica, *J. Geol. Soc. London*, *139*, 701–711.

Prodehl, C. (1985), Interpretation of a seismic-refraction survey across the Arabian Shield in western Saudi Arabia, *Tectonophysics*, *111*, 247–282.

Renner, R. G. B., L. J. S. Sturgeon, and S. W. Garrett (1985), Reconnaissance gravity and aeromagnetic surveys of the Antarctic Peninsula, *Br. Antarct. Surv. Sci. Rep. 110*, 50 pp., British Antarctic Survey, Cambridge, U. K.

Rosendahl, B. R. (1987), Architecture of Continental rifts with special reference to East Africa, *Annu. Rev. Earth Sci.*, *15*, 443–503.

Ross, N., R. G. Bingham, H. F. J. Corr, F. Ferraccioli, T. A. Jordan, A. Le Brocq, D. M. Rippin, D. A. Young, D. D. Blankenship, and M. J. Siegert (2012), Steep reverse bed slope at the grounding line of the Weddell Sea sector in West Antarctica, *Nat. Geosci.*, *5*, 393–396, doi: 10.1038/ngeo1468.

Sander, S., M. Argyle, S. Elieff, S. Ferguson, V. Lavoie, and L. Sander (2004), The AIRGrav aiborne gravity system, in *Airborne Gravity 2004—Australian Society of Exploration Geophysicists Workshop*, edited by R. Lane, pp. 49–53, Geosci. Aust., Canberra, Australia. [Available at http://sgl.com/technicalpapers/AIRGrav_airborne_grav_sys.pdf.]

Steckler, M. S., S. Feinstein, B. P. Kohn, L. Lavier, and M. Eyal (1998), Pattern of mantle thinning from subsidence and heat flow measurements in the gulf of Suez: Evidence for the rotation of Suez andalong-strike flow from the Red Sea, *Tectonics*, *17*, 903–920.

Stock, J. M., and P. Molnar (1987), Revised history of early Tertiary plate motion in the south-west Pacific, *Nature*, *325*, 495–499.

Stock, J. M., S. C. Cande, and C. A. Raymond (1996), Updated history of the Bellingshausen Plate, *Eos Trans. AGU*, *77*(46), *Fall Meet. Suppl.*, F647.

Storey, B. C., R. J. Pankhurst, I. L. Millar, I. W. D. Dalziel, and A. M. Grunow (1991), A new look at the geology of Thurston Island, in *Geological Evolution of Antarctica*, edited by M. R. A. Thomson, J. A. Crame, and J. W. Thomson, pp. 399–403, Cambridge Univ. Press, Cambridge, U. K.

Studinger, M., and R. E. Bell (2007), Moho topography of the West Antarctic Rift System from inversion of aerogravity data: Ramifications for geothermal heat flus and ice streaming, in *Antarctica: A Keystone for a Changing World—Online Proceedings of the 10th ISAES X*, *USGS Open File Rep. 2007-1047*, edited by A. K. Cooper and C. A. Raymond, USGS and the National Academies, Wash.

Studinger, M., R. E. Bell, D. D. Blankenship, C. A. Finn, R. A. Arko, D. L. Morse, and I. Joughin (2001), Subglacial sediments: A regional geological template for ice flow in West Antarcica, *Geophys. Res. Lett.*, *28*, 3493–3496.
Studinger, M., R. E. Bell, C. A. Finn, and D. D. Blankenship (2002), Mesozoic and Cenozoic extensional tectonics of the West Antarctic Rift System from high-resolution airborne geophysical mapping, *R. Soc. N. Z. Bull.*, *35*, 563–569.
Studinger, M., R. E. Bell, and N. Frearson (2008), Comparison of AIRGrav and GT-1A airborne gravimeters for research applications, *Geophysics*, *73*, 151–161.
Suarez, M. (1976), Plate-tectonic model for the southern Antarctic Peninsula and its relation to southern Andes, *Geology*, *4*, 211–214.
Swithinbank, C., R. S. Williams, J. G. Ferrigno, K. M. Foley, C. E. Rosanova, and L. M. Dallide (2004), Coastal-change and glaciological map of the Eights Coast area, Antarctica 1972–2001, Text to accompany Map I-2600-E, *U. S. Geol. Surv. Geol. Invest. Ser. Map I-2600-E*.
Talwani, M., J. L. Worzel, and M. Landisman (1959), Rapid gravity computations for two-dimensional bodies with application to the Mendocino submarine fracture zone, *J. Geophys. Res.*, *64*, 49–59.
Tinto, K. J., and R. E. Bell (2011), Progressive unpinning of Thwaites Glacier from newly identified offshore ridge—Constraints from aerogravity, *Geophys. Res. Lett.*, *38*, L20503, doi:10.1029/2011GL049026.
Uenzelmann-Neben, G., and K. Gohl (2012), Amundsen Sea sediment drifts: Archives of stratification and climatic conditions, *Mar. Geol.*, *229–302*, 51–62, doi:10.1016/j.margeo.2011.12.007.
Uenzelmann-Neben, G., and K. Gohl (2014), Early glaciation already during the Early Miocene in the Amundsen Sea, Southern Pacific: Indications from the distribution of sedimetary sequences, *Global Planet. Change*, *120*, 92–104, doi:10.1016/j.gloplacha.2014.06.004.
Weissel, J. K., D. E. Hayes, and E. M. Herron (1977), Plate tectonics synthesis: The displacements between Australia, New Zealand, and Antarctica since the late Cretaceous, *Mar. Geol.*, *25*, 231–277.
Wellner, J. S., A. L. Lowe, S. S. Shipp, and J. B. Anderson (2001), Distribution of glacial geomorphic features on the Antarctic continental shelf and correlation with substrate: Implications for ice behavior, *J. Glaciol.*, *47*, 397–411.
Wellner, J. S., D. C. Heroy, and J. B. Anderson (2006), The death mask of the Antarctic Ice Sheet: Comparison of glacial geomorhic features across the continental shelf, *Geomorphology*, *75*, 157–171, doi:10.1016/j.geomorph.2005.05.015.
Wessel, P., and W. H. F. Smith (1998), New improved version of Generic Mapping Tools released, *Eos Trans. AGU*, *79*, 579.
Winberry, J. P., and S. Anandakrishnan (2004), Crustal structure of the West Antarctic rift system and Marie Byrd Land hotspot, *Geology*, *32*, 997–980, doi:10.1130/G20768.1.
Wobbe, F., K. Gohl, A. Chambord, and R. Sutherland (2012), Structure and breakup history of the rifted margin of West Antarctica in relation to Cretaceous separation from Zealandia and Bellingshausen plate motion, *Geochem. Geophys. Geosyst.*, *13*, Q04W12, doi:10.1029/2011GC003742.
Wright, A. P., et al. (2014), Sensitivity of the Weddell Sea sector ice streams to sub-shelf melting and surface accummulation, *Cryosphere*, *8*, 2119–2134, doi:10.5194/tc-2119-2014.
Yegorova, T., and V. Bakhmutov (2013), Crustal structure of the Antarctic Peninsula sector of the Gondwana margin around Anvers Island from geophysical data, *Tectonophysics.*, *585*, 77–89.
Yegorova, T., V. Bakhmutov, T. Janik, and M. Grad (2011), Joint geophysical and petrological models for the lithosphere structure of the Antarctic Peninsula continental margin, *Geophys. J. Int.*, *184*, 90–110, doi:10.1111/j.1365-246X.2010.04867.x.

[Journal of Geophysical Research, Solid Earth

Supporting Information for

Resolving Bathymetry from Airborne Gravity along Greenland Fjords

Alexandra Boghosian[1], Kirsty Tinto[1], James R. Cochran[1], David Porter[1], Stefan Elieff[2],

Bethany L Burton[3], Robin E. Bell[1]

1. Lamont-Doherty Earth Observatory of Columbia University, Palisades, NY USA

2. Sander Geophysics Ltd., Ottawa Canada

3. U. S. Geological Survey, Denver, CO USA

Contents of this file

Additional Supporting Information (Files uploaded separately)

Figure S7. Profiles showing our preferred model along 54 glaciers and fjords in Greenland. For each profile, the upper panel shows the observed gravity anomalies (red line), the calculated gravity anomalies (blue line) resulting from our model, and the observed magnetic anomalies (gray line). The middle panel shows the lidar-determined ice or water surface (blue line), the radar-determined ice base (red line) and our gravity-determined bed and bathymetry (black line). Grounding line positions are shown as a red dot on the ice surface. The lower panel shows the radar echogram for the modeled line. Elevation is with respect to WGS84 ellipsoid.

Additional information displayed on particular profiles is annotated on the figure. The colored stars on profiles for 160.120 (Kangiata Nunaata Sermia) and 162.100 (Narsap

Sermia) show the locations of the gravity-determined bed from an OIB crossing line that were used for the reference density columns in the respective profiles. Purple line and green dots in profile 3.120 (Jakobshavn) show acoustic bathymetry [*Schumann et al.*, 2012] and individual soundings [*Holland et al.* 2008] in the fjord. The green lines in profiles 20.111 (Upernavik North), 147.121 (A.P. Bernstorff) and 151.101 (Heimdal) show radar from 2014 used to constrain the gravity models. Dashed red lines in profiles 71.120 (Newmann Bugt) and 193.110 (Petermann) show the IceBridge measured gravity, and solid red line shows the regionally corrected gravity used in the model.

Introduction

We here further describe the results of the gravity inversions on a region-by-region basis and present profiles along each of the 54 glaciers and fjords. We will refer to the profiles by the fjords and glaciers that they span. We assign a unique number to each glacier and also to each profile along the glacier. For each profile, the glacier ID is given before the decimal point. The first two digits after the decimal point refer to the year IceBridge collected the data, and the third digit is the profile number along the glacier for that year. For example, the profile along Store Glacier in Figure S7 is indexed as 9.120. In this case, 9 is the glacier ID, 12 refers to the year in which the data were collected (2012), and 0 indicates it is the first profile along the glacier during that year. We will also generally refer to the glacier by name in the text.

In Figure S7, we present our preferred model for each fjord, but all model results are found at NSIDC. Our preferred model solution is one with smooth bathymetry and topography, a low RMS error between observed and calculated gravity, and topographic shapes that match those of the gravity signal (Figure 2). We also take into account agreement with offshore constraints and, within these constraints, attempt to maximize the total length of bathymetry modeled.

Text S1.

1. Southwest

In this region (Figure 1), the modeled dataset includes four glaciers that flow towards Godthabsfjord in southwest Greenland (Figure S1). Three are marine-terminating, Kangiata Nunaata Sermia (KNS) (160), Narsap Sermia (162), and Akullersuup Sermia

(161), and one is land-terminating, Saqqap Sermersua (207). The flight down Saqqap Sermersua continues into the marine segment of the fjord. The gravity models contribute a total of 167 km of subice topography and 88 km of bathymetry, and provide grounding line depths of 174 m for KNS and 320 m for Narsap Sermia (Table 1).

Throughout this region, radar returns from the bed are particularly sparse, and the bed is not constrained by radar within ~50 km of the grounding line of the marine-terminating glaciers. To create consistent models of these four glaciers, we used intersecting flight lines to provide reference density columns when radar constraints were not available (Figure S1). We selected a reference density column based on observed or modeled topography or bathymetry at the intersection point. The only radar data along KNS is in the very upper reaches of the glacier and does not provide a suitable location for a reference density column. However, the line along KNS and Godthabsfjord intersects a coast-parallel IceBridge flight (line 9160.120) (Figure S1). We modeled this line to obtain bathymetry in Godthabsfjord and bed topography beneath Narsaap Sermia, and used the intersections of this line with the lines along KNS and Narsaap Sermia to model both glaciers. The red star (Figure S1) denotes the reference density column for KNS, enabling us to model 34 km of bathymetry in Godthabsfjord and 28 km of bed topography beneath KNS. Similarly, using a reference density column at the blue star (Figure S1) for Narsaap Sermia allowed us to model 5 km of bathymetry and 51 km of bed topography.

The radar on the line along Akullersuup Sermia recovered no ice-thickness, which would ordinarily preclude a gravity model. No gravity data were recovered at the intersection with the crossing line, but the flight path along Akullersuup Sermia continues into Godthabsfjord, and is coincident with a line down KNS. We were able to select a reference density column based on these coincident paths and model 35 km of bathymetry and 37 km of subice topography along the Akullersuup Sermia line.

This procedure increases the uncertainty in the modeled bathymetry and bed since the reference density column was determined from modeled bathymetry and is subject to the uncertainty inherent in the inversion.

2. West

In this region (Figure 1), we modeled seven fjords (Figure S2). The southernmost cluster near Disko Bay includes Jakobshavn (3), Eqip Sermia (5), and Store Glacier (9). To the north of Disko Bay, we modeled Kangerlusuup Sermersua (14), Rink Isbrae (15), Umiammakku Isbrae (16), and Inngia Isbrae (17). In these seven profiles, the gravity models contribute 204 km of subice topography and 353 km of bathymetry. The models provide grounding line depths for Jakobshavn, Eqip, Store, Kangerlusuup, and Rink (Table 1). Jakobshavn has the deepest grounding line depth in this group at 642 m, while Rink has the deepest fjord depth at 1254 m.

The 2012 IceBridge line down Jakobshavn follows the centerline of the glacier, and is the longest of three modeled lines in this region, with a total flight path length of 216 km. In spite of this gravity coverage, Jakobshavn probably represents a worse case for gravity inversion. The bed beneath Jakobshavn is notoriously difficult to image with radar (see discussion in *Gogineni et al.* [2014]). The OIB radar lines from 2010 to 2012 only resolve 13 km of subice topography landward of the deep glacial trough and our gravity inversion must model topography and bathymetry extending 200 km from the reference density column.

Gogineni et al. [2014] produced a bed map for Jakobshavn by using advanced processing techniques to reprocess radar data along and across Jakobshavn collected from a relatively slow-flying Twin Otter aircraft from 2005 to 2009. Their bed depths sampled along our gravity line are shown on the lower panel in Figure S2. The gravity-determined and radar-determined beds agree well in the uppermost portion of the glacier, where the gravity-determined bed is constrained by OIB radar. However, as soon as the line enters the trough, the gravity-determined and *Gogineni et al.* [2014] bed diverge sharply, with the radar-determined bed 400-700 m deeper. There are no OIB radar returns in this region. About 10 km landward of the calving front, the *Gogineni et al.* [2014] bed shallows suddenly by 500 m and is consistent with the gravity-determined bed. In the fjord, the gravity-determined bathymetry is in reasonable agreement with 10 bathymetric soundings acquired by *Holland et al.* [2008] (Figure S2), although a quantitative comparison is not meaningful since the soundings are not along the aircraft track and had to be projected onto our profile. Just outside of the fjord, our gravity-derived bathymetry shows a distinct shallow ridge. However, this ridge is deeper than bathymetry measured

by swath-mapping [*Schumann et al.*, 2012] (Figure S2). This offset between modeled and observed bathymetry suggests the shallow area is made up of sediments and probably represents a moraine.

The discrepancy between the *Gogineni et al.* [2014] radar-determined ice base and the gravity-determined bed likely results from the location of the reference density column, which is landward of the deep glacial trough and therefore not representative of conditions within the trough where the discrepancy is the greatest. The differing conditions between the reference column location and the trough could result from changes in sediment thickness or in geology [*Block*, 2011] that would impact the density column. The discrepancy highlights the important of a reference density column close to the grounding line and within the glacial trough.

3. Northwest

The modeled dataset includes fourteen fjords in northwest Greenland (Figure 1, Figure S3). In the Upernavik region, we model Upernavik South (18), Upernavik North (20) and Upernavik Northwest (301). To the north, we model Alison Gletcher (31), Sverdrup Gletscher (40), Nansen Gletscher (41), Kong Oscar Gletscher (44), Rink Gletscher (48), Docker Smith Glacier West (194), Yngvar Nielsen Brae (55), Savissuaq Gletscher (57), and Nigerlikasik (58). We also model a pair of glaciers that flow into Inglefield Gulf, Heilprin Gletscher (63) and Tracy Gletscher (64). In these fourteen profiles, the gravity models contribute 71 km of subice topography and 312 km of bathymetry. The gravity model provides grounding line depths in Upernavik South, Upernavik North, Alison, Nansen, Savissuaq, Nigerlikasik, Heilprin, and Tracy. The maximum fjord depth modeled in this region is Upernavik North at 1137 m. Nansen, Kong Oscar and Tracy all have minimum fjord depths that are shallower (i.e. a difference of over 200 m) than their grounding line depths (Table 1).

A total of seven lines were modeled for Tracy and Heilprin. The flights down Tracy and Heilprin are reoccupied paths onshore but diverge offshore, providing a total of 81 km of new bathymetry in Inglefield Gulf (Figure S3). The models for Tracy and Heilprin give grounding depths of 624 m and 383 m respectively. *Porter et al.* [2014] used the models for Tracy and Heilprin to analyze the impact of grounding line depth on mass

loss, noting that Tracy, with the deeper grounding line, has experienced greater mass loss. The model also indicates that Heilprin may have a short floating tongue.

4. North

We modeled eleven fjords in north Greenland (Figure 1), including Humboldt Glacier (70), Petermann Glacier (193), Newman Bugt (71), Steensby Gletscher (72), Ryder Gletscher (73), C. H. Ostenfeld Gletscher (75), Marie Sophie Gletscher (78), Academy Gletscher (79), Hagen Brae (80), Nioghalvfjerdsfjorden (79 North) (500), and five lines from the IceBridge grid over Zachariae Isstrom (82) (Figure S4). Radar images the bed up to the grounding line in each glacier, and the gravity models contribute a total of 779 km of bathymetry in the fjords. IceBridge flights down glaciers in north Greenland tend to be longer and straighter than in other areas, resulting in higher quality gravity data.

Bathymetry in Petermann Fjord is constrained by ship-based bathymetry in the outer part of the fjord [*Johnson et al.*, 2011]. *Tinto et al.* [2015] used multiple non-coincident gravity and magnetics lines along the fjord along with the shipboard bathymetry to constrain a detailed geological model within the fjord. The gravity-derived bathymetry model reveals a 600 m deep sill 25 km seaward of the grounding line, under the floating ice tongue.

5. Northeast

We modeled seven fjords in northeast Greenland (Figure 1), including in the Geike region (Figure S5). North of Geike we modeled Gerard de Geer Gletscher (88), Morell Gletscher (90), F. Graae Gletscher (91), and Daugaard-Jensen Gletscher (92). In the Geike region, we modeled Sydbrae (101), Bredegletscher (102), and Dendritgletscher (104). In these seven profiles, the gravity models contribute 148 km of new subice topography and 167 km of new bathymetry. The gravity models provide grounding line depths for Gerard de Geer, Morell, F. Graee, Sydbrae, and Bredegletscher. Of profiles to the north of Geike, F. Graae has the deepest grounding line at 560 m, and Sydbrae has the deepest grounding line of the three profiles on the Geike Peninsula at 430 m. The maximum fjord depth of all profiles in this region is 1377 m in F. Graae. Morell and F. Graae both have minimum fjord depths shallower than their grounding line depths.

6. Southeast

We modeled eleven fjords in southeast Greenland (Figure 1), including two in Sermilik Fjord on the southern side of the Geike Peninsula (Figure S6). In Sermilik Fjord, we modeled Helheim Gletscher (133) and Midgaard Glacier (131). We also modeled Ikertivaq North (135), Koge Bugt (140), Umiivik Fjord (144), Graulv (145), A.P. Bernstorff Gletscher (147), Skinfaxe (149), Heimdal Gletscher (151), Puisortoq North (200), and Puisortoq South (700). In this region, the gravity models contribute 282 km of new subice topography, 252 km of new bathymetry, and provide new grounding line depths of Puisortoq South, Helheim, and A.P. Bernstorff. Of the eleven profiles, Helheim has the deepest grounding line depth of 621 m, and A.P. Bernstorff has the deepest fjord depth of 1053 m. Both Helheim and A.P. Bernstorff have minimum fjord depths shallower than their grounding line depths.

The flight across Sermilik fjord in 2012 was used to model both Helheim and Midgaard. Radar constraints were only available in Helheim, but due to the flight's relatively straight geometry and continuous gravity measurements, we modeled the bathymetry in front of the two glaciers and bed topography along Midgaard (Figure S6), although the Midgaard grounding line is ~70 km away from the reference density column.

Radar bed returns from 2010 to 2012 were insufficient for the modeling of two additional glaciers, A.P. Bernstorff and Heimdal. Flight paths down both glaciers in 2014, on which gravity data was not collected, were coincident with flight paths from 2010 to 2012. We used radar bed returns from 2014 to model these glaciers. In 2014, radar imaged the bed close to the grounding lines of these glaciers, which is one of our criteria for a reference density column selection. Radar from 2014 was used in models 20.110, 20.111, 147.110, 147.111, 147, 120, 147.121, 151.101 and 151.110.

Figure S1

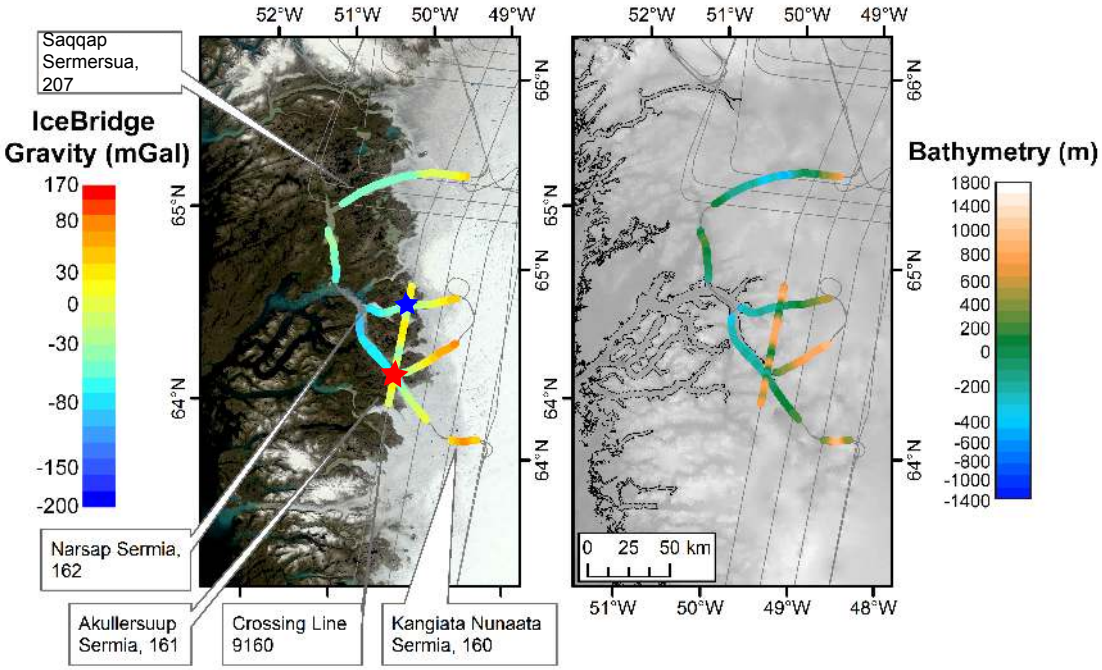
52°W
51°W
50°W
49°W
48°W
66°N
65°N
64°N
Saqqap Sermersua, 207
IceBridge Gravity (mGal)
170
80
30
0
-30
-80
-150
-200
Bathymetry (m)
1800
1400
1000
800
600
400
200
0
-200
-400
-600
-800
-1000
-1400
Narsap Sermia, 162
Akullersuup Sermia, 161
Crossing Line 9160
Kangiata Nunaata Sermia, 160
0 25 50 km

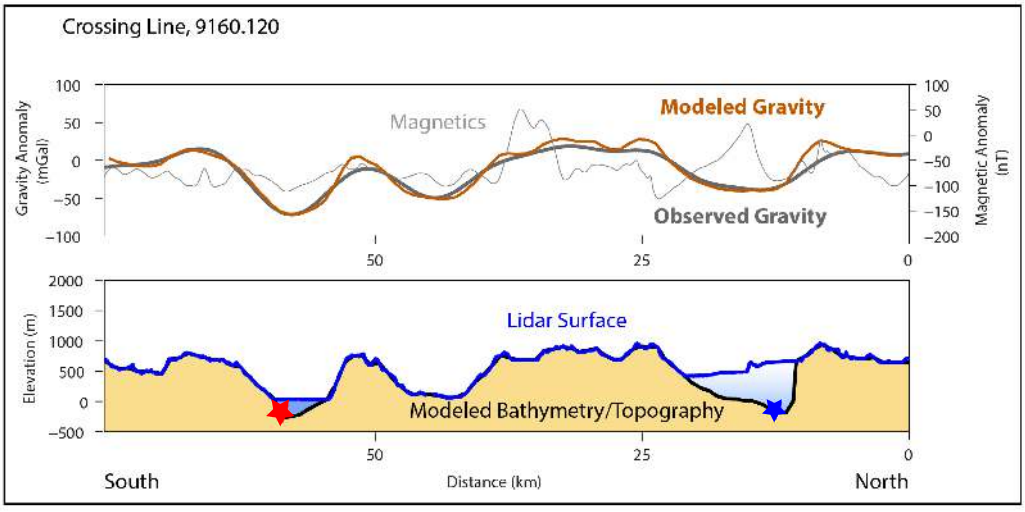
Crossing Line, 9160.120
Gravity Anomaly (mGal)
Magnetic Anomaly (nT)
Magnetics
Modeled Gravity
Observed Gravity
Elevation (m)
Lidar Surface
Modeled Bathymetry/Topography
South
Distance (km)
North

Figure S1 Maps of IceBridge gravity, modeled bathymetry and subice topography, and model of an across-fjord-axis line in southwest Greenland. Top left panel shows all IceBridge flights from 2010 to 2012 in gray, and gravity anomalies along the fjord-axis flights as well as the across-fjord-axis line shown in the bottom panel. Red and blue stars show the intersection of the across-fjord-axis line with intersecting lines along Kangiata Nunaata Sermia (160) and Narsap Sermia (162). Background is 250 m MODIS Terra image from 2013. Top right panel shows all IceBridge flights from 2010 to 2012 in gray, and bathymetry along the modeled portions of the profiles. Background is the *Bamber et al.* [2013] bed elevation and bathymetry grid. Lower panel shows the across-fjord-axis line providing reference density columns for intersecting lines, Kangiata Nunaata Sermia (red star) and Narsap Sermia (blue star). All maps are shown in a polar stereographic projection (EPSG 3413).

Figure S2

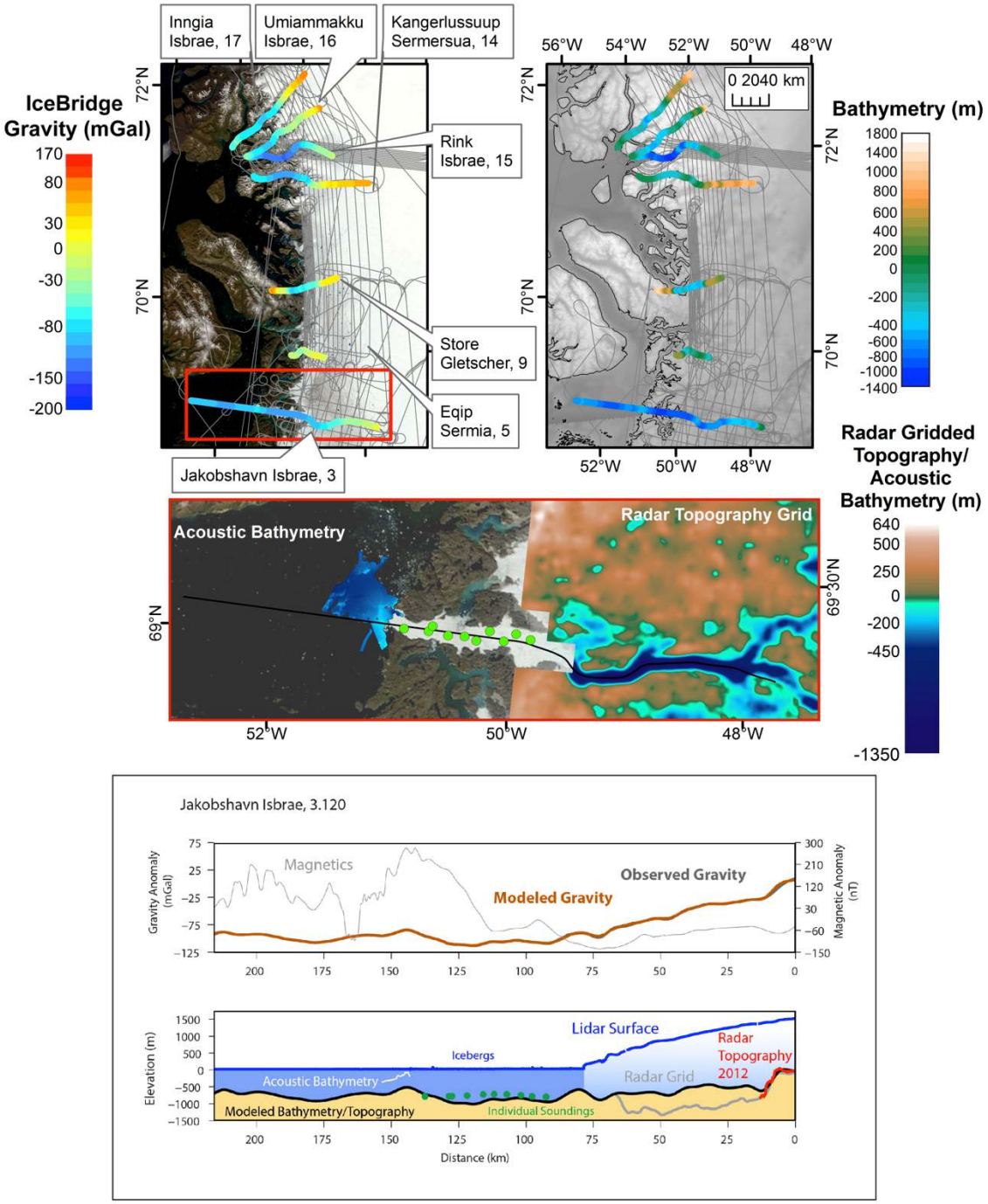

Figure S2 Maps of IceBridge gravity (upper left), and modeled bathymetry and subice topography (upper right) in west Greenland as in Figure S1. Middle panel shows close-up view of the area in the red box, with bed derived from reprocessed radar data [*Gogineni et al.*, 2014], acoustic bathymetry grid from just outside the fjord [*Schumann et al.*,

2012], and individual soundings in the fjord [*Holland et al.*, 2008] (green dots). Lower panel shows an OIB line along Jakobshavn Isbrae (3.120) showing gravity-derived subice topography and bathymetry. Red and blue lines are OIB radar and lidar respectively from 2012, black line is gravity-modeled bathymetry, gray and white lines show the radar grid and offshore bathymetry grid respectively sampled onto the line, and green dots show point measurements of bathymetry measurements in the fjord projected onto the line.

Figure S3

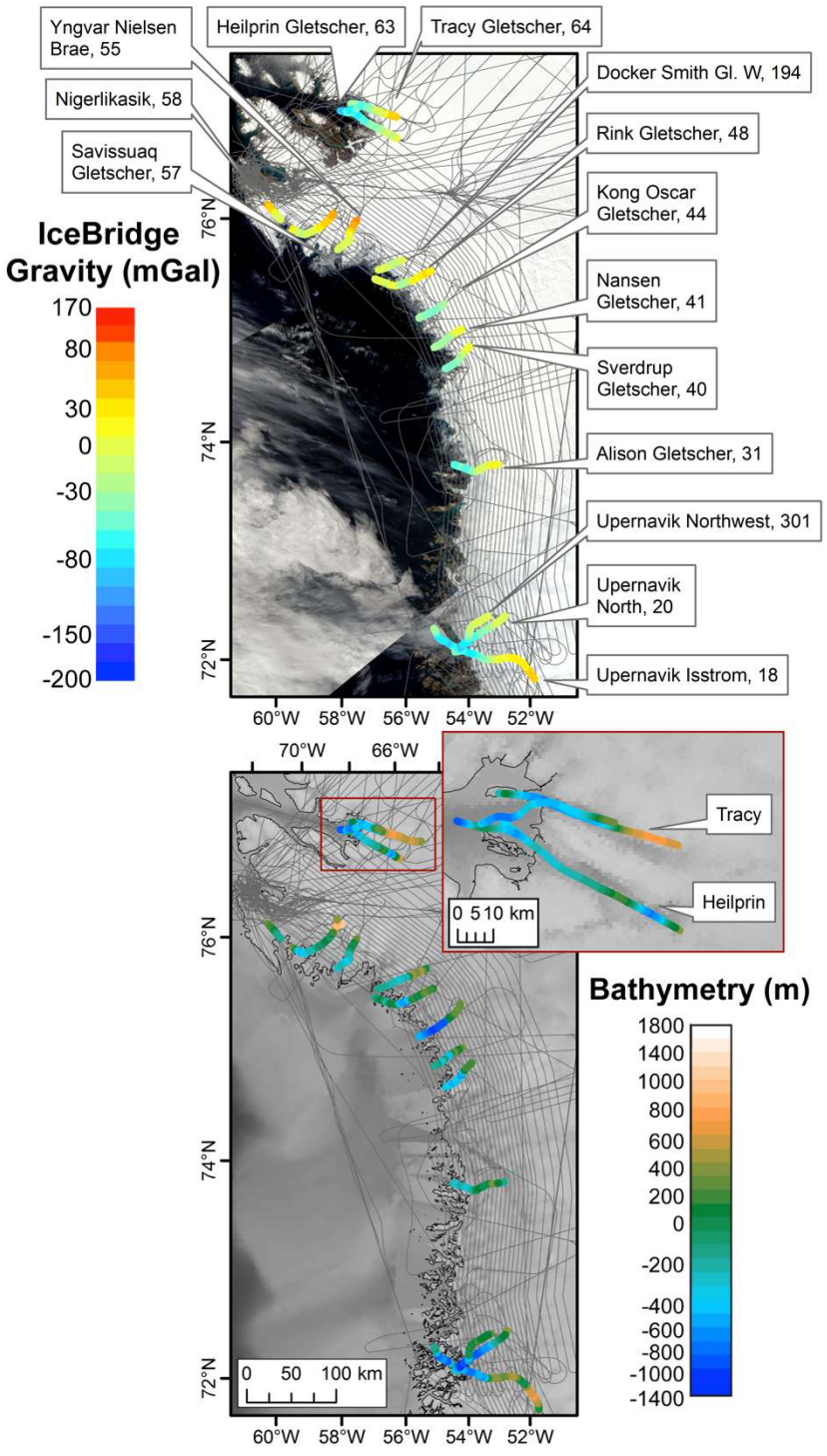

Figure S3 Maps of IceBridge gravity, modeled bathymetry and subice topography in northwest Greenland. Upper and lower panels show gravity and bathymetry, as in Figure S1. Upper right corner of the lower panel is a close-up view of the area in the red box,

showing bed topography and modeled bathymetry for all seven OIB profiles along Tracy and Heilprin glaciers.

Figure S4

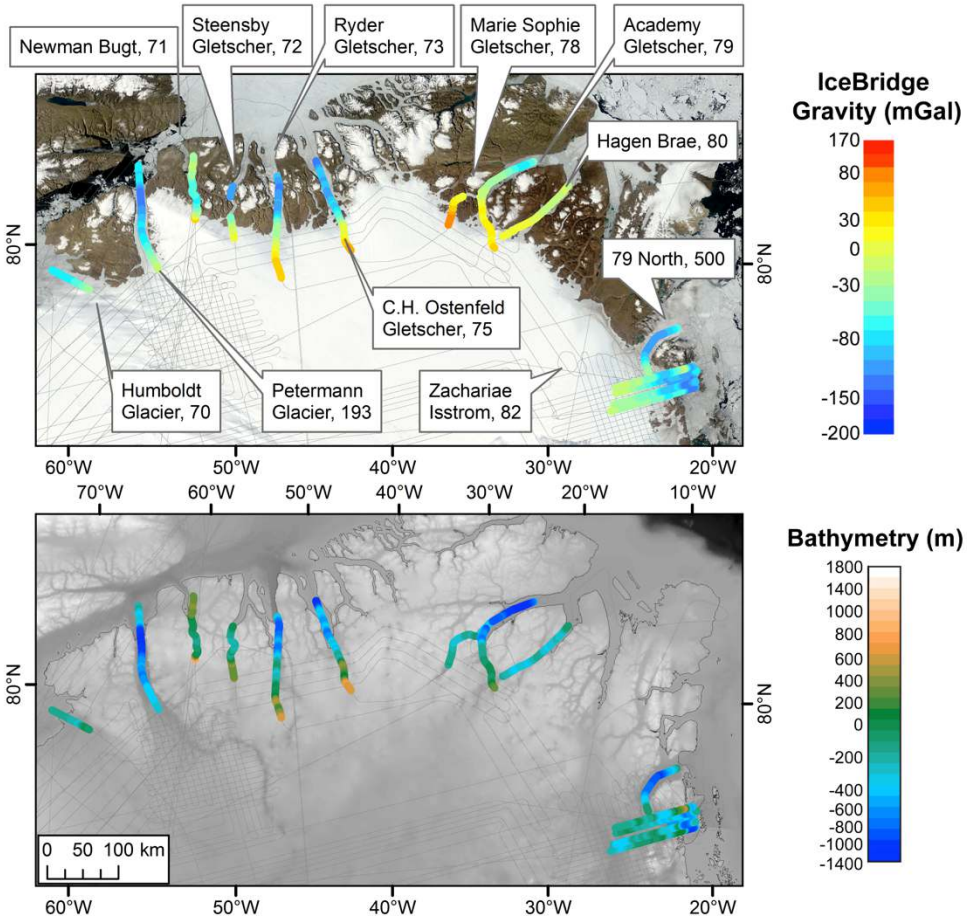

Figure S4 Maps of IceBridge gravity, modeled bathymetry and subice topography in north Greenland. Upper and lower panels show gravity and bathymetry as in Figure S1.

Figure S5

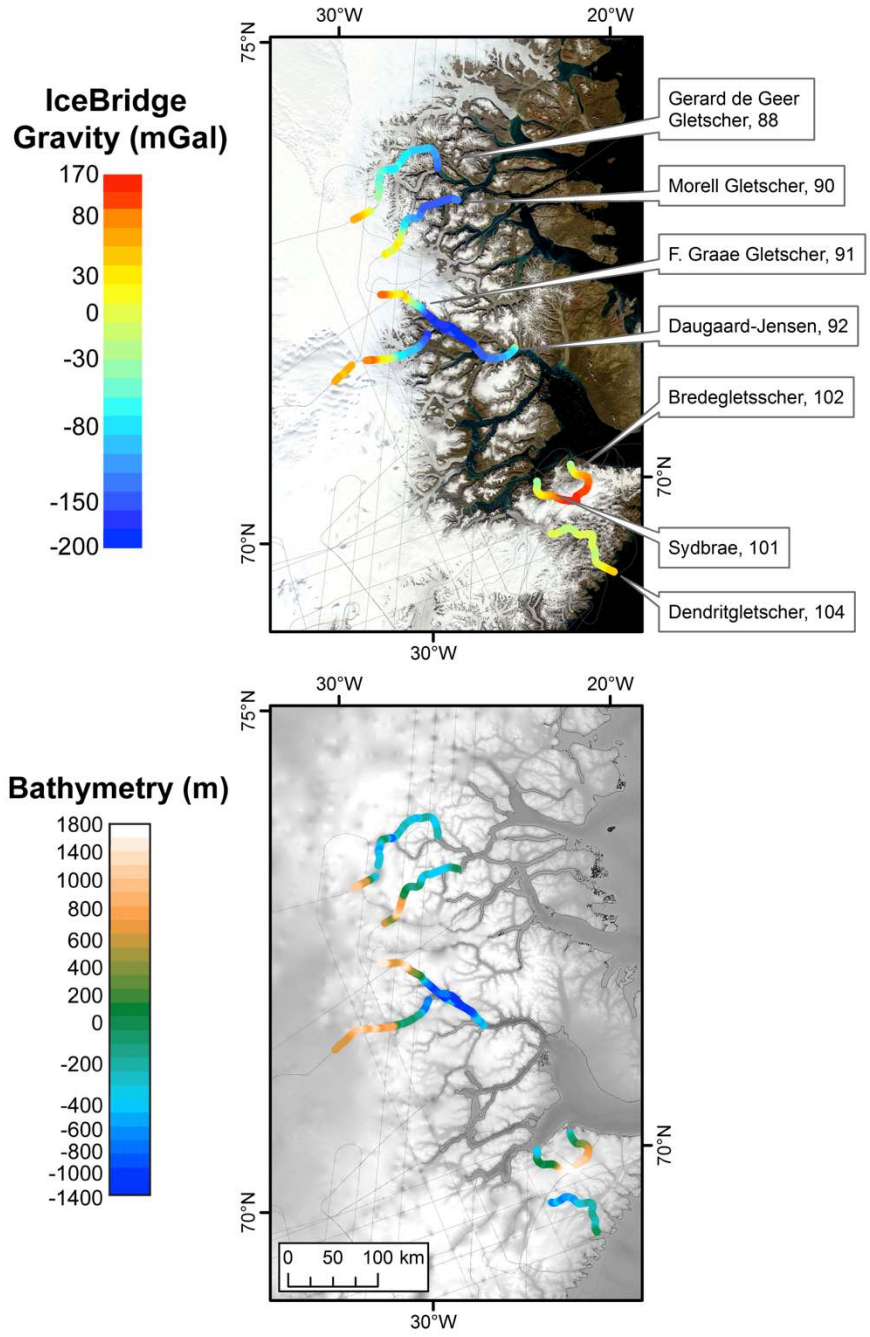

Figure S5 Maps of IceBridge gravity, modeled bathymetry and subice topography in northeast Greenland. Upper and lower panels show gravity and bathymetry as in Figure S1.

Figure S6

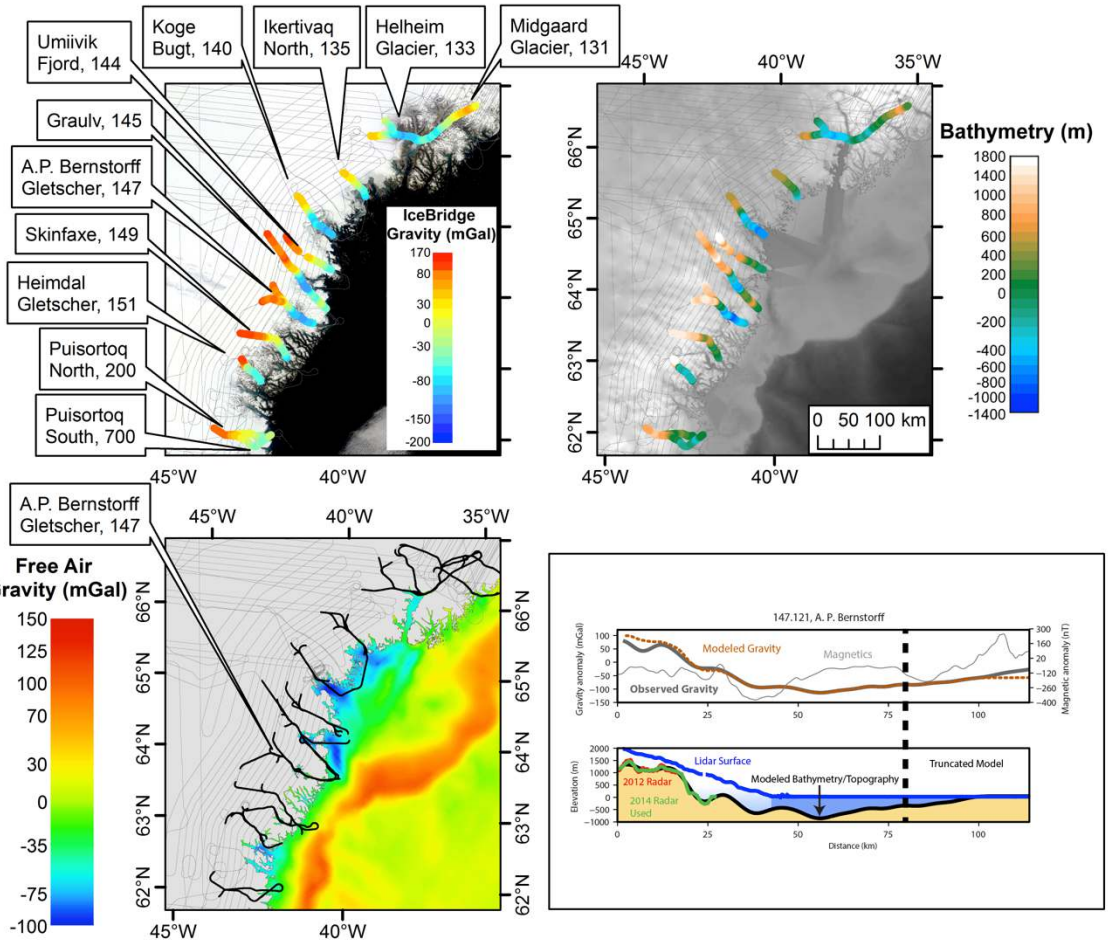

Figure S6 Maps of IceBridge gravity, modeled bathymetry and subice topography in southeast Greenland. Top left and right panels show gravity and bathymetry as in Figure S1. Lower left panel shows regional gravity [*Sandwell et al.*, 2007] in southeast Greenland rising offshore, with IceBridge along-fjord axis flights from 2010 to 2012 in

black. Lower right panel shows the observed and calculated gravity along with the magnetics for A.P. Bernstorff. Dashed line indicates the point where the magnetic anomaly changes character. We truncate the model seaward of this point where the modeled bathymetry becomes unrealistically shallow.

References

Bamber, J. L., et al. (2013), A new bed elevation dataset for Greenland, *The Cryosphere*, *7*, 499-510, doi:doi:10.5194/tc-7-499-2013.

Block, A. E. (2011), Geophysical perspectives of subglacial settings and their influence on glacial dynamics, 129 pp, Columbia University, New York.

Gogineni, P., et al. (2014), Bed topography of Jakobshaven Isbrae, Greenland, and Byrd Glacier, Antarctica, *J. Glaciology*, *60*(223), 813-833, doi:doi:10.3189/2014JoG14J129.

Holland, D. M., R. H. Thomas, B. De Young, M. H. Ribergaard, and B. Lyberth (2008), Acceleration of Jakobshavn Isbrae triggered by warm subsurface ocean waters, *Nature Geoscience*, *1*, 659-664, doi:doi:10.1038/ngeo316.

Johnson, H. L., A. Müenchow, K. K. Falkner, and H. Melling (2011), Ocean circulation and properties in Petermann Fjord, Greenland, *Journal of Geophysical Research*, *116*, doi:doi:10.1029/2010JC006519.

Porter, D., K. J. Tinto, A. Boghosian, J. R. Cochran, R. E. Bell, S. Manizade, and J. Sonntag (2014), Bathymetric control of tidewater glacier mass loss in northwest Greenland, *Earth and Planetary Science Letters*, *401*, 40-46, doi:doi:10.1016/j.epsl2014.05058.

Schumann, K., D. Volker, and W. R. Weinrebe (2012), Acoustic mapping of the Illulisat Ice Fjord mout, West Greenland, *Quat. Sci. Rev.*, *40*, 78-88, doi:doi:10.1016/j.quascirev.2012.02.016.

Tinto, K. J., R. E. Bell, J. R. Cochran, and A. Munchow (2015), Bathymetry in Petermann Fjord from Operation IceBridge aerogravity, *Earth and Planetary Science Letters*, *422*, 58-66, doi:doi:10.1016/.j.epsl.2015.04009.

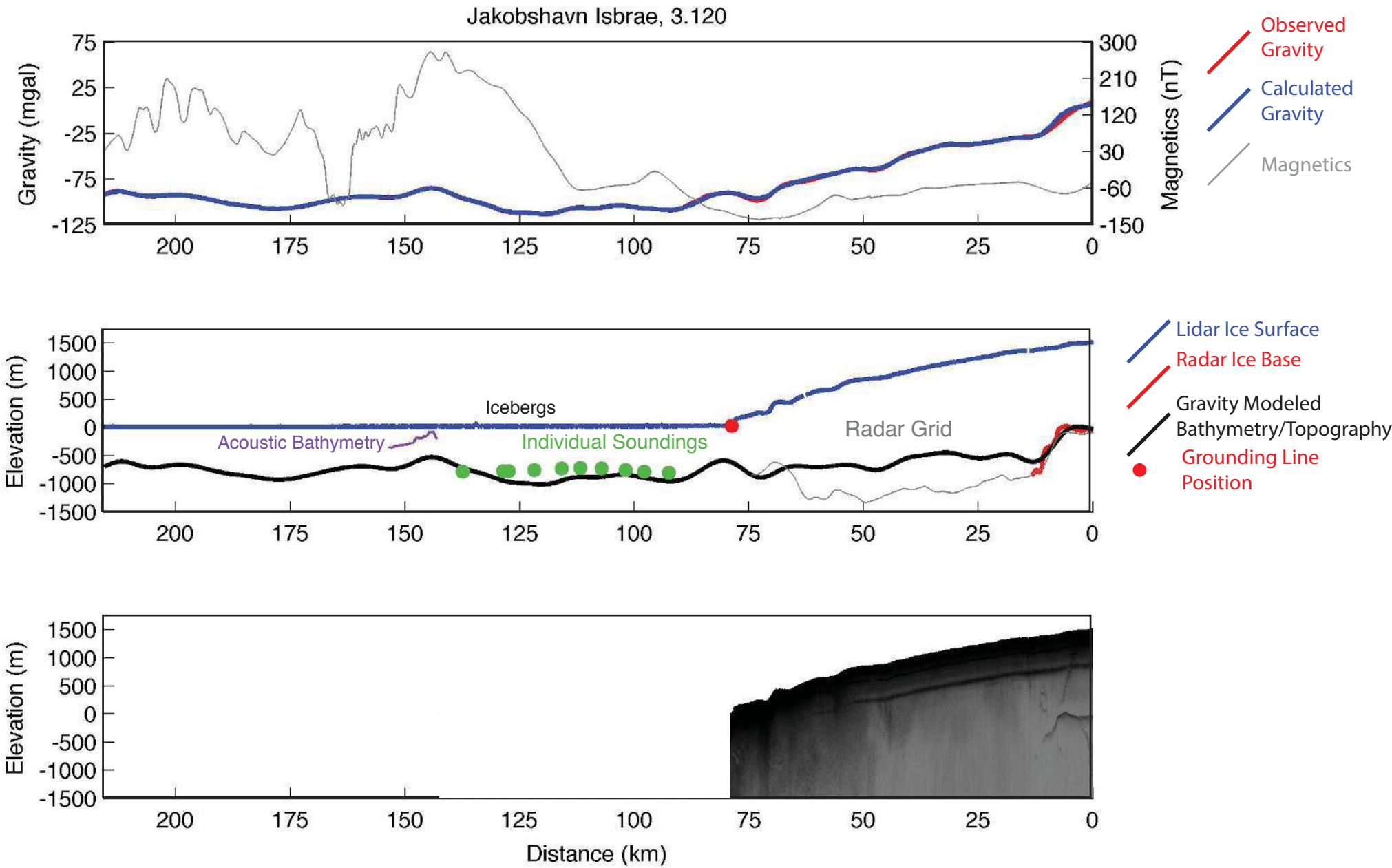
Jakobshavn Isbrae, 3.120
Gravity (mgal)
75
25
-25
-75
-125
Magnetics (nT)
300
210
120
30
-60
-150
200
175
150
125
100
75
50
25
0
Observed Gravity
Calculated Gravity
Magnetics
Elevation (m)
1500
1000
500
0
-500
-1000
-1500
Icebergs
Acoustic Bathymetry
Individual Soundings
Radar Grid
Lidar Ice Surface
Radar Ice Base
Gravity Modeled Bathymetry/Topography
Grounding Line Position
Distance (km)

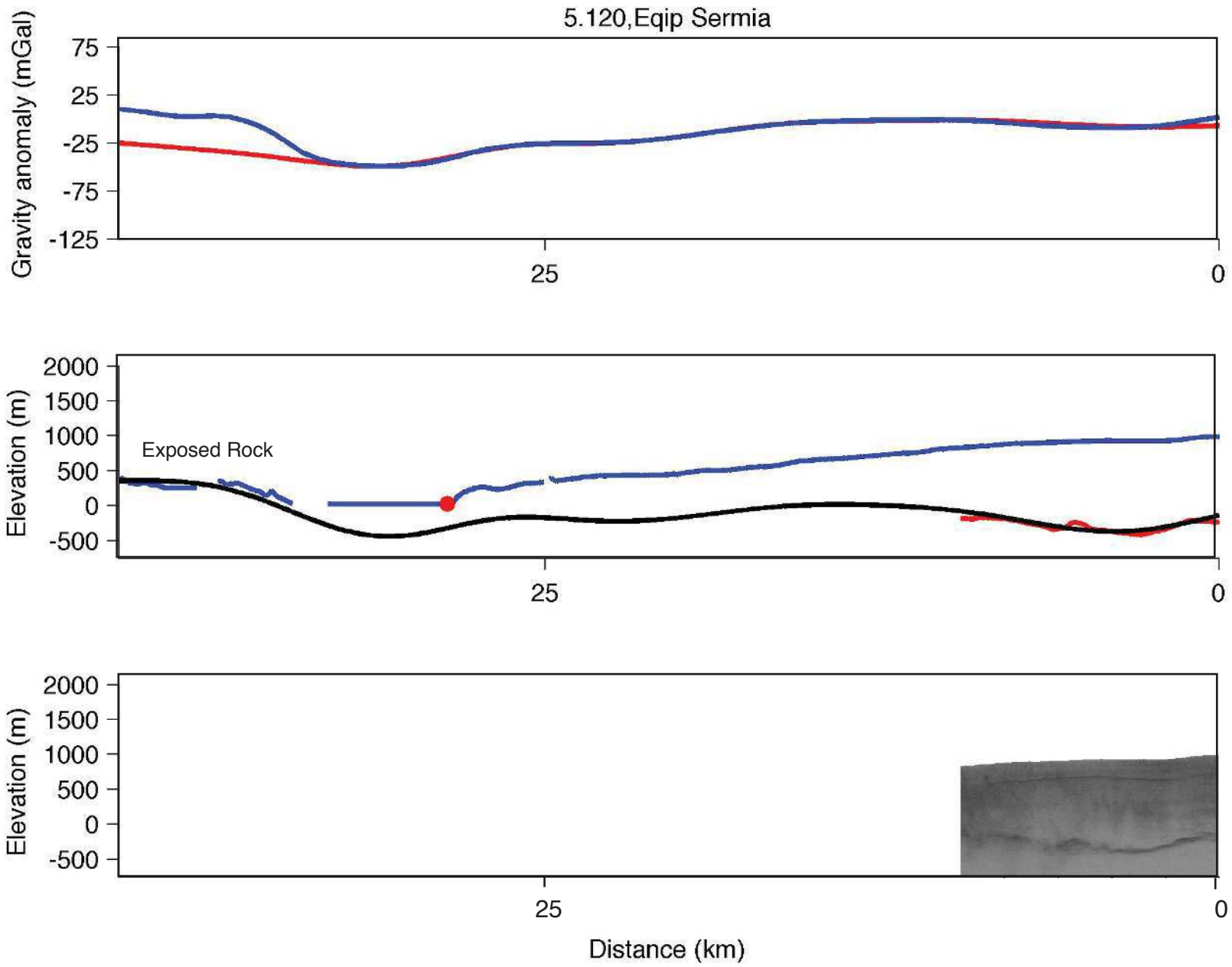
5.120,Eqip Sermia
Gravity anomaly (mGal)
75
25
-25
-75
-125
25
0
Observed Gravity
Calculated Gravity
Magnetics
Elevation (m)
2000
1500
1000
500
0
-500
Exposed Rock
25
0
Lidar Ice Surface
Radar Ice Base
Gravity Modeled Bathymetry/Topography
Grounding Line Position
Elevation (m)
2000
1500
1000
500
0
-500
25
0
Distance (km)

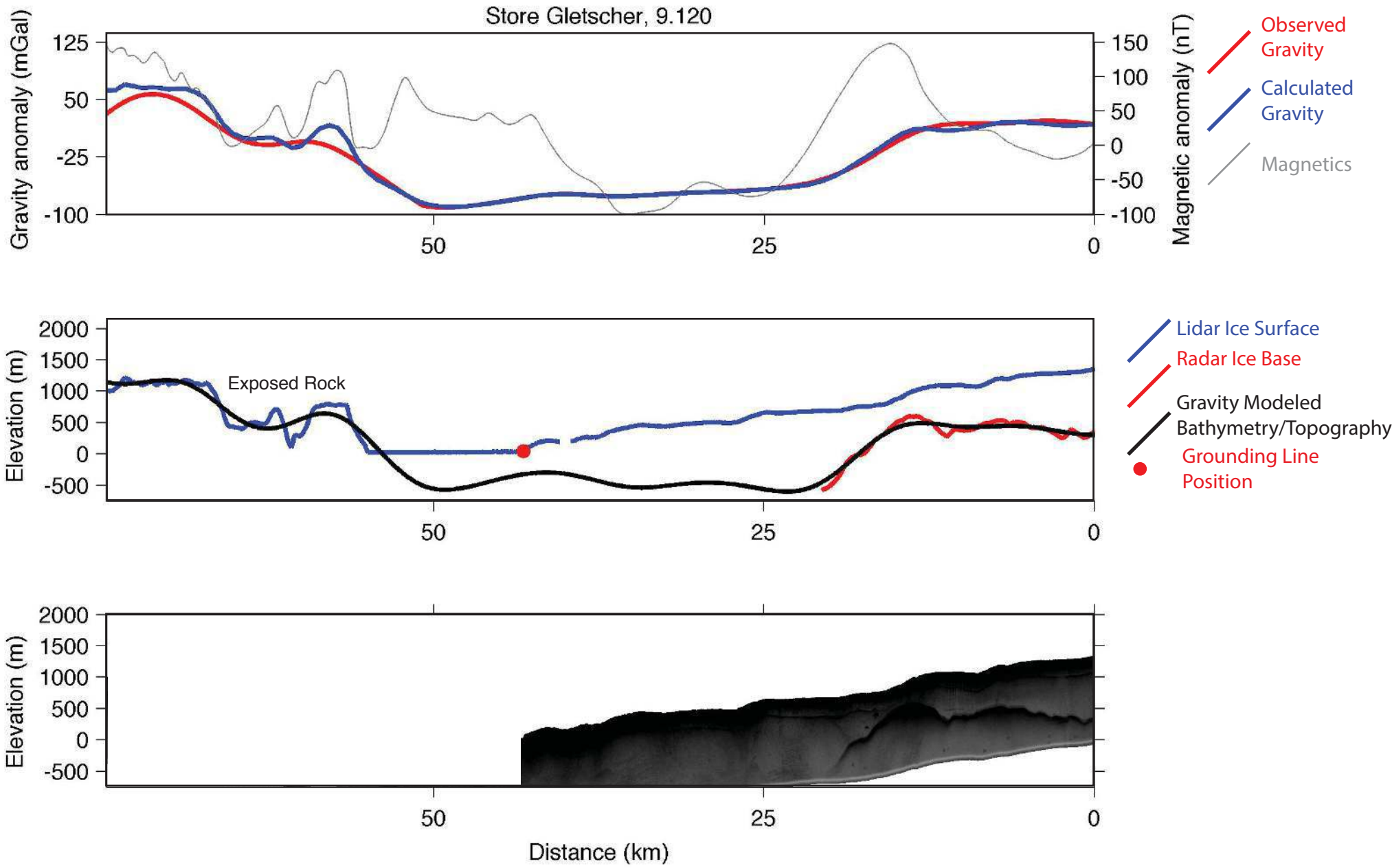
Store Gletscher, 9.120
Gravity anomaly (mGal)
125
50
-25
-100
Magnetic anomaly (nT)
150
100
50
0
-50
-100
50
25
0
Observed Gravity
Calculated Gravity
Magnetics
Elevation (m)
2000
1500
1000
500
0
-500
Exposed Rock
Lidar Ice Surface
Radar Ice Base
Gravity Modeled Bathymetry/Topography
Grounding Line Position
Distance (km)

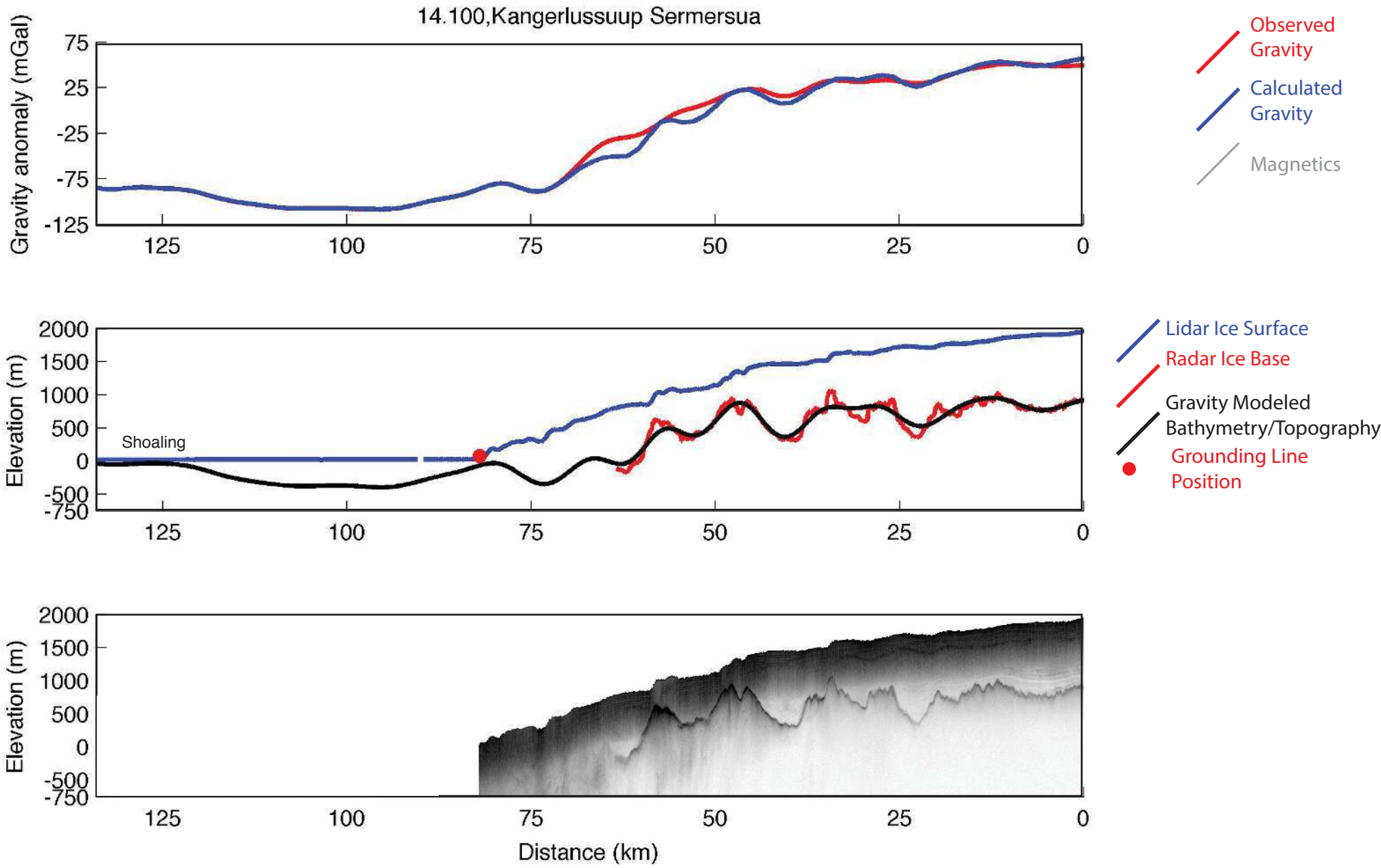
14.100,Kangerlussuup Sermersua
Gravity anomaly (mGal)
75
25
-25
-75
-125
125
100
75
50
25
0
Observed Gravity
Calculated Gravity
Magnetics
Elevation (m)
2000
1500
1000
500
0
-500
-750
Shoaling
Lidar Ice Surface
Radar Ice Base
Gravity Modeled Bathymetry/Topography
Grounding Line Position
Distance (km)

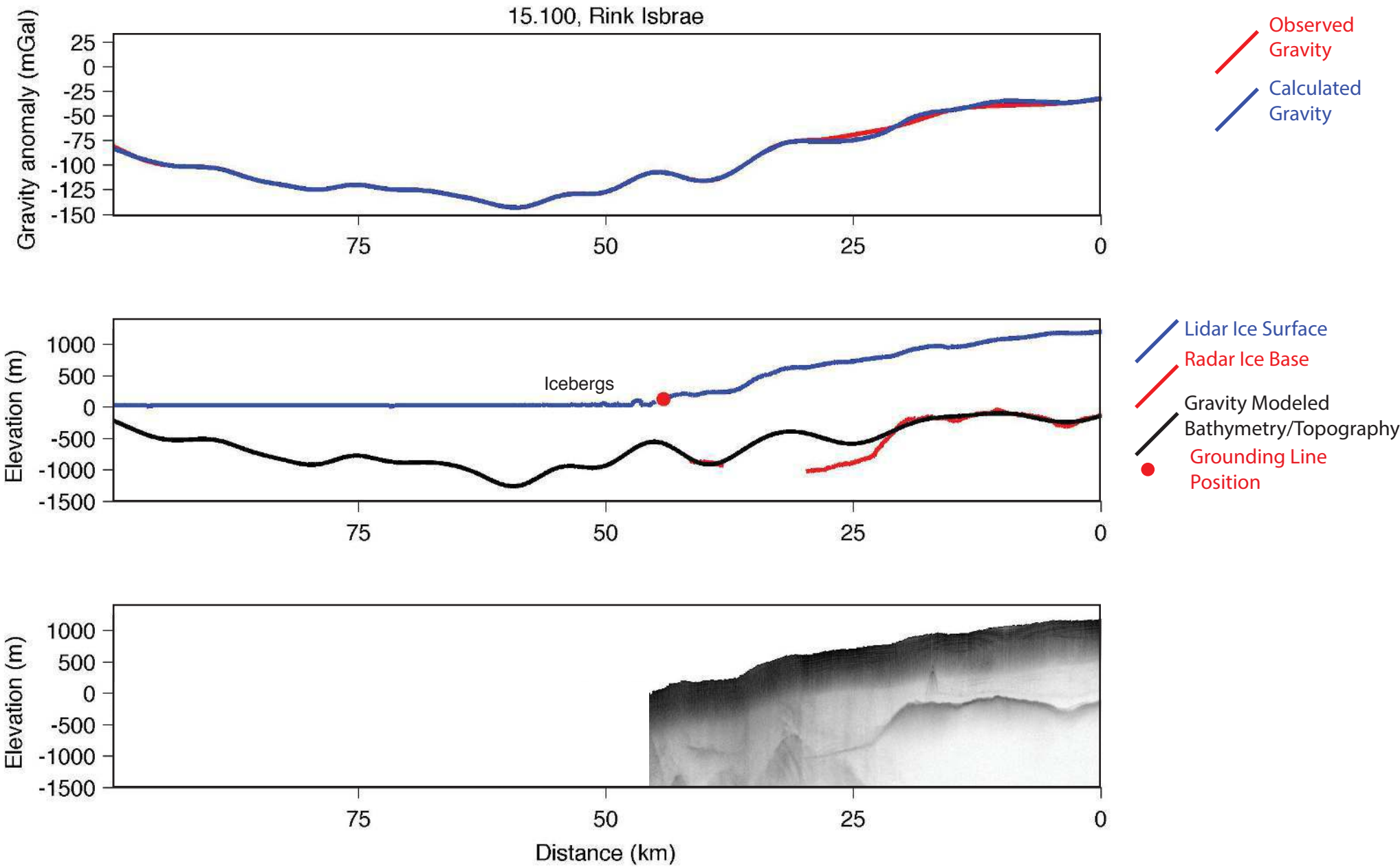
15.100, Rink Isbrae
Gravity anomaly (mGal)
25
0
-25
-50
-75
-100
-125
-150
75
50
25
0
Observed Gravity
Calculated Gravity
Elevation (m)
1000
500
0
-500
-1000
-1500
Icebergs
Lidar Ice Surface
Radar Ice Base
Gravity Modeled Bathymetry/Topography
Grounding Line Position
Distance (km)

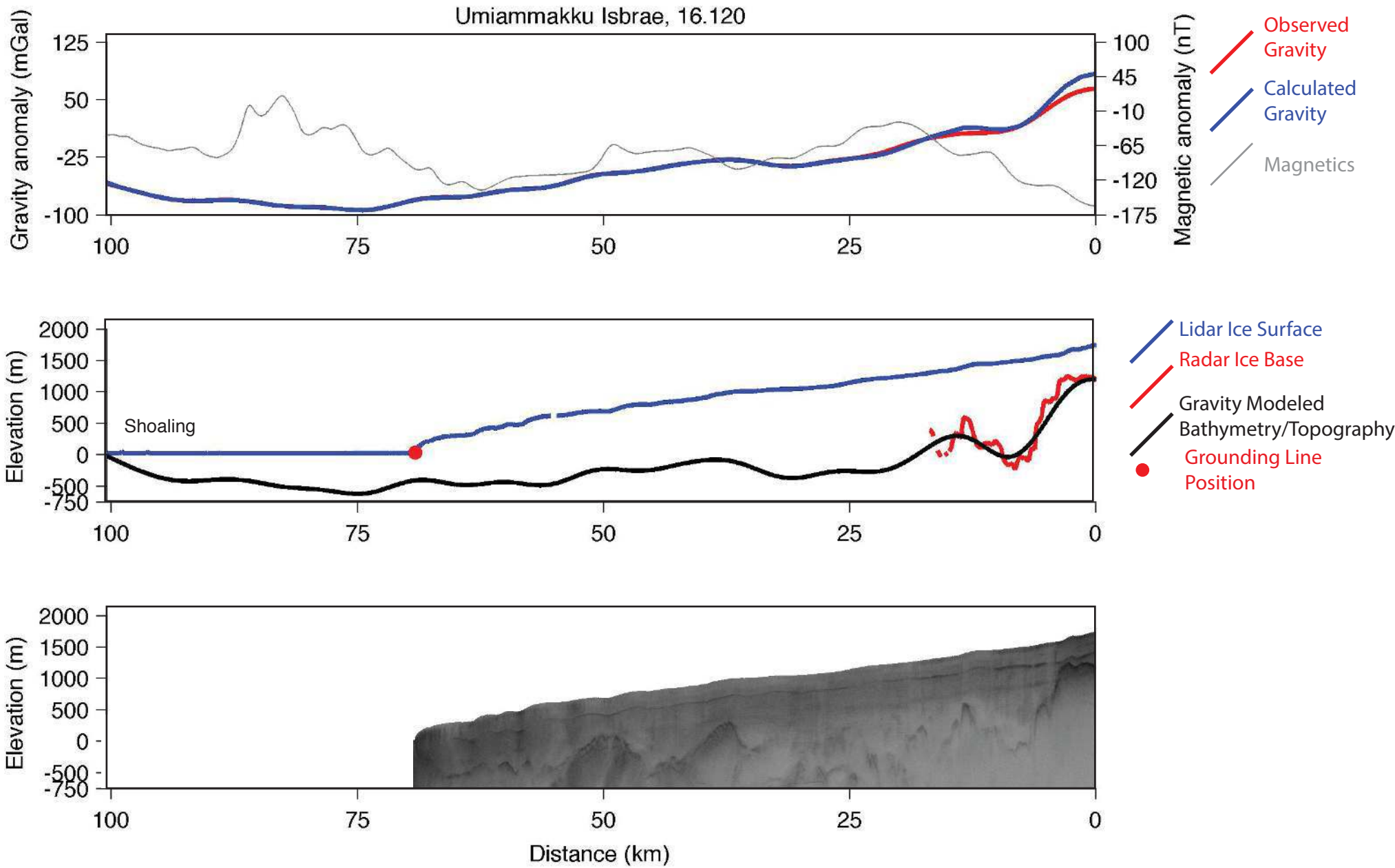
Umiammakku Isbrae, 16.120
Gravity anomaly (mGal)
125
50
-25
-100
Magnetic anomaly (nT)
100
45
-10
-65
-120
-175
100
75
50
25
0
Observed Gravity
Calculated Gravity
Magnetics
Elevation (m)
2000
1500
1000
500
0
-500
-750
Shoaling
Lidar Ice Surface
Radar Ice Base
Gravity Modeled Bathymetry/Topography
Grounding Line Position
Distance (km)

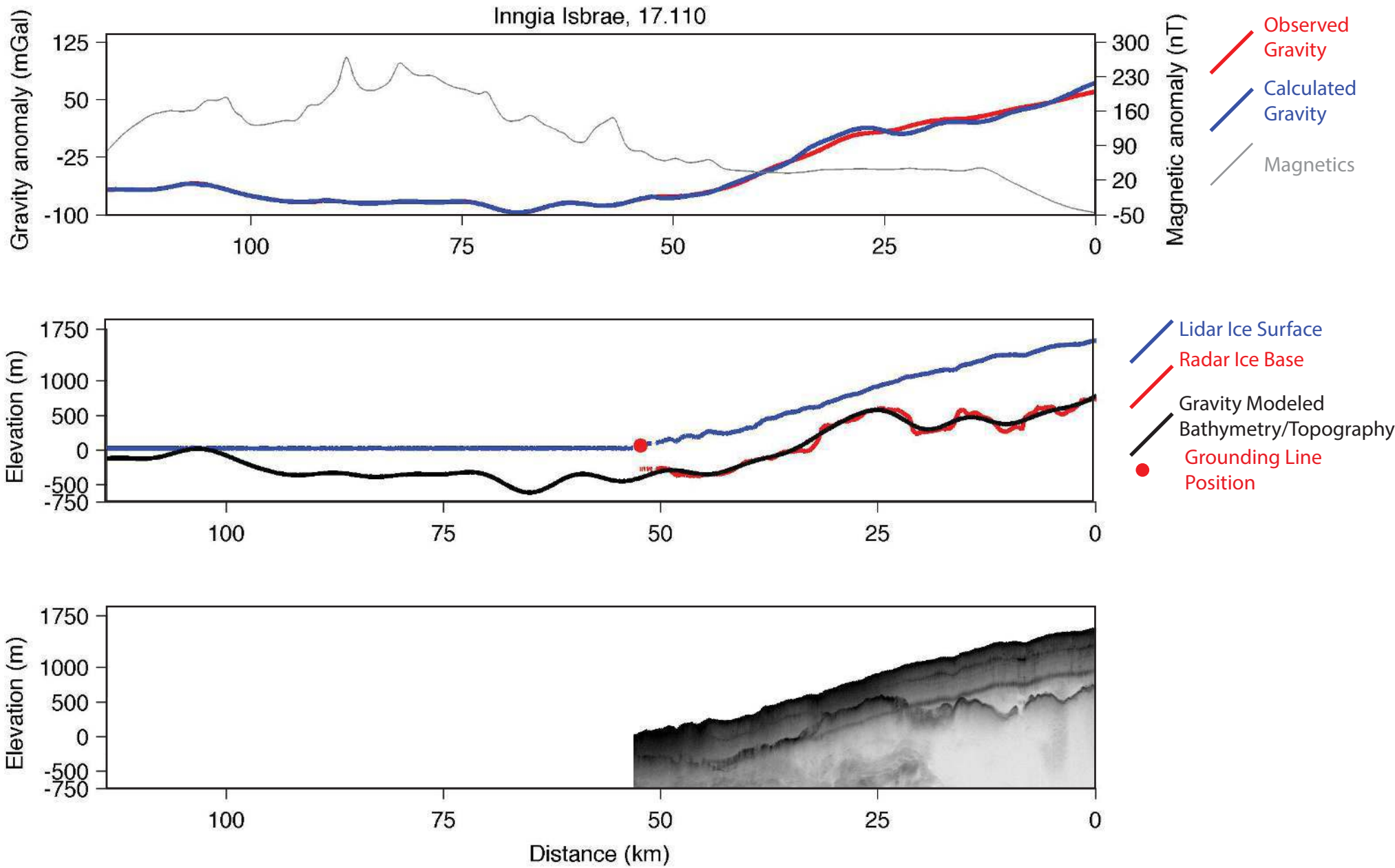
Inngia Isbrae, 17.110
Gravity anomaly (mGal)
125
50
-25
-100
Magnetic anomaly (nT)
300
230
160
90
20
-50
100
75
50
25
0
Observed Gravity
Calculated Gravity
Magnetics
Elevation (m)
1750
1000
500
0
-500
-750
Lidar Ice Surface
Radar Ice Base
Gravity Modeled Bathymetry/Topography
Grounding Line Position
Distance (km)

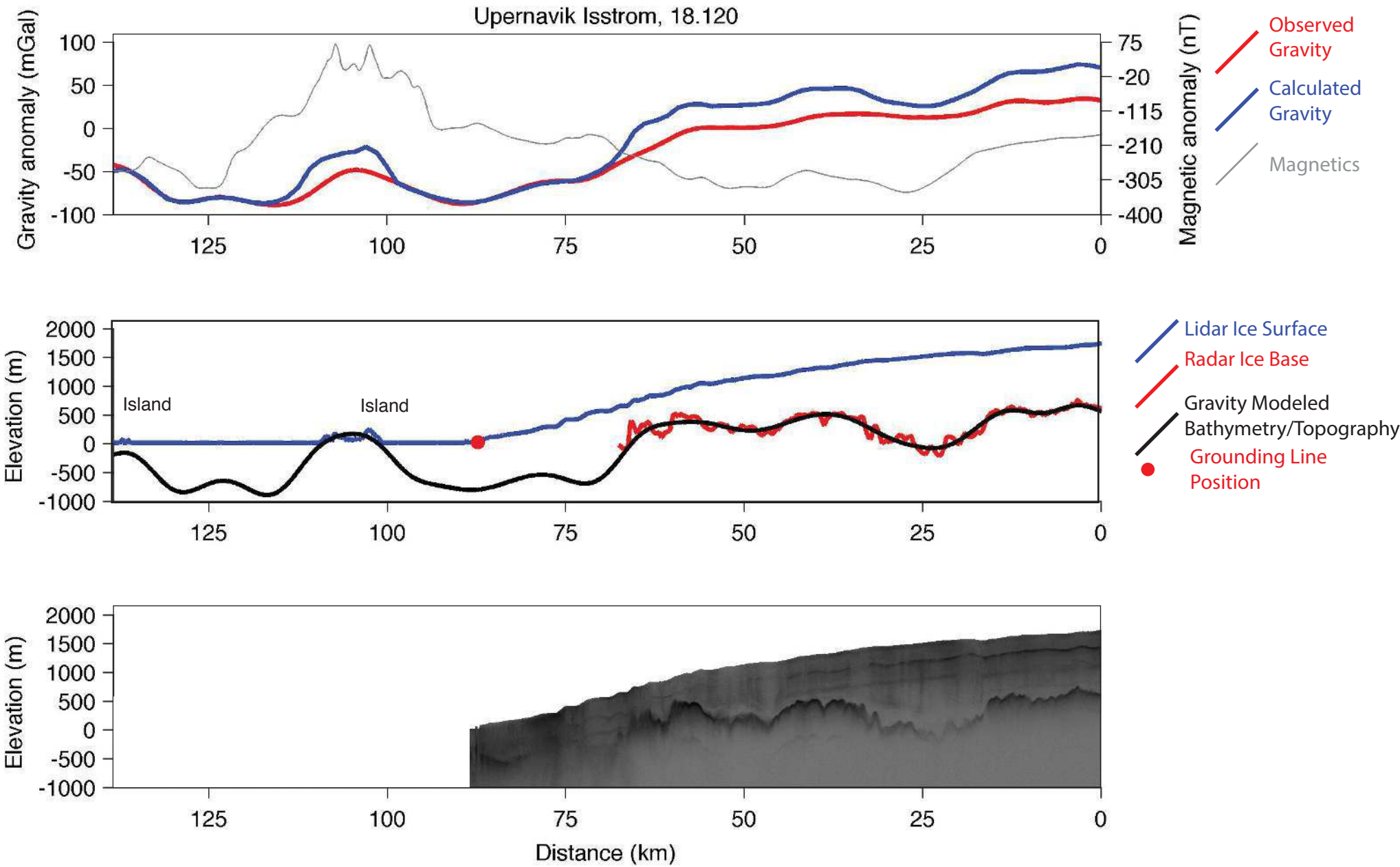
Upernavik Isstrom, 18.120
Gravity anomaly (mGal)
100
50
0
-50
-100
Magnetic anomaly (nT)
75
-20
-115
-210
-305
-400
125
100
75
50
25
0
Observed Gravity
Calculated Gravity
Magnetics
Elevation (m)
2000
1500
1000
500
0
-500
-1000
Island
Island
Lidar Ice Surface
Radar Ice Base
Gravity Modeled Bathymetry/Topography
Grounding Line Position
Distance (km)

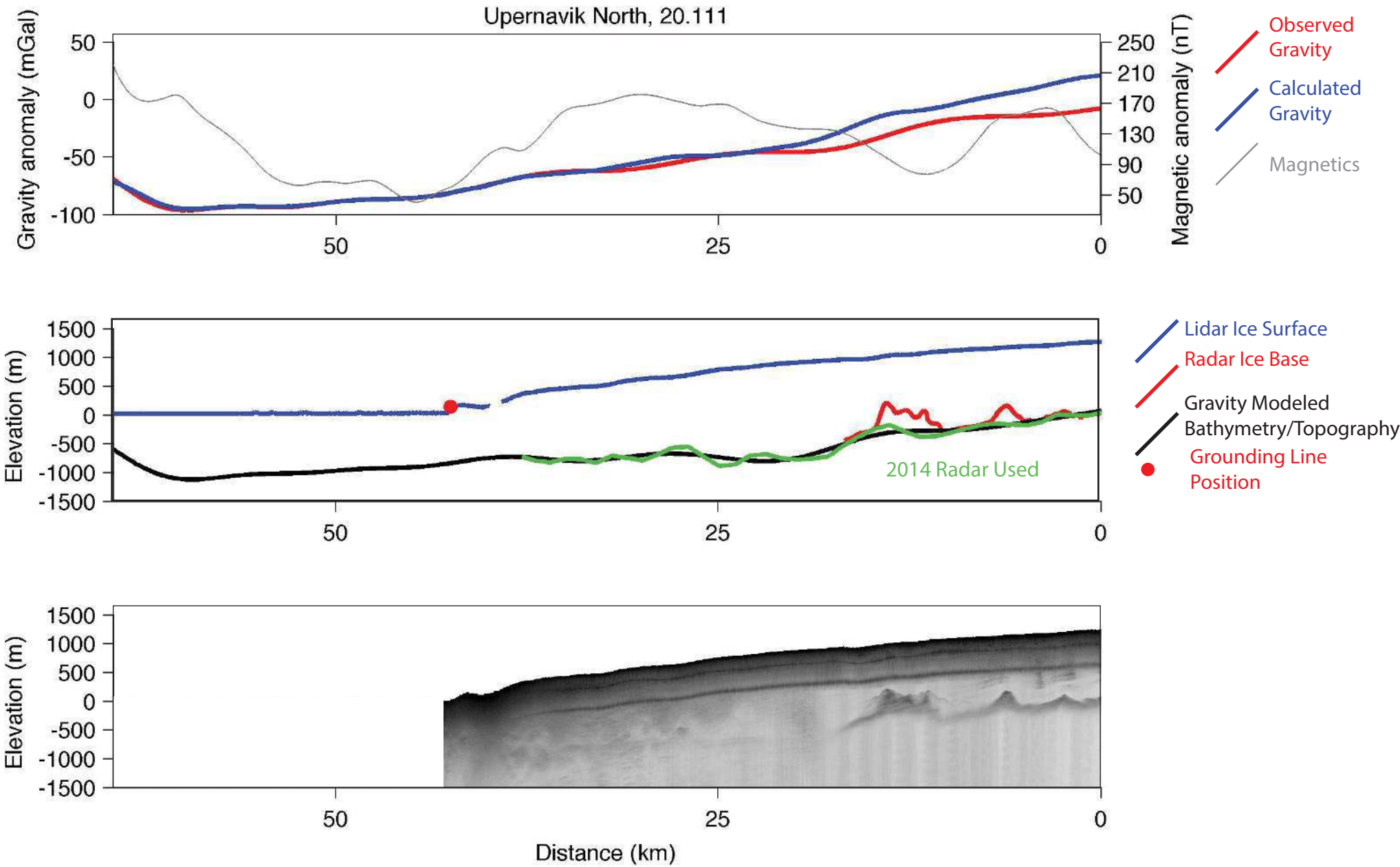
Upernavik North, 20.111
Gravity anomaly (mGal)
50
0
-50
-100
50
25
0
Magnetic anomaly (nT)
250
210
170
130
90
50
Observed Gravity
Calculated Gravity
Magnetics
Elevation (m)
1500
1000
500
0
-500
-1000
-1500
2014 Radar Used
Lidar Ice Surface
Radar Ice Base
Gravity Modeled Bathymetry/Topography
Grounding Line Position
Distance (km)

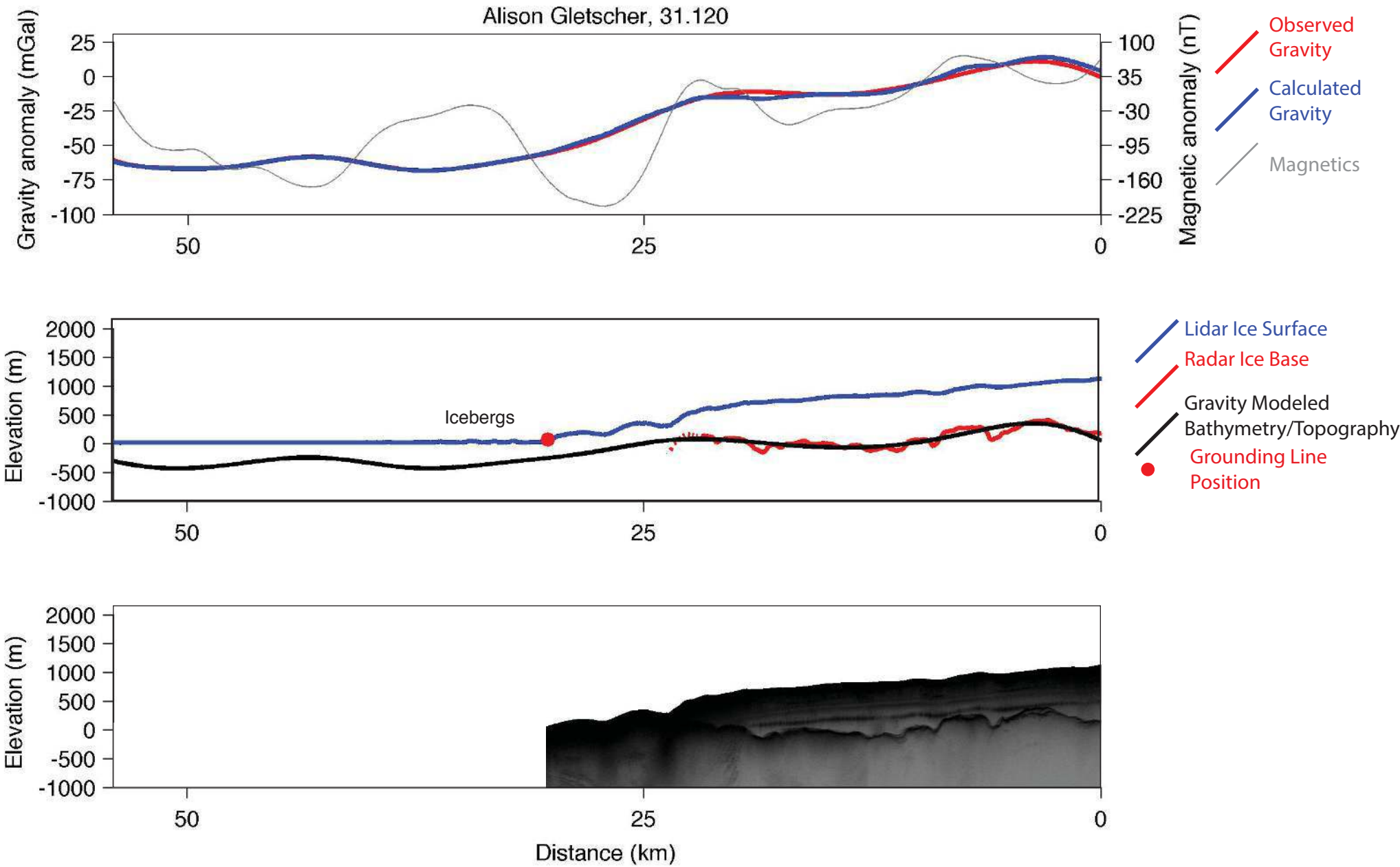
Alison Gletscher, 31.120
Gravity anomaly (mGal)
25
0
-25
-50
-75
-100
Magnetic anomaly (nT)
100
35
-30
-95
-160
-225
50
25
0
Observed Gravity
Calculated Gravity
Magnetics
Elevation (m)
2000
1500
1000
500
0
-500
-1000
Icebergs
Lidar Ice Surface
Radar Ice Base
Gravity Modeled Bathymetry/Topography
Grounding Line Position
Distance (km)

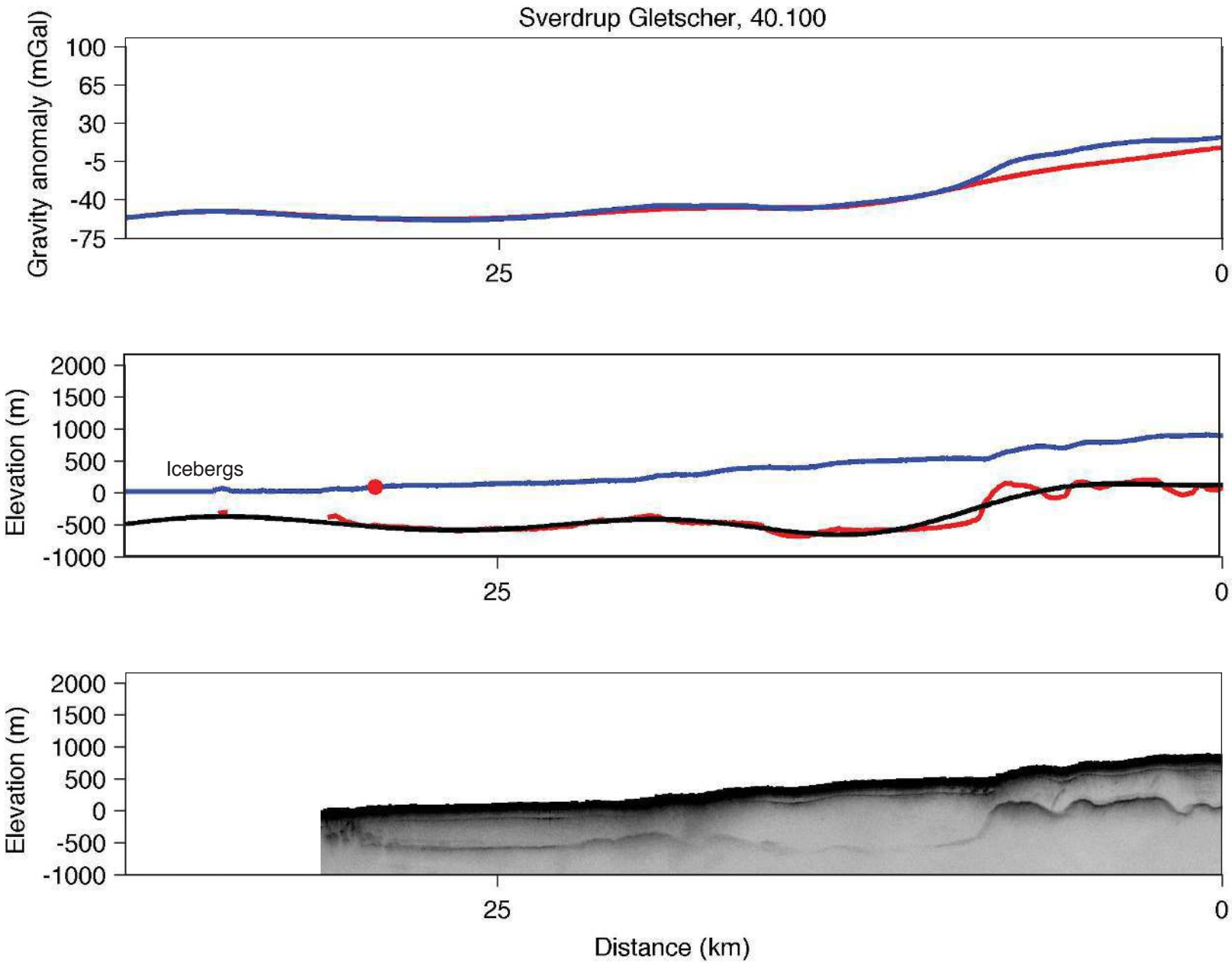
Sverdrup Gletscher, 40.100
Gravity anomaly (mGal)
100
65
30
-5
-40
-75
25
0
Observed Gravity
Calculated Gravity
Magnetics
Elevation (m)
2000
1500
1000
500
0
-500
-1000
Icebergs
25
0
Lidar Ice Surface
Radar Ice Base
Gravity Modeled Bathymetry/Topography
Grounding Line Position
Elevation (m)
2000
1500
1000
500
0
-500
-1000
25
0
Distance (km)

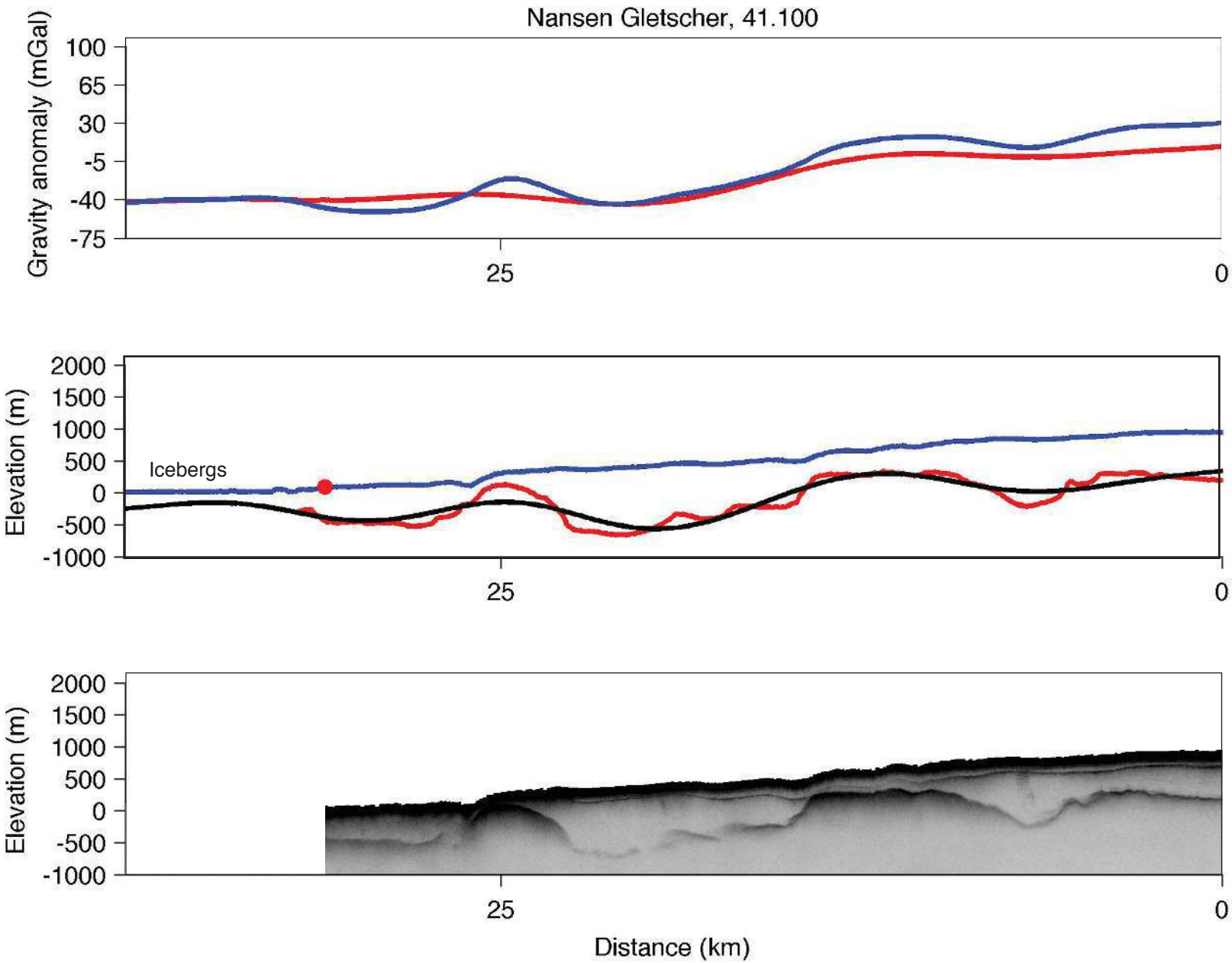
Nansen Gletscher, 41.100
Gravity anomaly (mGal)
100
65
30
-5
-40
-75
25
0
Observed Gravity
Calculated Gravity
Magnetics
Elevation (m)
2000
1500
1000
500
0
-500
-1000
Icebergs
25
0
Lidar Ice Surface
Radar Ice Base
Gravity Modeled Bathymetry/Topography
Grounding Line Position
Elevation (m)
2000
1500
1000
500
0
-500
-1000
25
0
Distance (km)

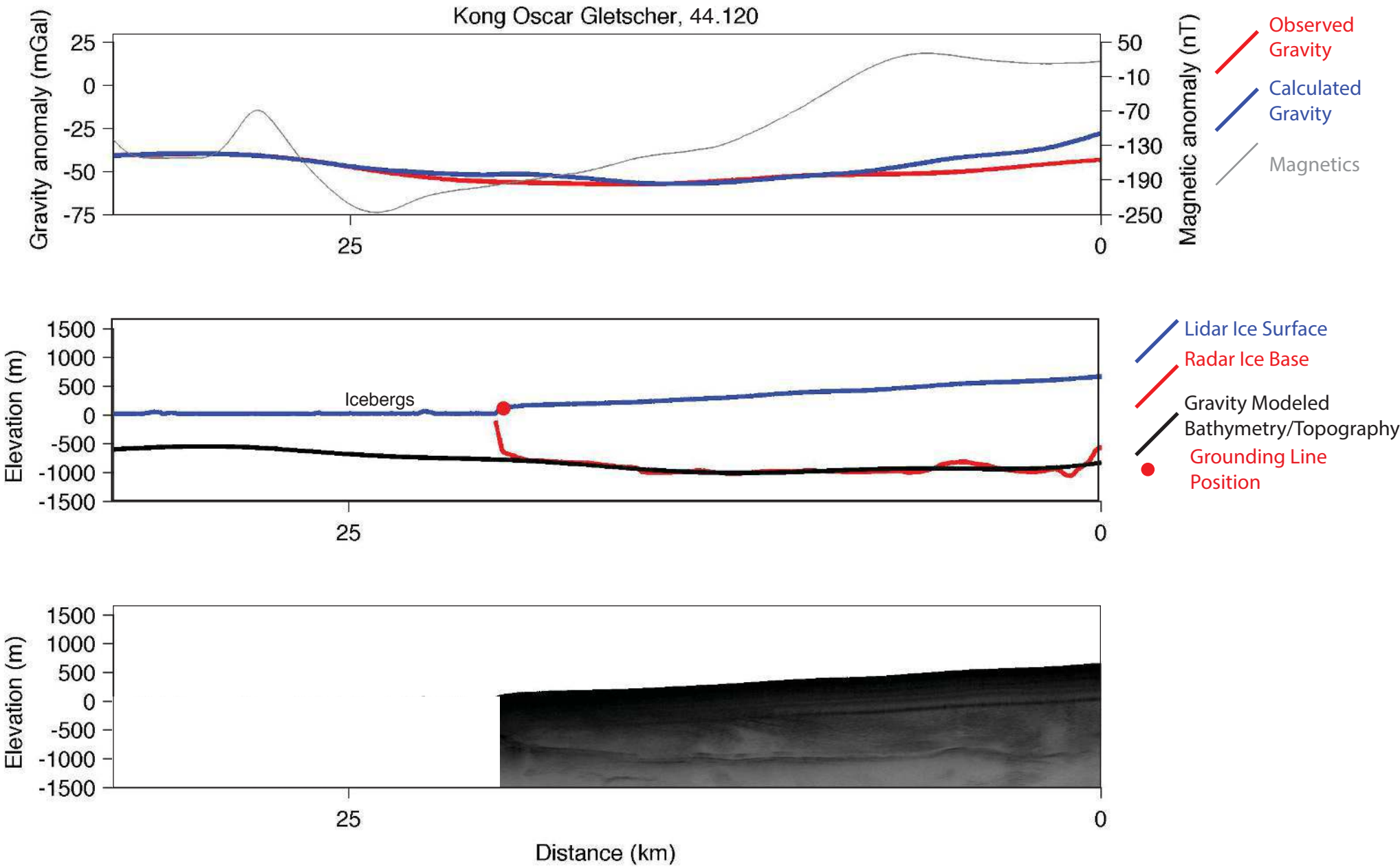
Kong Oscar Gletscher, 44.120
Gravity anomaly (mGal)
25
0
-25
-50
-75
25
0
Magnetic anomaly (nT)
50
-10
-70
-130
-190
-250
Observed Gravity
Calculated Gravity
Magnetics
Elevation (m)
1500
1000
500
0
-500
-1000
-1500
Icebergs
25
0
Lidar Ice Surface
Radar Ice Base
Gravity Modeled Bathymetry/Topography
Grounding Line Position
Elevation (m)
1500
1000
500
0
-500
-1000
-1500
25
0
Distance (km)

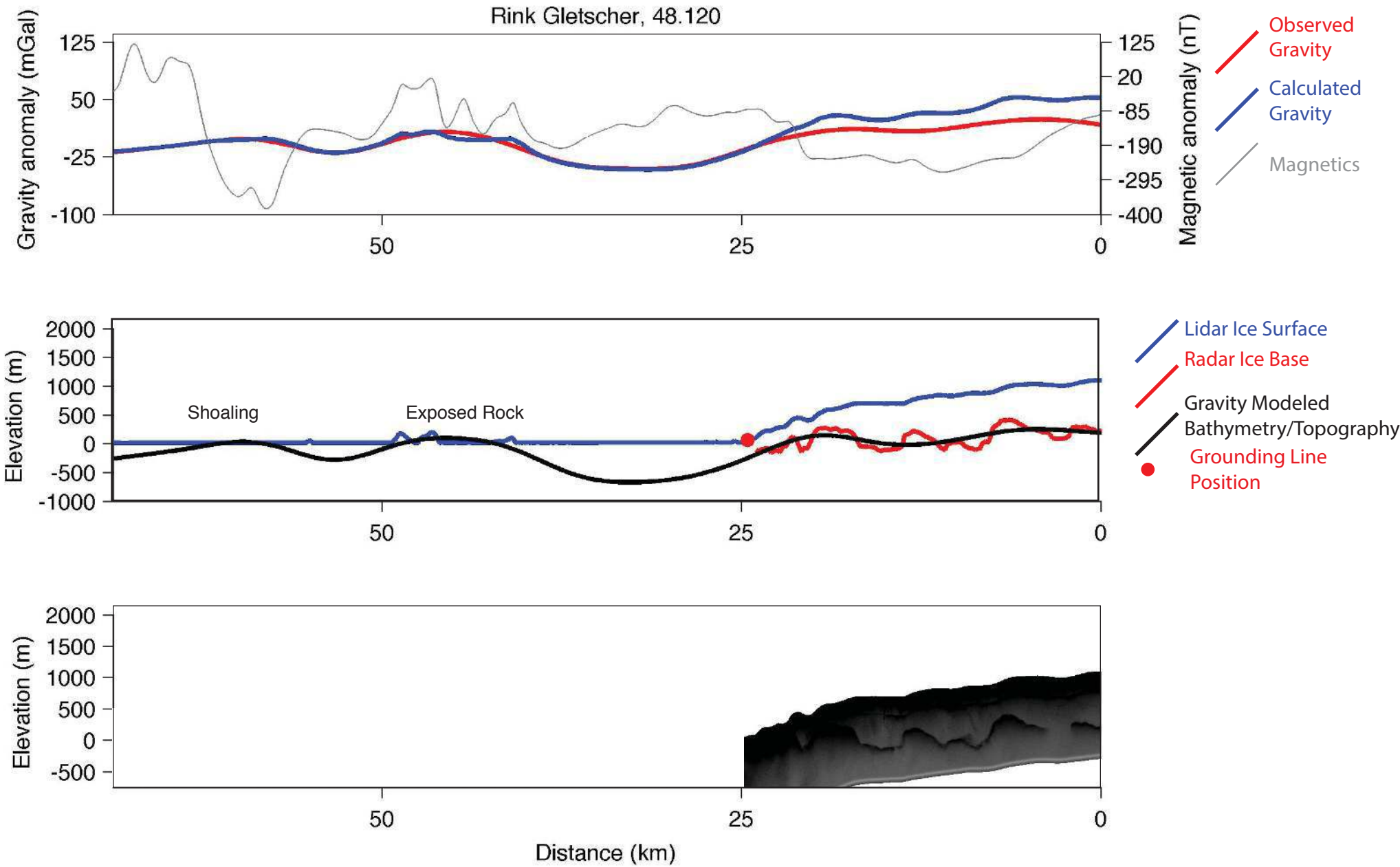
Rink Gletscher, 48.120
Gravity anomaly (mGal)
125
50
-25
-100
Magnetic anomaly (nT)
125
20
-85
-190
-295
-400
50
25
0
Observed Gravity
Calculated Gravity
Magnetics
Elevation (m)
2000
1500
1000
500
0
-500
-1000
Shoaling
Exposed Rock
Lidar Ice Surface
Radar Ice Base
Gravity Modeled Bathymetry/Topography
Grounding Line Position
Distance (km)

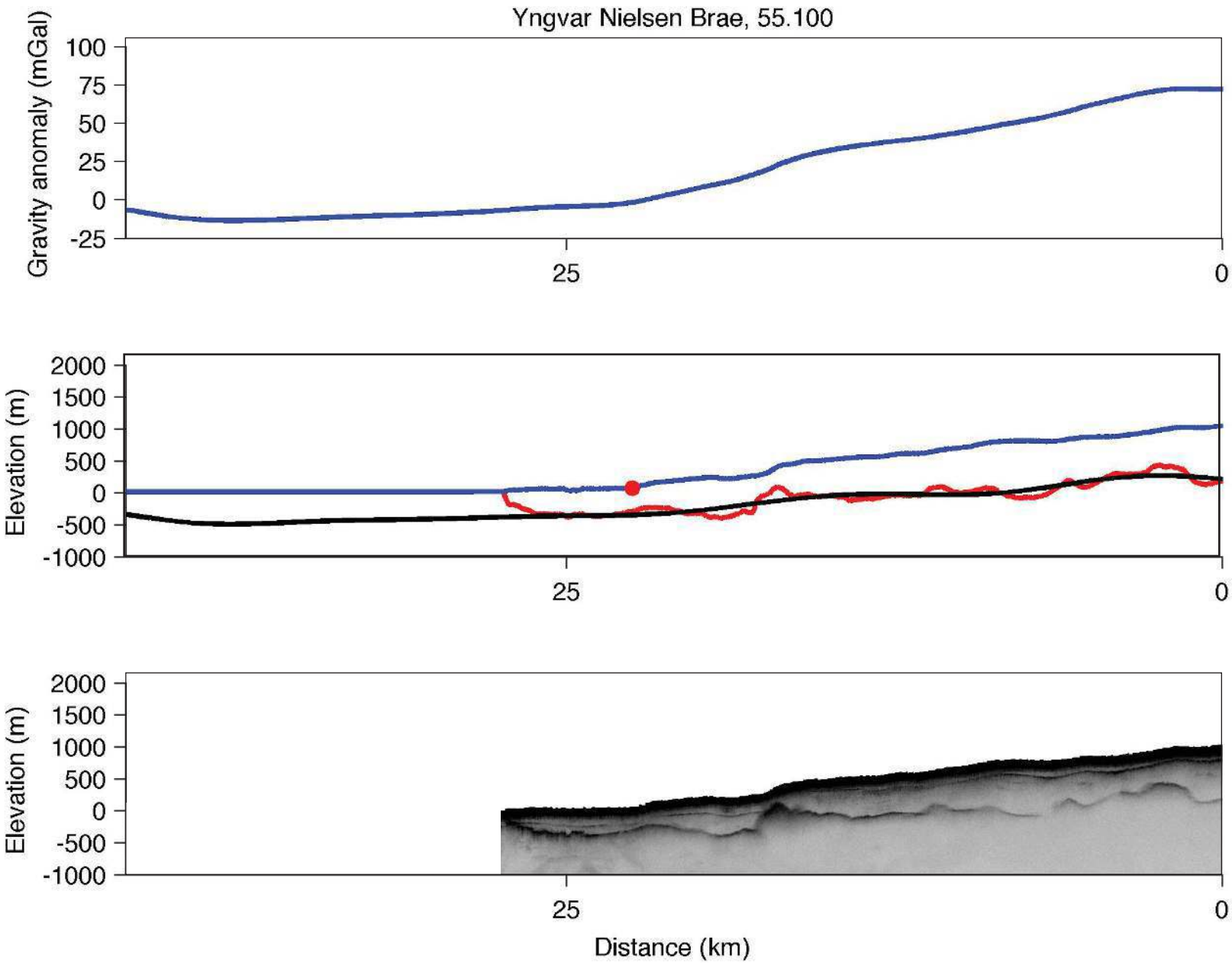
Yngvar Nielsen Brae, 55.100
Gravity anomaly (mGal)
100
75
50
25
0
-25
25
0
Observed Gravity
Calculated Gravity
Magnetics
Elevation (m)
2000
1500
1000
500
0
-500
-1000
25
0
Lidar Ice Surface
Radar Ice Base
Gravity Modeled Bathymetry/Topography
Grounding Line Position
Elevation (m)
2000
1500
1000
500
0
-500
-1000
25
0
Distance (km)

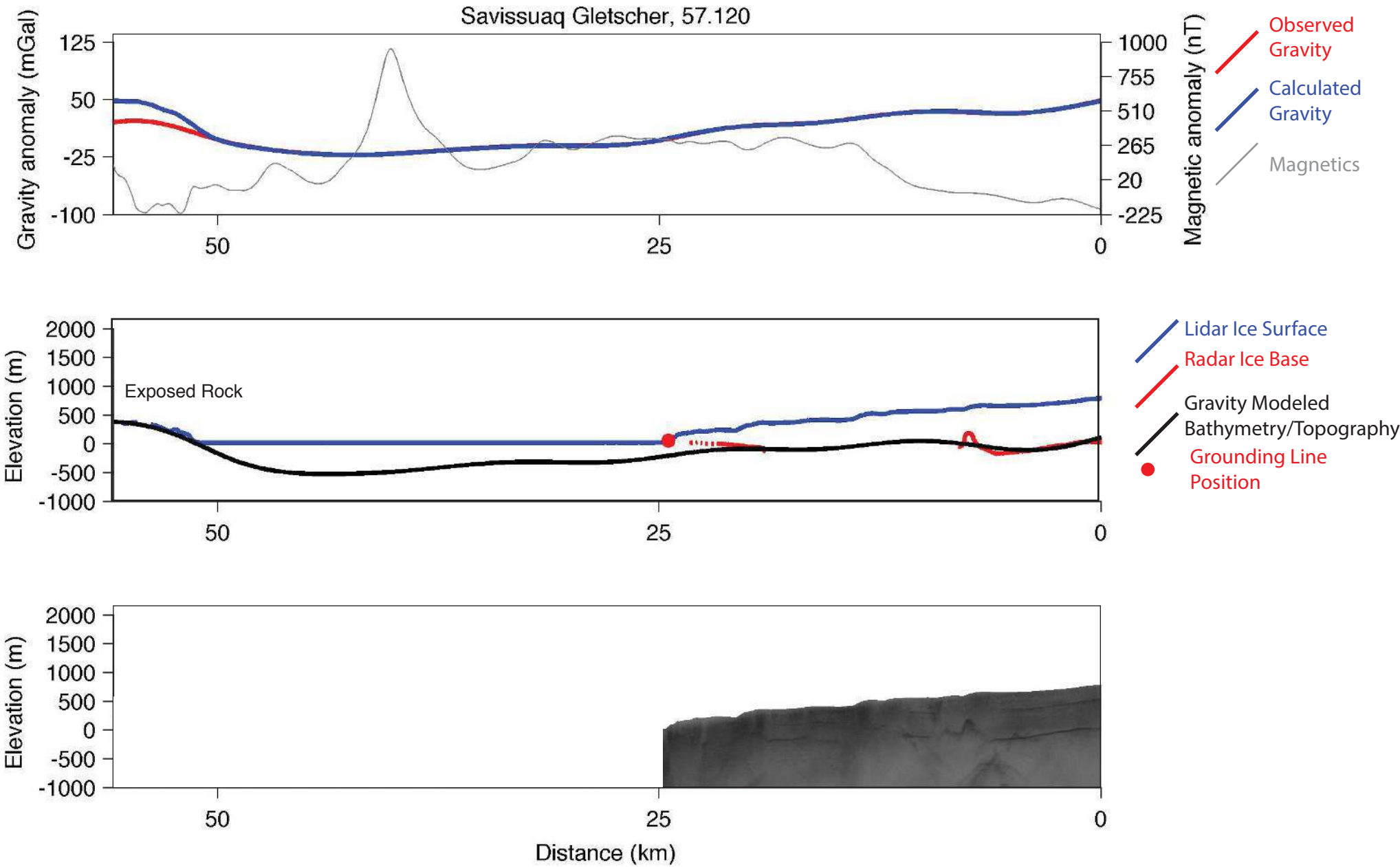
Savissuaq Gletscher, 57.120
Gravity anomaly (mGal)
125
50
-25
-100
1000
755
510
265
20
-225
Magnetic anomaly (nT)
50
25
0
Observed Gravity
Calculated Gravity
Magnetics
Elevation (m)
2000
1500
1000
500
0
-500
-1000
Exposed Rock
Lidar Ice Surface
Radar Ice Base
Gravity Modeled Bathymetry/Topography
Grounding Line Position
Distance (km)

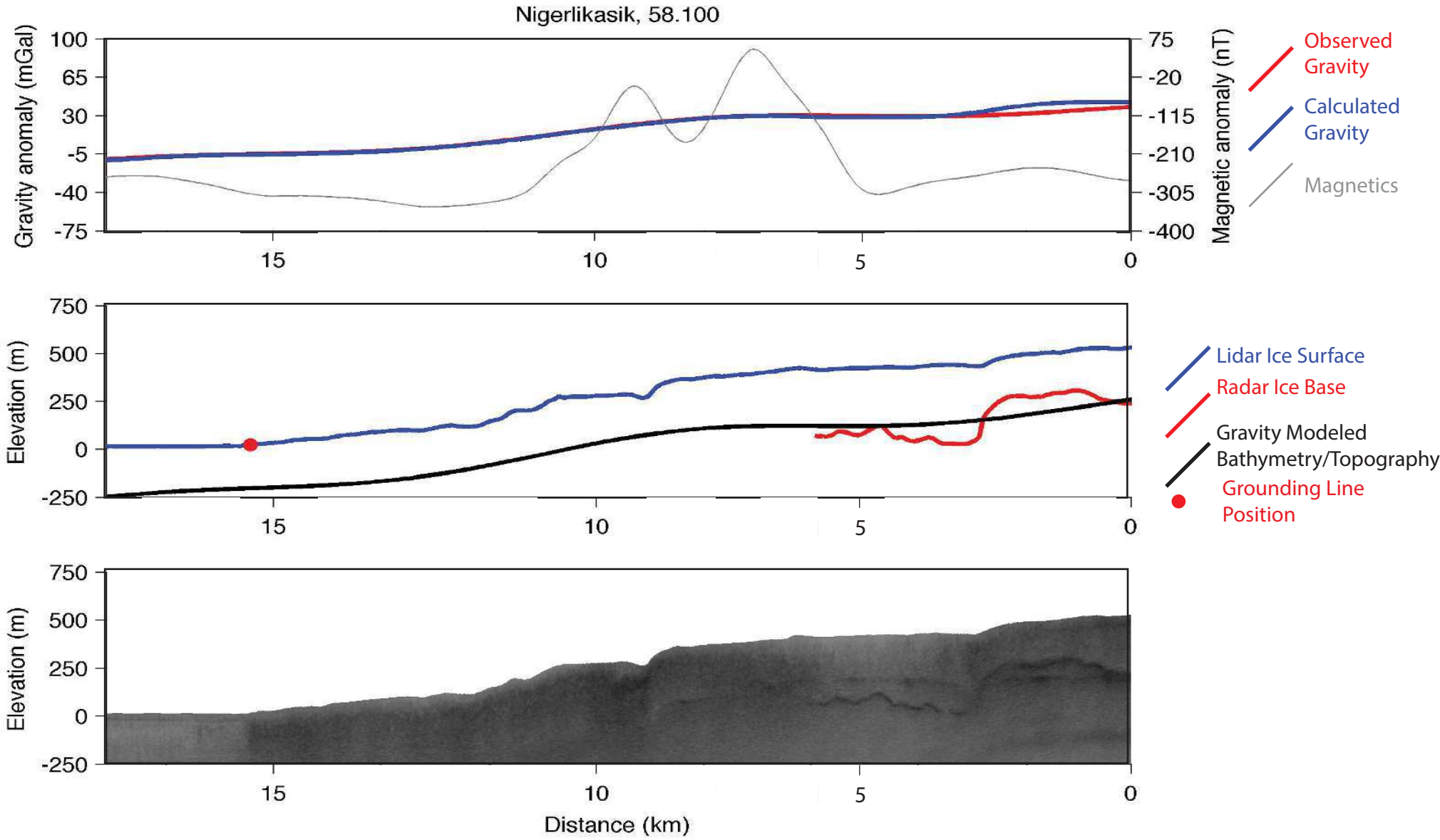
Nigerlikasik, 58.100
Gravity anomaly (mGal)
100
65
30
-5
-40
-75
Magnetic anomaly (nT)
75
-20
-115
-210
-305
-400
15
10
5
0
Observed Gravity
Calculated Gravity
Magnetics
Elevation (m)
750
500
250
0
-250
Lidar Ice Surface
Radar Ice Base
Gravity Modeled Bathymetry/Topography
Grounding Line Position
Distance (km)

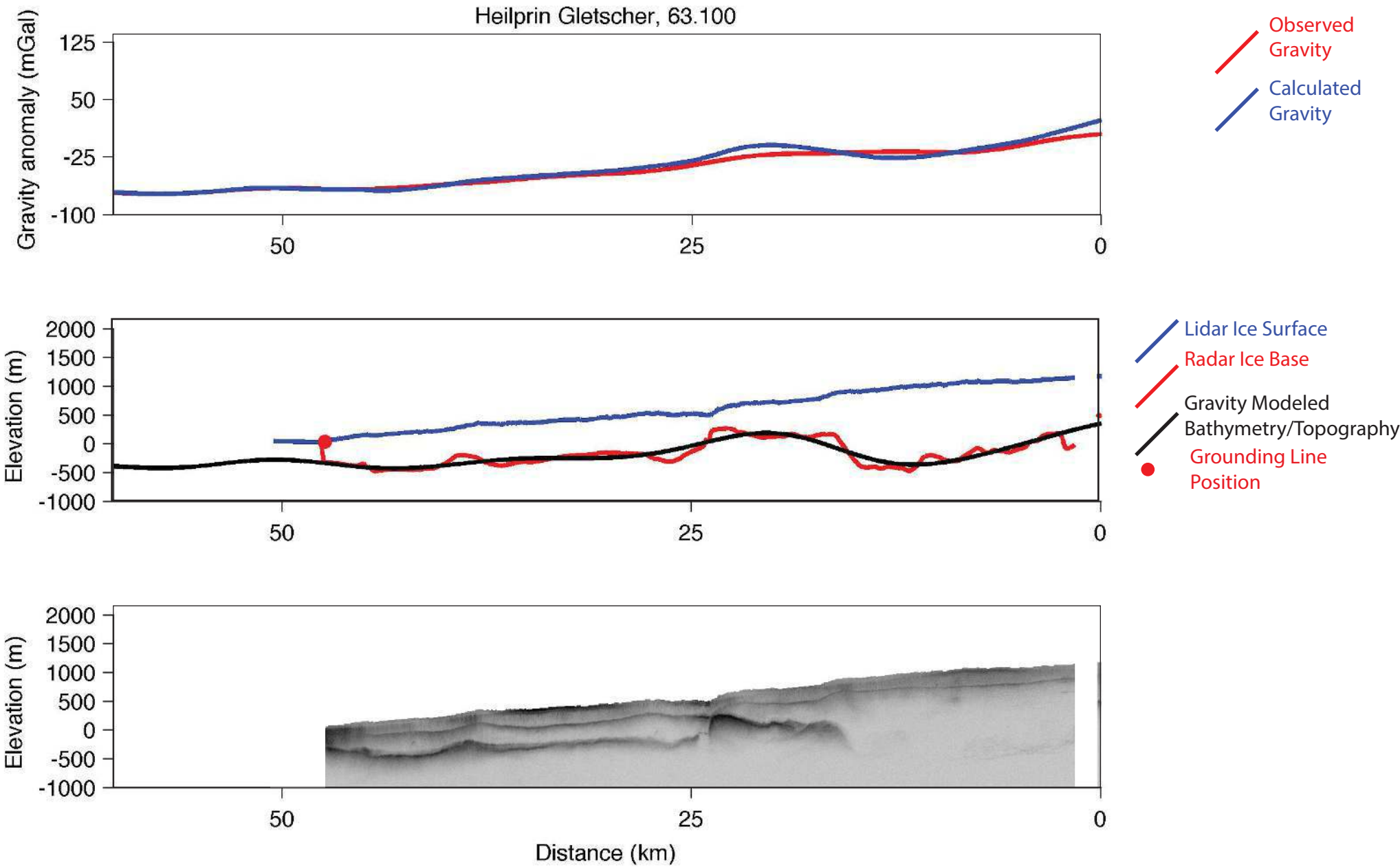
Heilprin Gletscher, 63.100
Gravity anomaly (mGal)
125
50
-25
-100
50
25
0
Observed Gravity
Calculated Gravity
Elevation (m)
2000
1500
1000
500
0
-500
-1000
50
25
0
Lidar Ice Surface
Radar Ice Base
Gravity Modeled Bathymetry/Topography
Grounding Line Position
Elevation (m)
2000
1500
1000
500
0
-500
-1000
50
25
0
Distance (km)

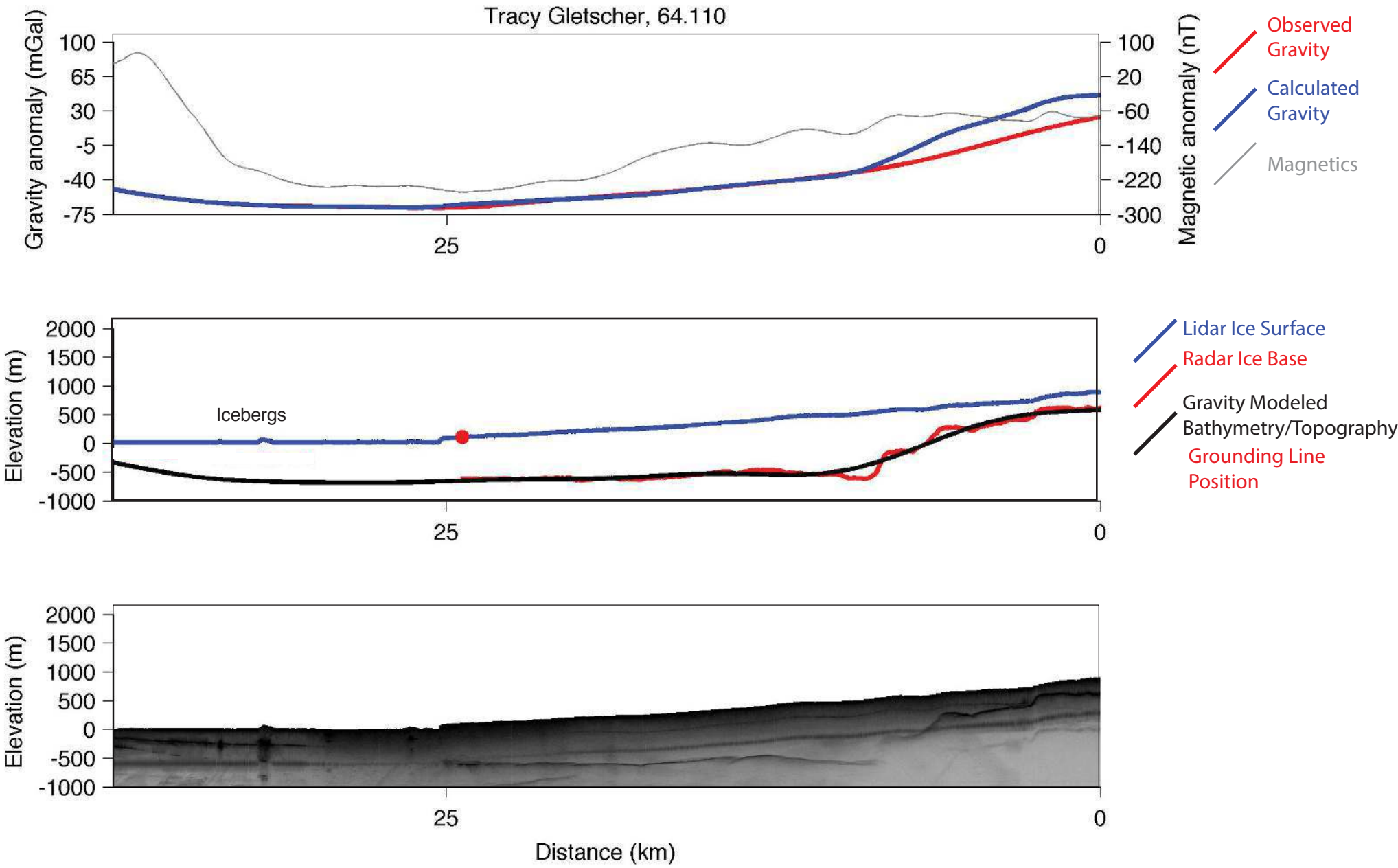
Tracy Gletscher, 64.110
Gravity anomaly (mGal)
100
65
30
-5
-40
-75
25
0
Magnetic anomaly (nT)
100
20
-60
-140
-220
-300
Observed Gravity
Calculated Gravity
Magnetics
Elevation (m)
2000
1500
1000
500
0
-500
-1000
Icebergs
Lidar Ice Surface
Radar Ice Base
Gravity Modeled Bathymetry/Topography
Grounding Line Position
Distance (km)

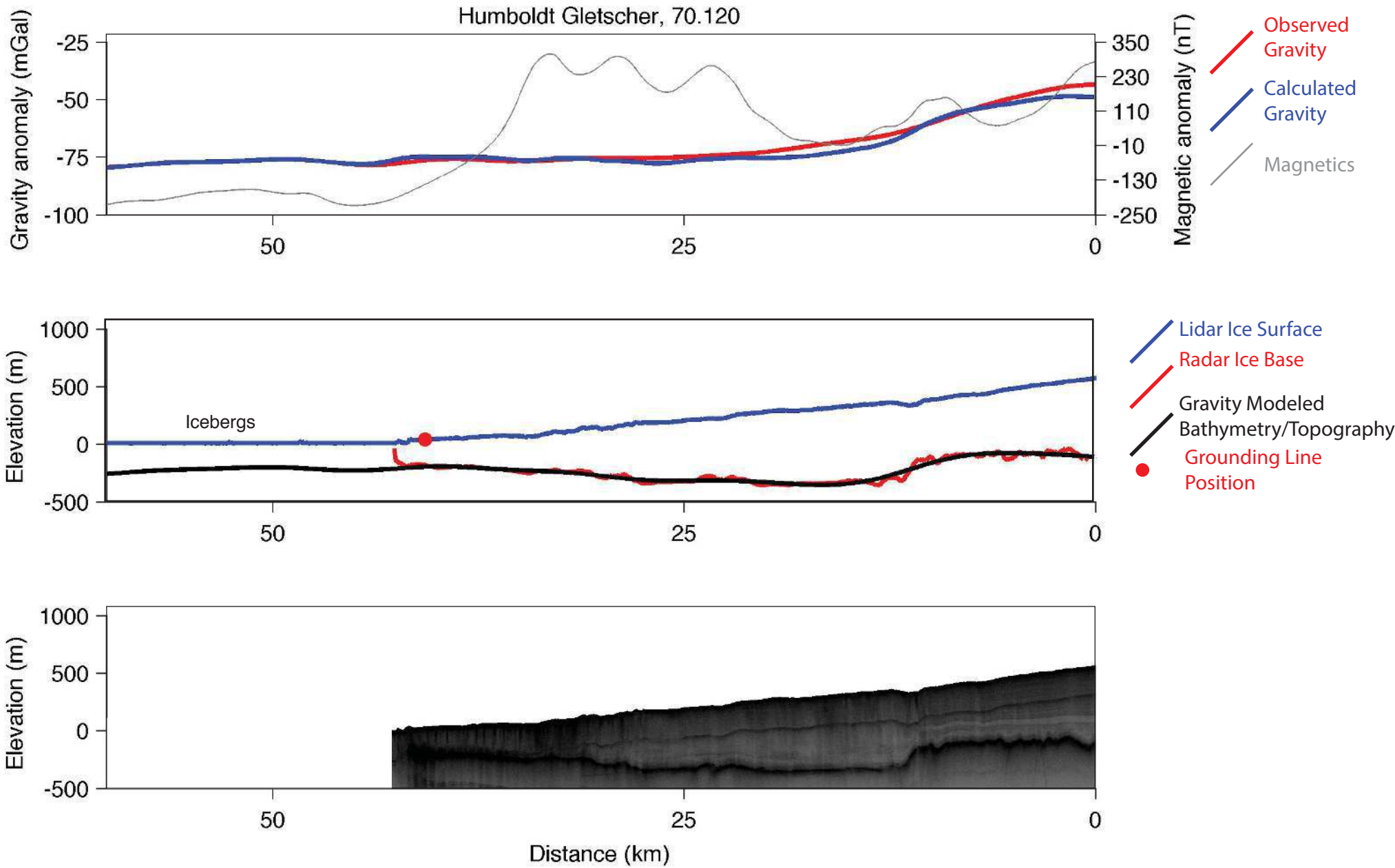
Humboldt Gletscher, 70.120
Gravity anomaly (mGal)
-25
-50
-75
-100
Magnetic anomaly (nT)
350
230
110
-10
-130
-250
50
25
0
Observed Gravity
Calculated Gravity
Magnetics
Elevation (m)
1000
500
0
-500
Icebergs
Lidar Ice Surface
Radar Ice Base
Gravity Modeled Bathymetry/Topography
Grounding Line Position
Distance (km)

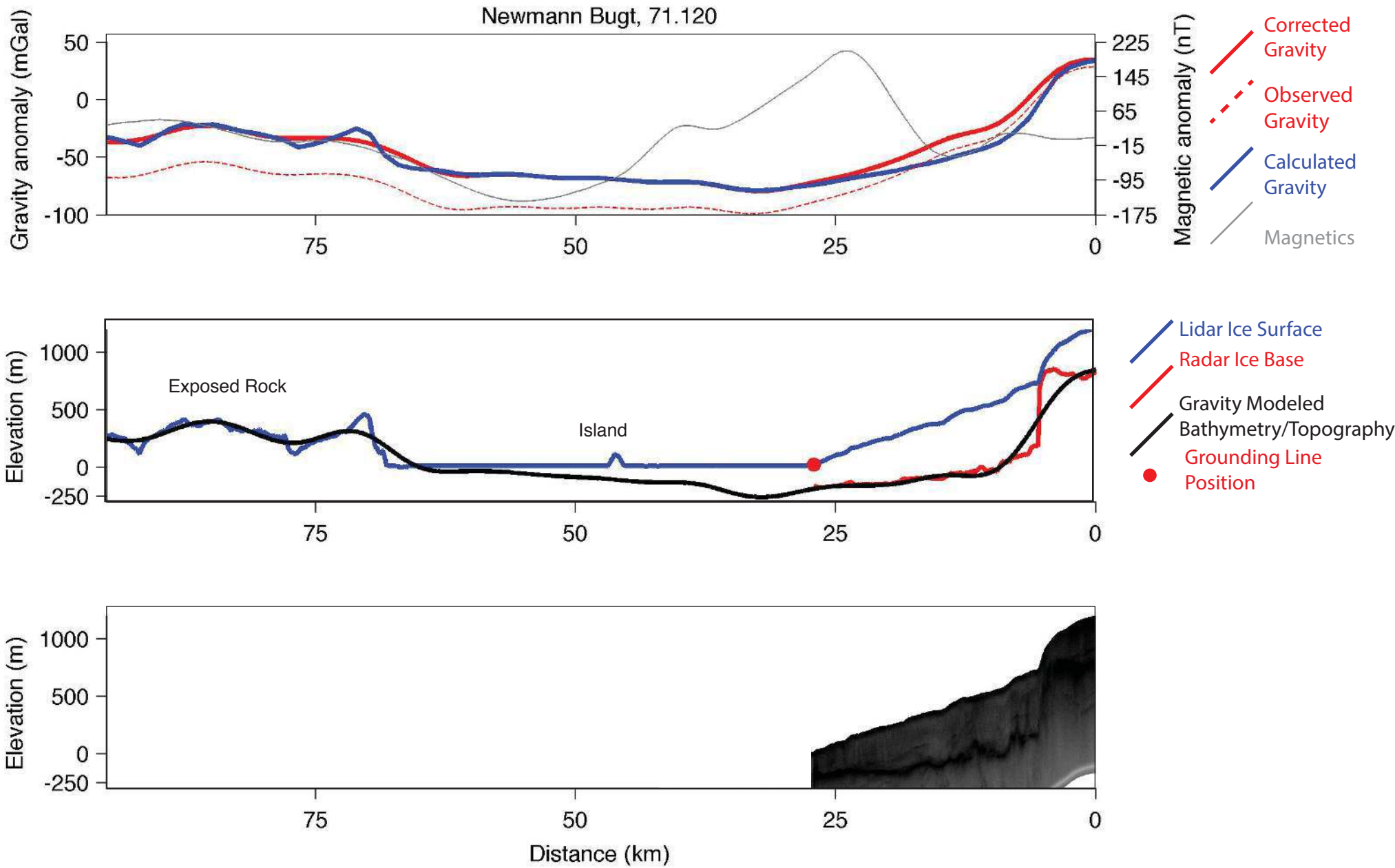
Newmann Bugt, 71.120
Gravity anomaly (mGal)
50
0
-50
-100
225
145
65
-15
-95
-175
Magnetic anomaly (nT)
75
50
25
0
Corrected Gravity
Observed Gravity
Calculated Gravity
Magnetics
Elevation (m)
1000
500
0
-250
Exposed Rock
Island
Lidar Ice Surface
Radar Ice Base
Gravity Modeled Bathymetry/Topography
Grounding Line Position
Distance (km)

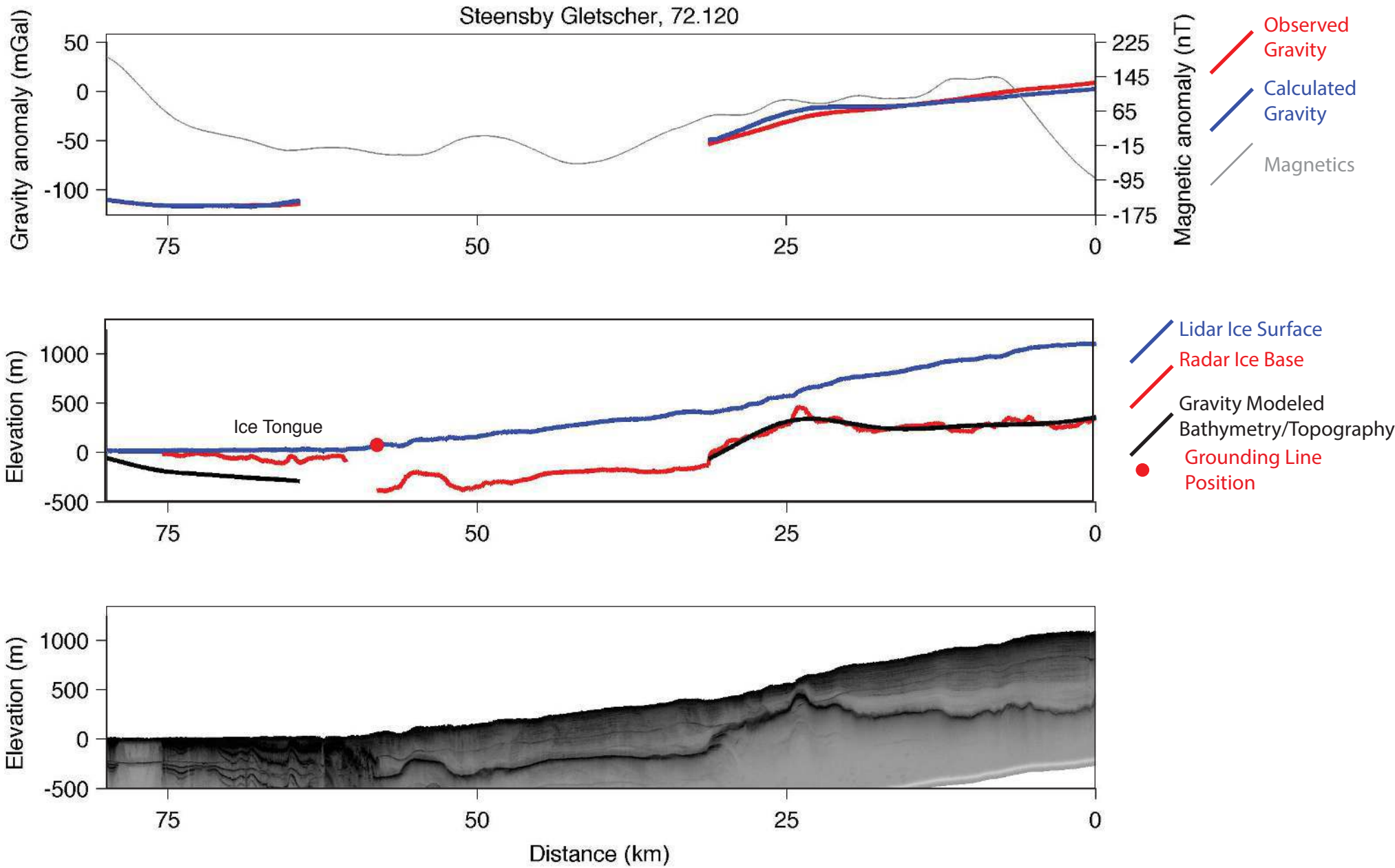
Steensby Gletscher, 72.120
Gravity anomaly (mGal)
50
0
-50
-100
Magnetic anomaly (nT)
225
145
65
-15
-95
-175
75
50
25
0
Observed Gravity
Calculated Gravity
Magnetics
Elevation (m)
1000
500
0
-500
Ice Tongue
Lidar Ice Surface
Radar Ice Base
Gravity Modeled Bathymetry/Topography
Grounding Line Position
Distance (km)

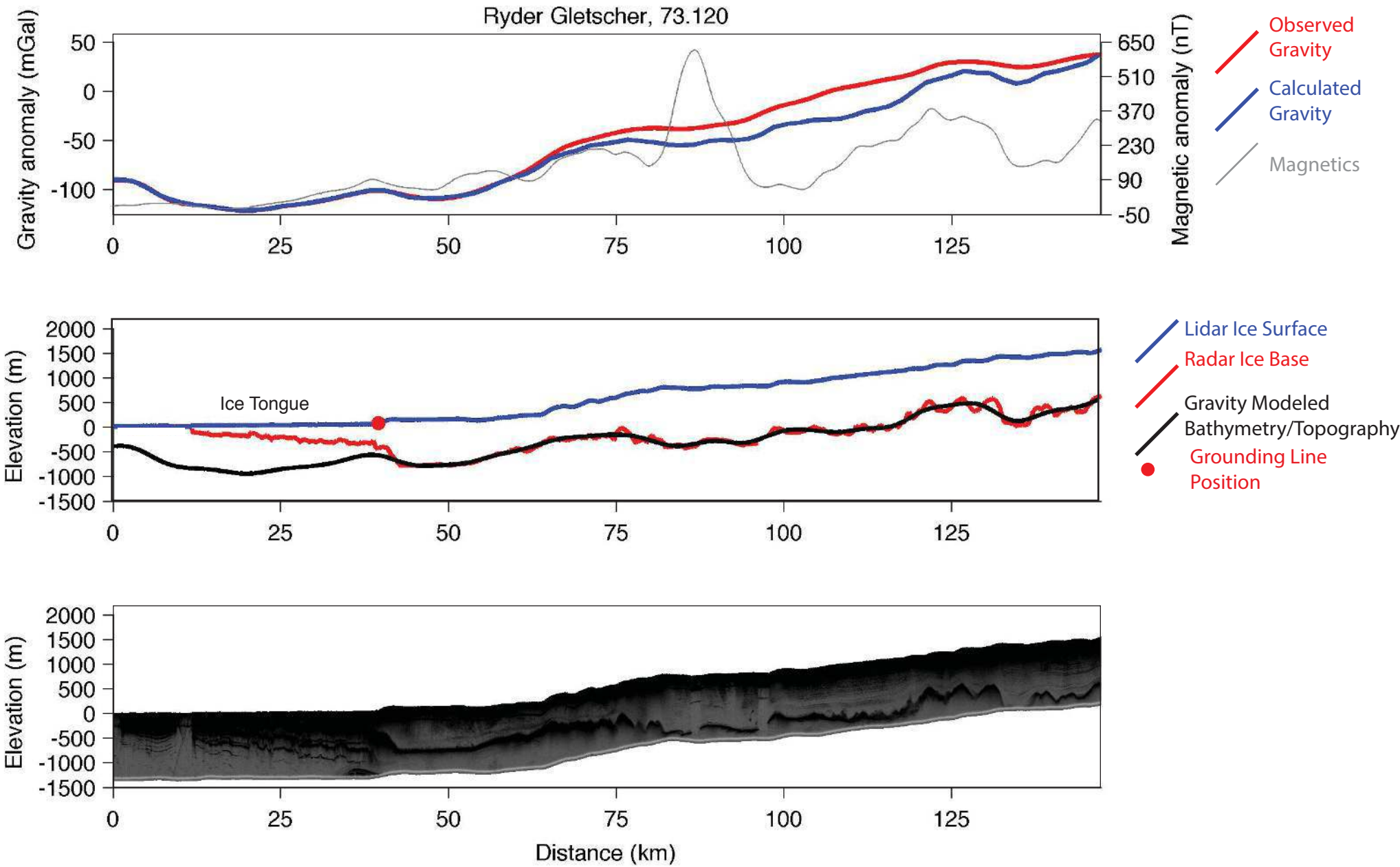
Ryder Gletscher, 73.120
Gravity anomaly (mGal)
50
0
-50
-100
Magnetic anomaly (nT)
650
510
370
230
90
-50
0
25
50
75
100
125
Observed Gravity
Calculated Gravity
Magnetics
Elevation (m)
2000
1500
1000
500
0
-500
-1000
-1500
Ice Tongue
Lidar Ice Surface
Radar Ice Base
Gravity Modeled Bathymetry/Topography
Grounding Line Position
Distance (km)

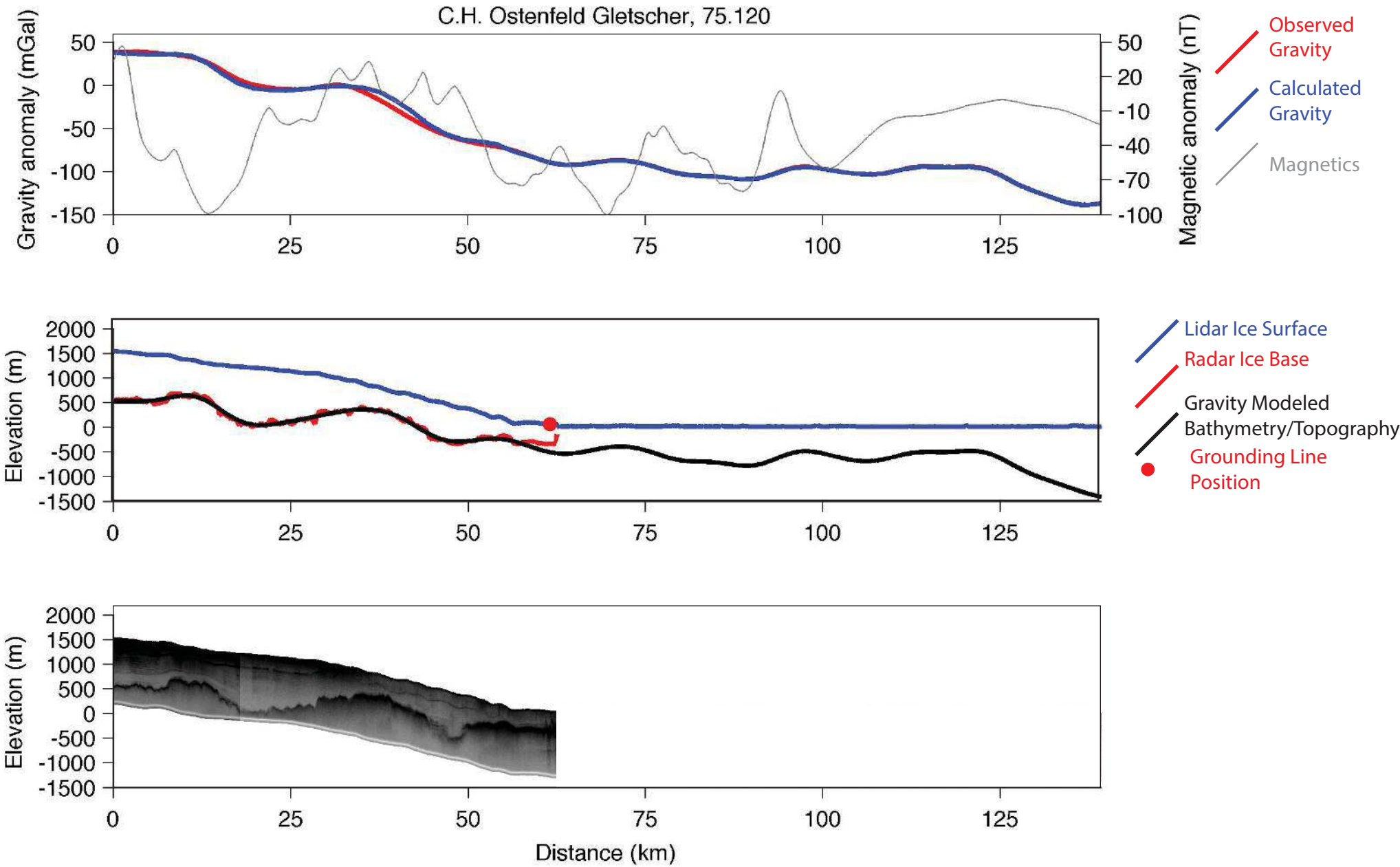
C.H. Ostenfeld Gletscher, 75.120
Gravity anomaly (mGal)
Magnetic anomaly (nT)
Observed Gravity
Calculated Gravity
Magnetics
Elevation (m)
Lidar Ice Surface
Radar Ice Base
Gravity Modeled Bathymetry/Topography
Grounding Line Position
Distance (km)

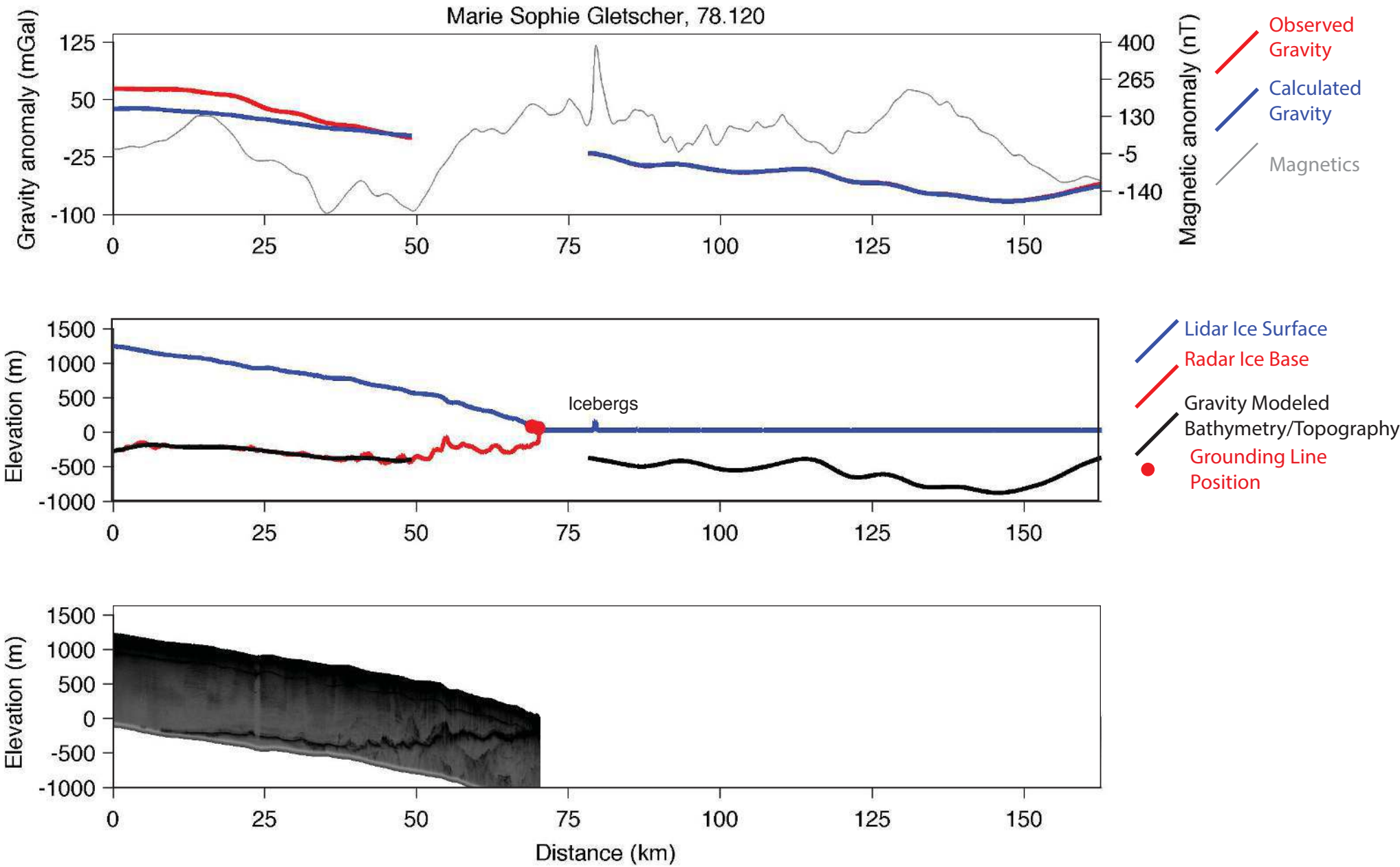
Marie Sophie Gletscher, 78.120
Gravity anomaly (mGal)
125
50
-25
-100
Magnetic anomaly (nT)
400
265
130
-5
-140
0
25
50
75
100
125
150
Observed Gravity
Calculated Gravity
Magnetics
Elevation (m)
1500
1000
500
0
-500
-1000
Icebergs
Lidar Ice Surface
Radar Ice Base
Gravity Modeled Bathymetry/Topography
Grounding Line Position
Distance (km)

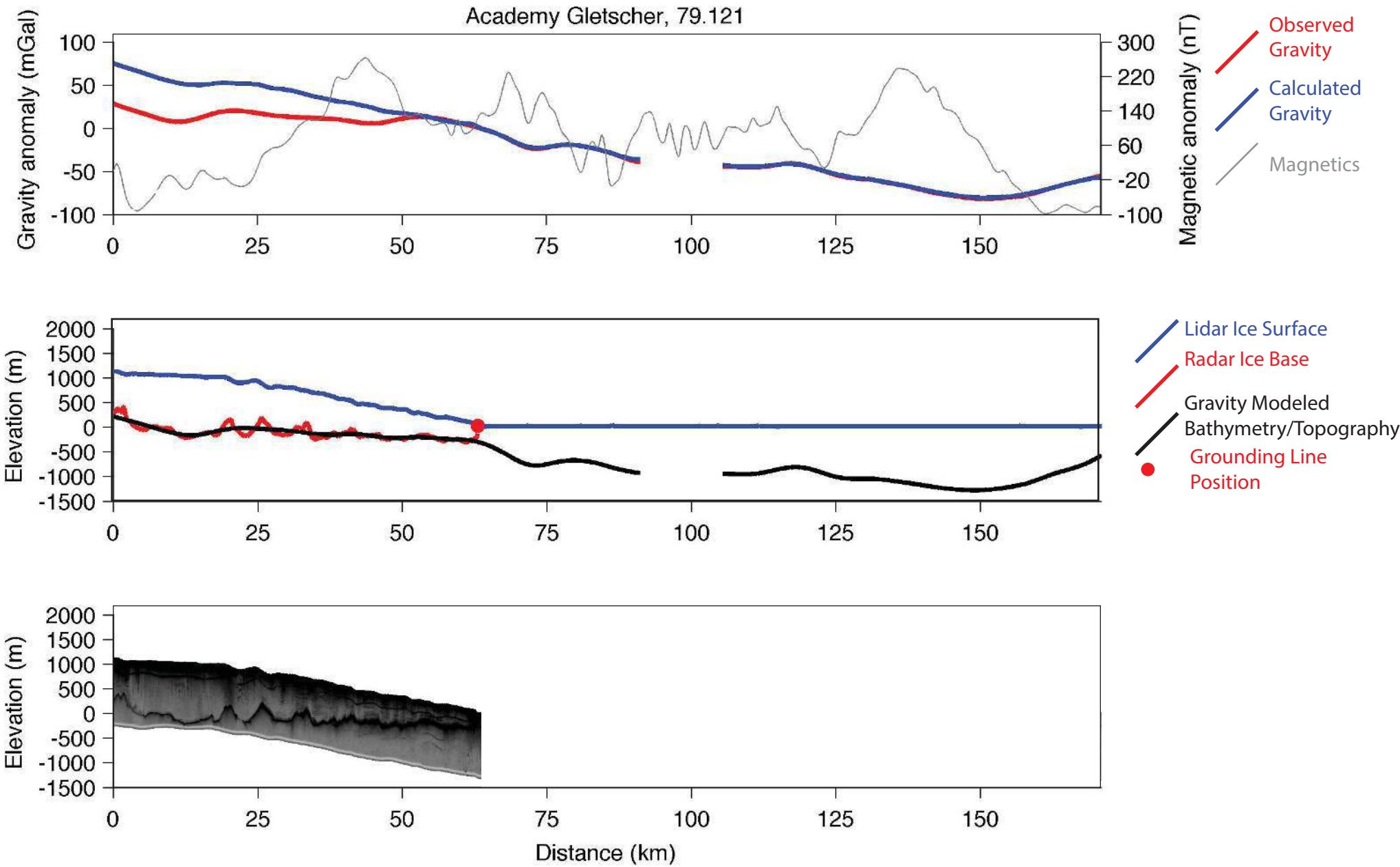
Academy Gletscher, 79.121
Gravity anomaly (mGal)
Magnetic anomaly (nT)
Observed Gravity
Calculated Gravity
Magnetics
Elevation (m)
Lidar Ice Surface
Radar Ice Base
Gravity Modeled Bathymetry/Topography
Grounding Line Position
Distance (km)

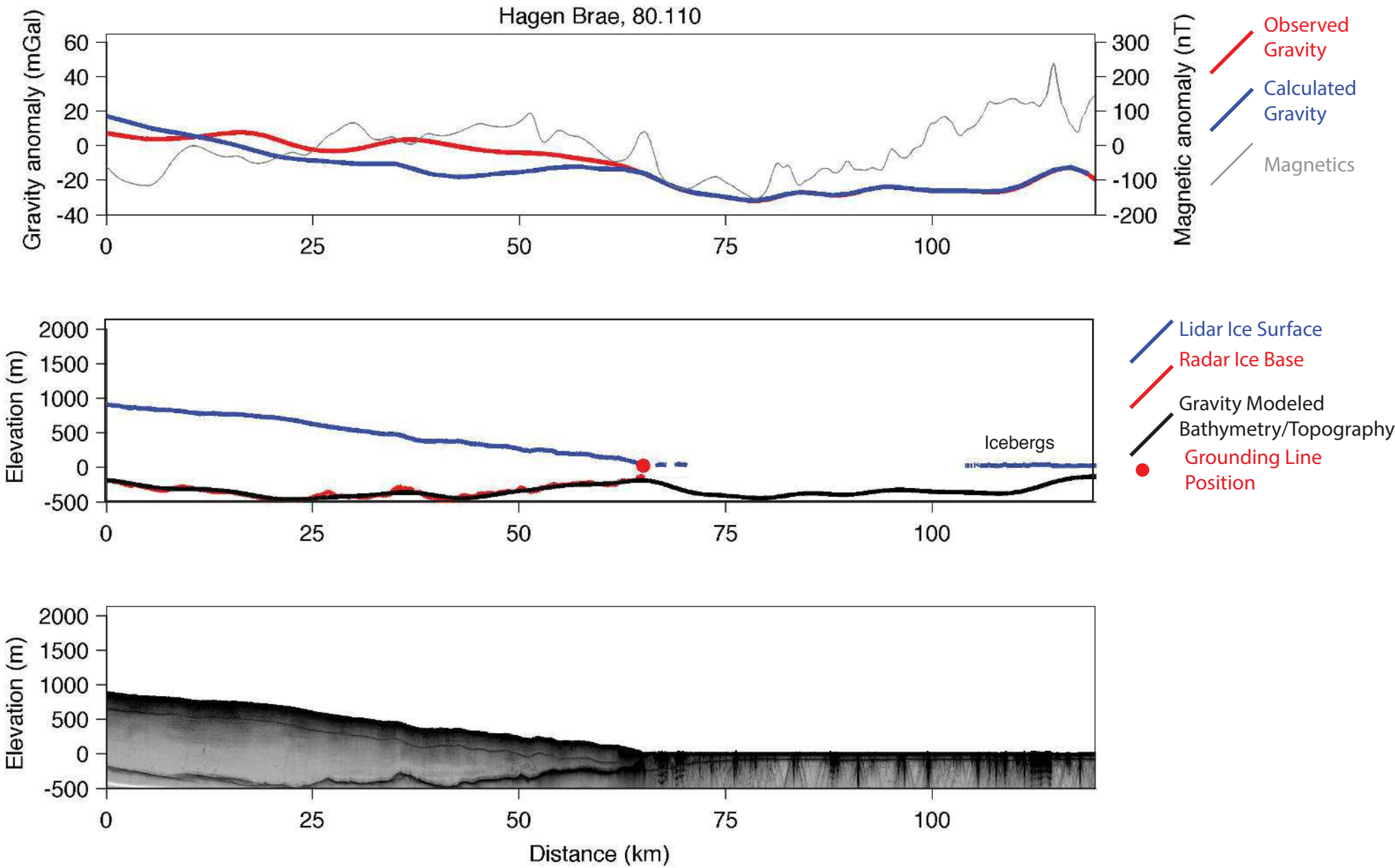
Hagen Brae, 80.110
Gravity anomaly (mGal)
60
40
20
0
-20
-40
0
25
50
75
100
300
200
100
0
-100
-200
Magnetic anomaly (nT)
Observed Gravity
Calculated Gravity
Magnetics
Elevation (m)
2000
1500
1000
500
0
-500
Icebergs
Lidar Ice Surface
Radar Ice Base
Gravity Modeled Bathymetry/Topography
Grounding Line Position
Distance (km)

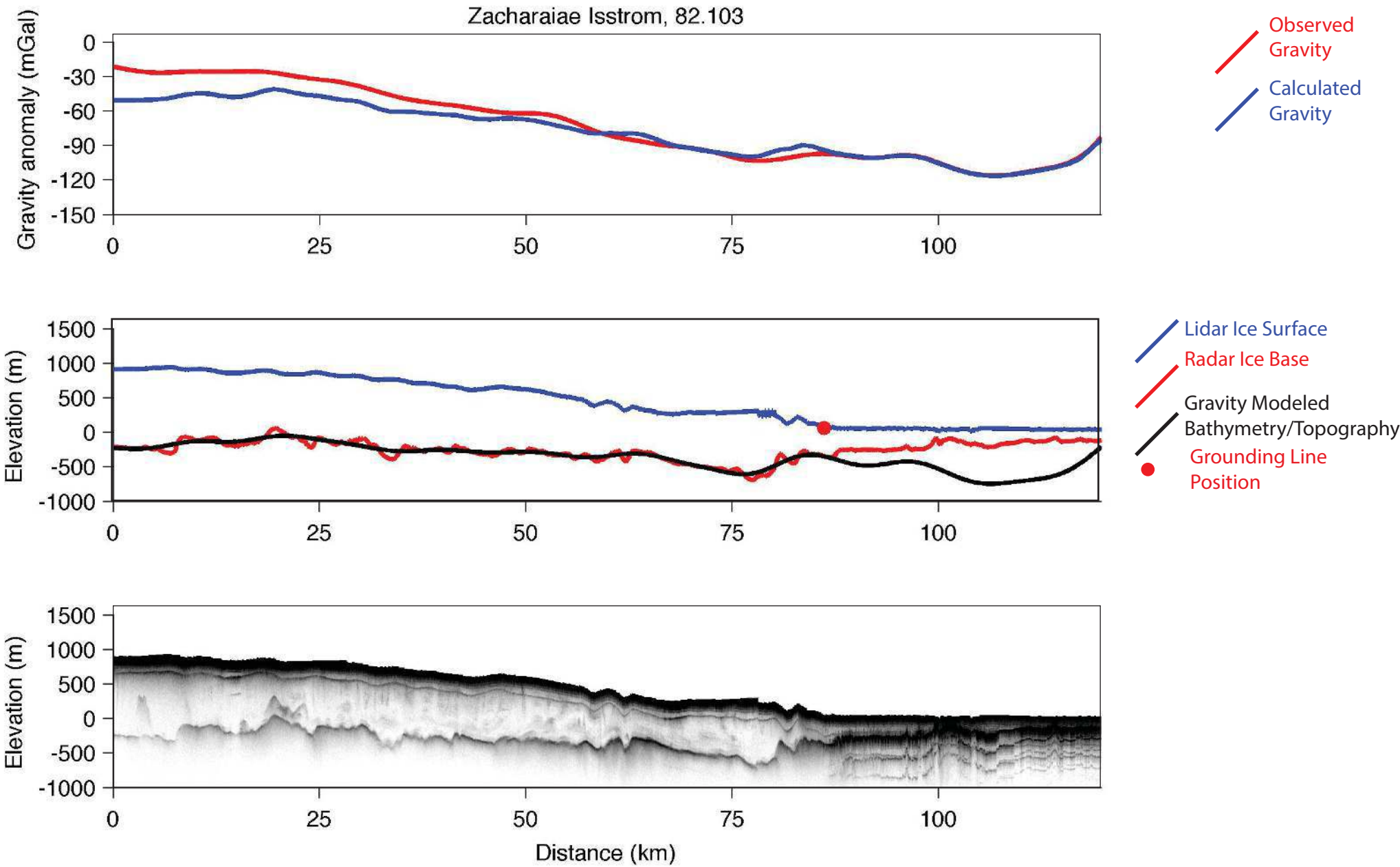
Zacharaiae Isstrom, 82.103
Gravity anomaly (mGal)
0
-30
-60
-90
-120
-150
0
25
50
75
100
Observed Gravity
Calculated Gravity
Elevation (m)
1500
1000
500
0
-500
-1000
Lidar Ice Surface
Radar Ice Base
Gravity Modeled Bathymetry/Topography
Grounding Line Position
Distance (km)

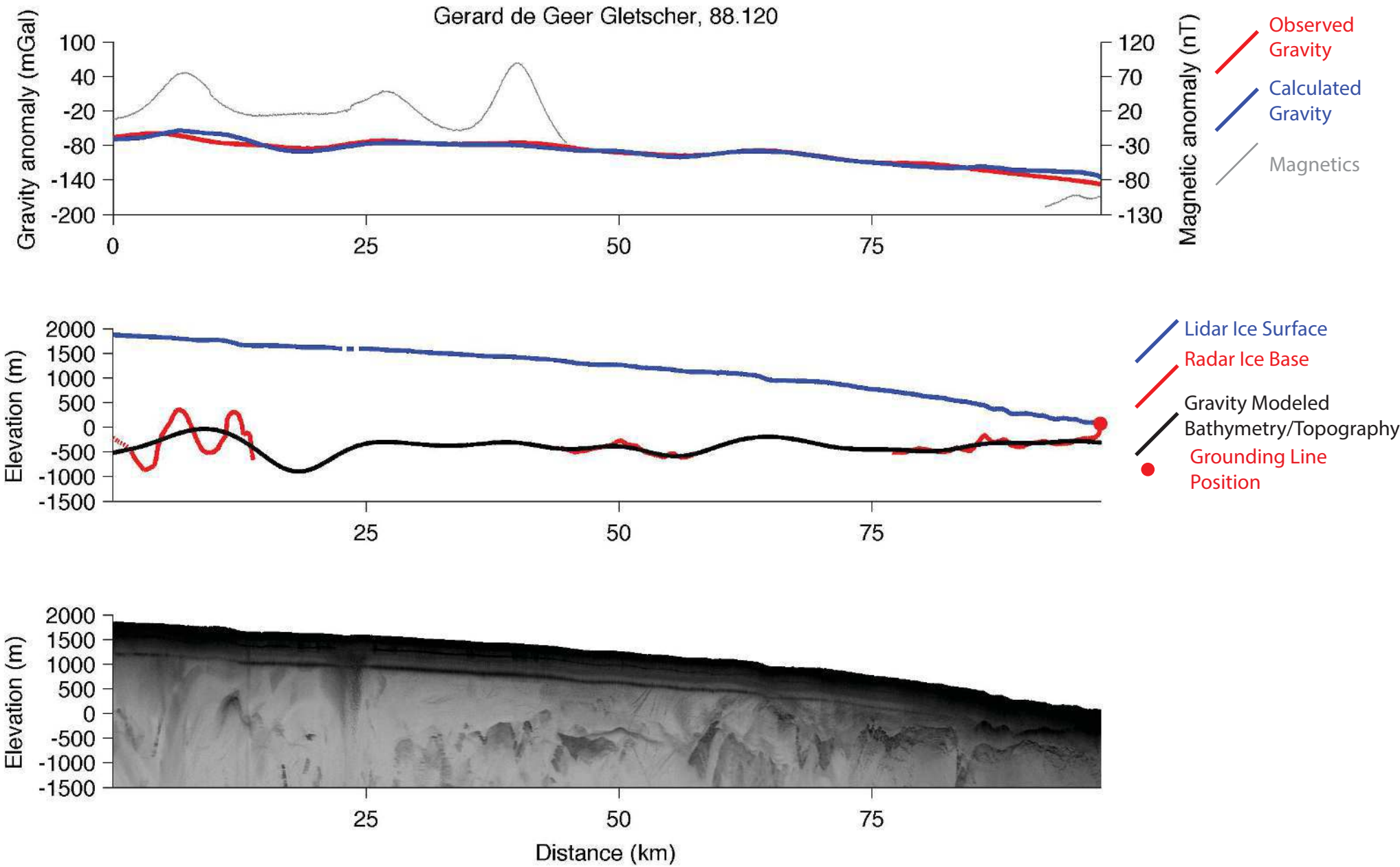
Gerard de Geer Gletscher, 88.120
Gravity anomaly (mGal)
100
40
-20
-80
-140
-200
0
25
50
75
Magnetic anomaly (nT)
120
70
20
-30
-80
-130
Observed Gravity
Calculated Gravity
Magnetics
Elevation (m)
2000
1500
1000
500
0
-500
-1000
-1500
Lidar Ice Surface
Radar Ice Base
Gravity Modeled Bathymetry/Topography
Grounding Line Position
Distance (km)

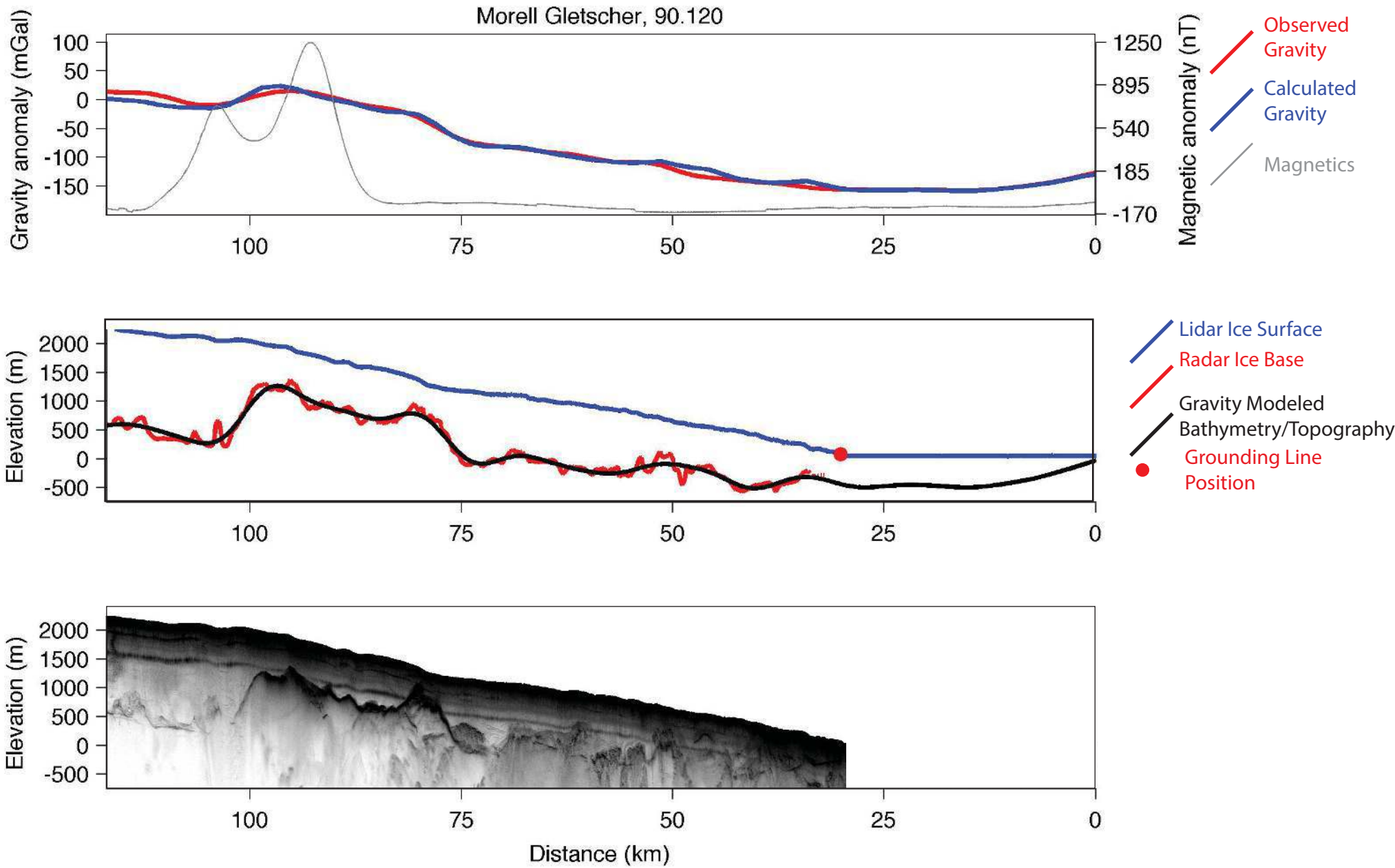
Morell Gletscher, 90.120
Gravity anomaly (mGal)
100
50
0
-50
-100
-150
Magnetic anomaly (nT)
1250
895
540
185
-170
100
75
50
25
0
Observed Gravity
Calculated Gravity
Magnetics
Elevation (m)
2000
1500
1000
500
0
-500
Lidar Ice Surface
Radar Ice Base
Gravity Modeled Bathymetry/Topography
Grounding Line Position
Distance (km)

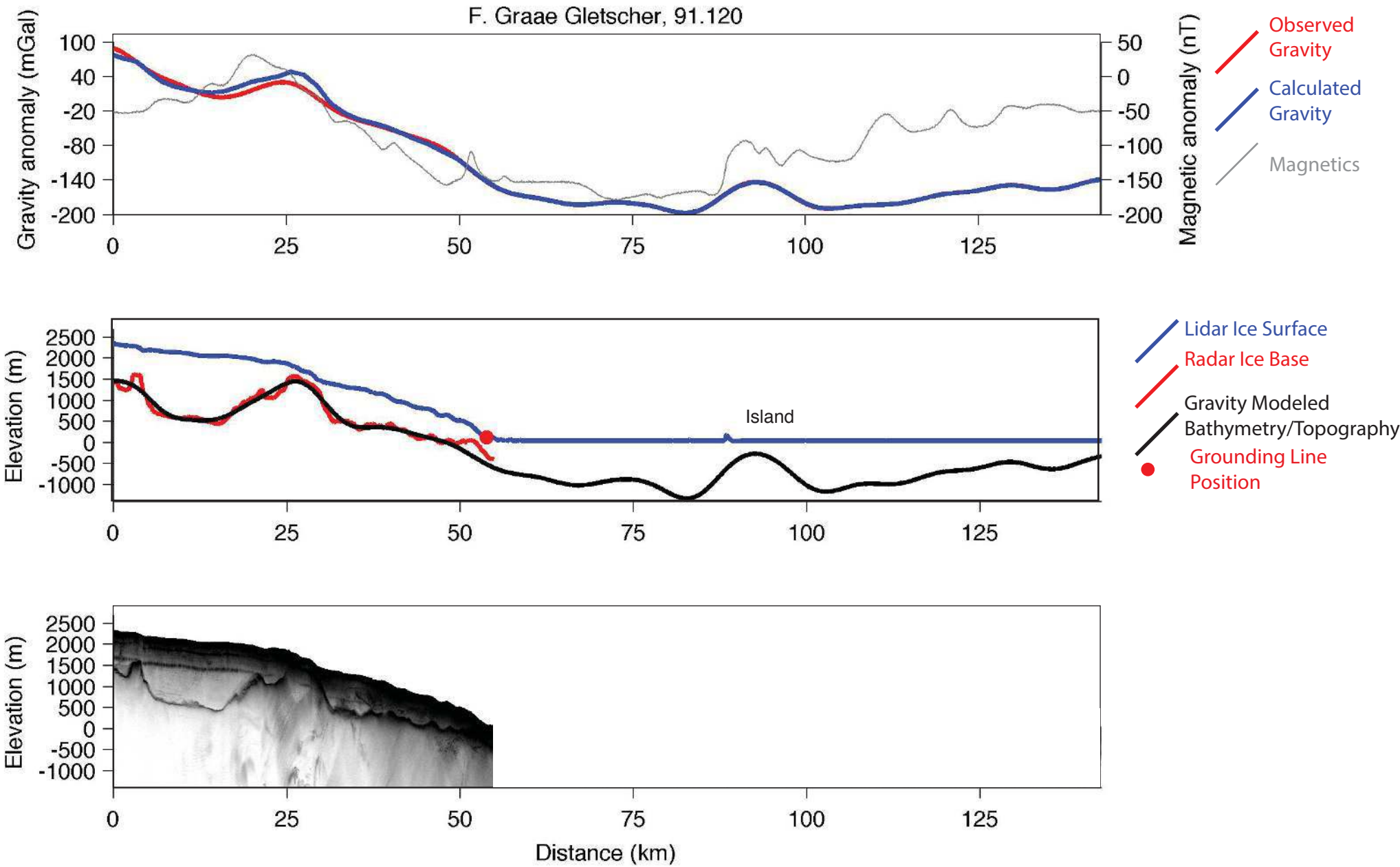
F. Graae Gletscher, 91.120
Gravity anomaly (mGal)
100
40
-20
-80
-140
-200
Magnetic anomaly (nT)
50
0
-50
-100
-150
-200
0
25
50
75
100
125
Observed Gravity
Calculated Gravity
Magnetics
Elevation (m)
2500
2000
1500
1000
500
0
-500
-1000
Island
Lidar Ice Surface
Radar Ice Base
Gravity Modeled Bathymetry/Topography
Grounding Line Position
Distance (km)

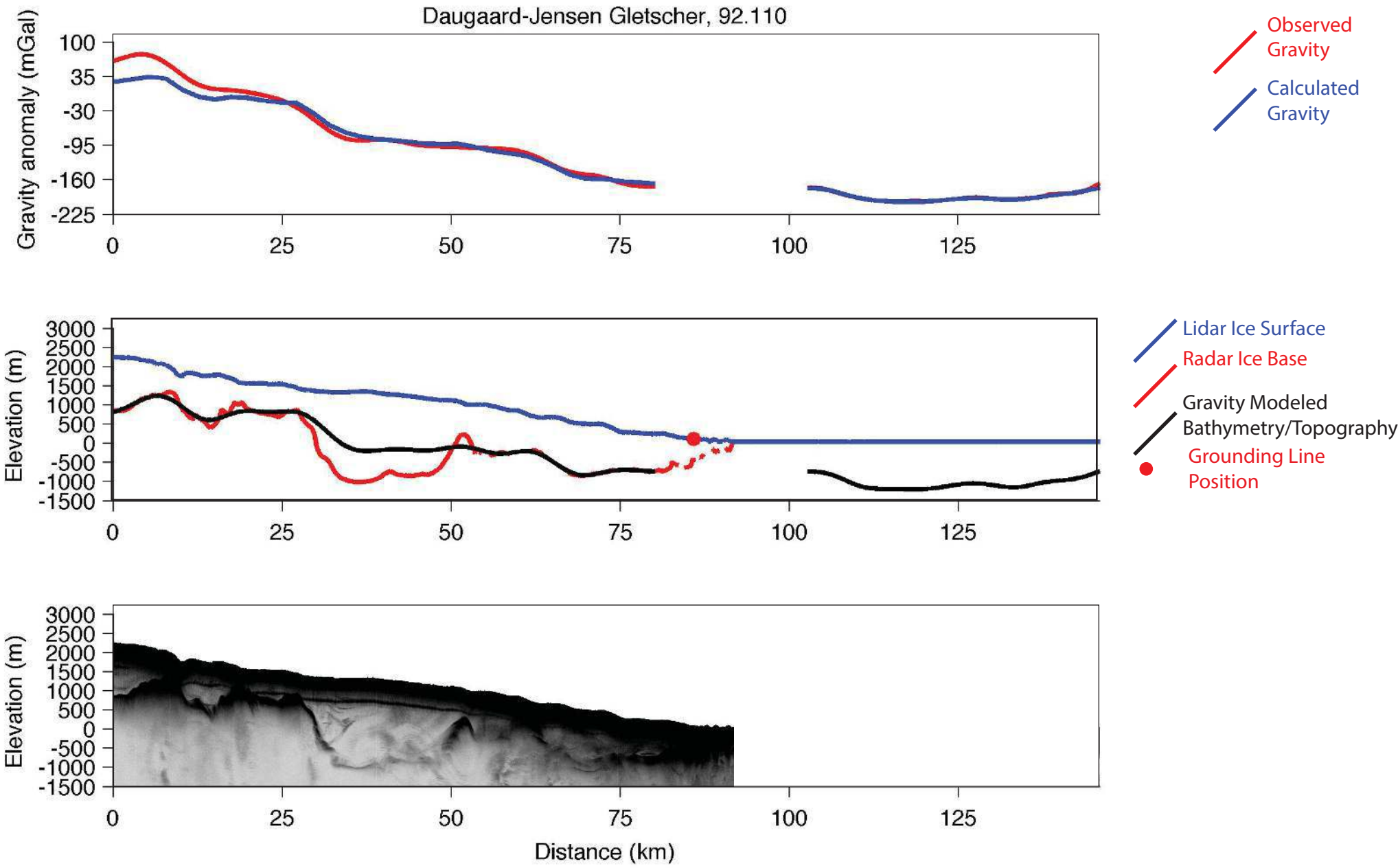
Daugaard-Jensen Gletscher, 92.110
Gravity anomaly (mGal)
100
35
-30
-95
-160
-225
0
25
50
75
100
125
Observed Gravity
Calculated Gravity
Elevation (m)
3000
2500
2000
1500
1000
500
0
-500
-1000
-1500
Lidar Ice Surface
Radar Ice Base
Gravity Modeled Bathymetry/Topography
Grounding Line Position
Distance (km)

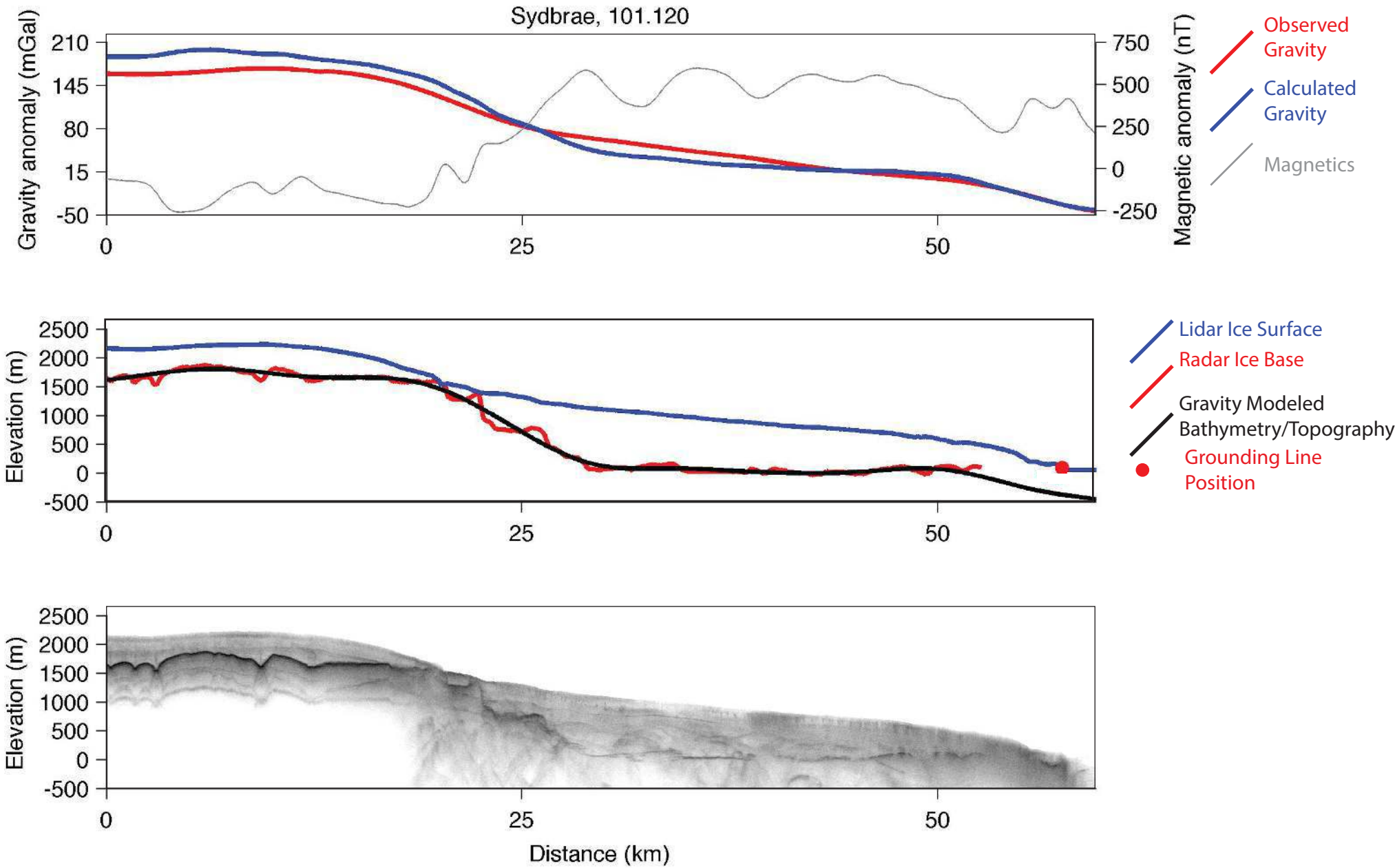
Sydbrae, 101.120
Gravity anomaly (mGal)
210
145
80
15
-50
0
25
50
Magnetic anomaly (nT)
750
500
250
0
-250
Observed Gravity
Calculated Gravity
Magnetics
Elevation (m)
2500
2000
1500
1000
500
0
-500
Lidar Ice Surface
Radar Ice Base
Gravity Modeled Bathymetry/Topography
Grounding Line Position
Distance (km)

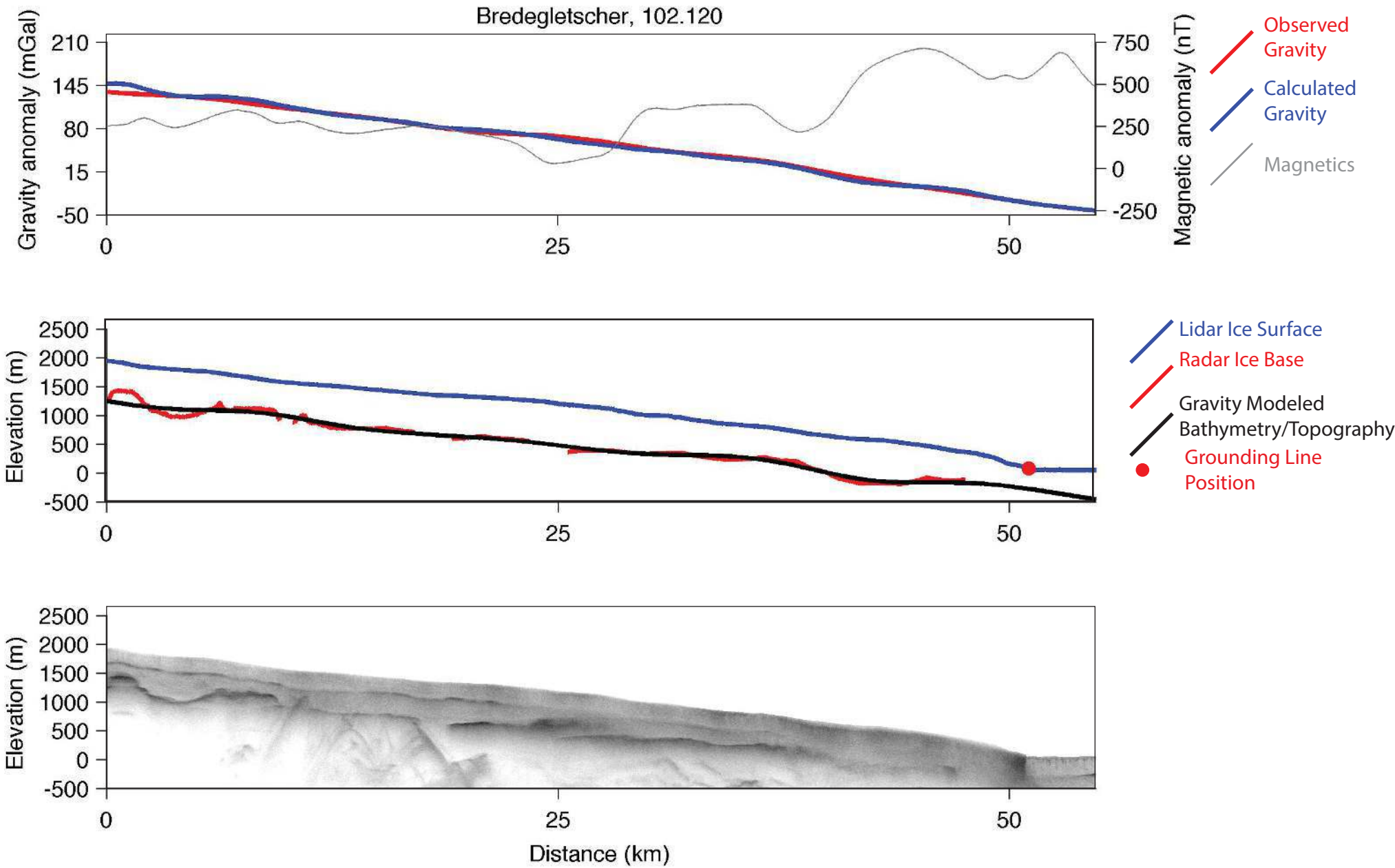
Bredegletscher, 102.120
Gravity anomaly (mGal)
210
145
80
15
-50
0
25
50
Magnetic anomaly (nT)
750
500
250
0
-250
Observed Gravity
Calculated Gravity
Magnetics
Elevation (m)
2500
2000
1500
1000
500
0
-500
Lidar Ice Surface
Radar Ice Base
Gravity Modeled Bathymetry/Topography
Grounding Line Position
Distance (km)

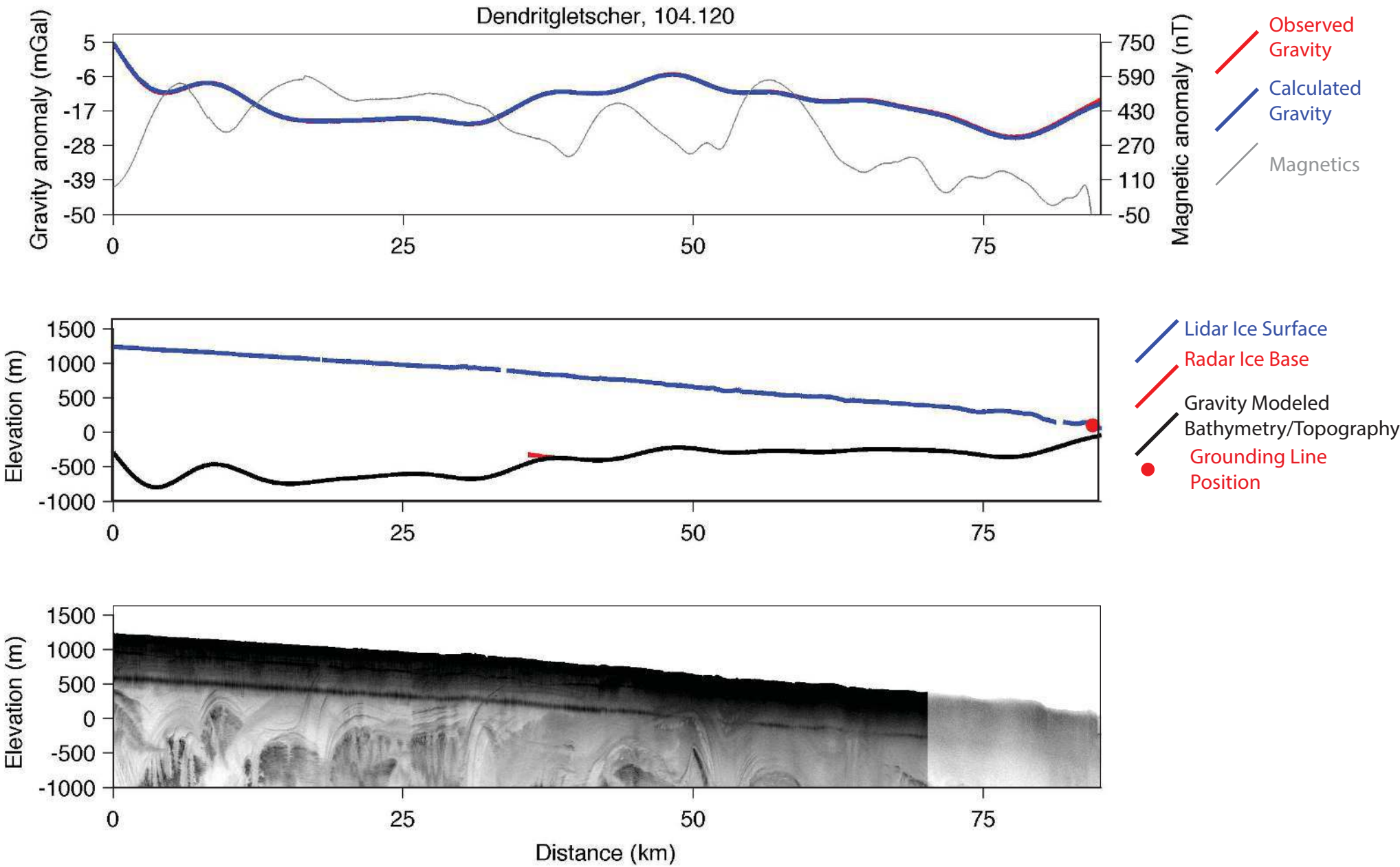
Dendritgletscher, 104.120
Gravity anomaly (mGal)
5
-6
-17
-28
-39
-50
Magnetic anomaly (nT)
750
590
430
270
110
-50
0
25
50
75
Observed Gravity
Calculated Gravity
Magnetics
Elevation (m)
1500
1000
500
0
-500
-1000
Lidar Ice Surface
Radar Ice Base
Gravity Modeled Bathymetry/Topography
Grounding Line Position
Distance (km)

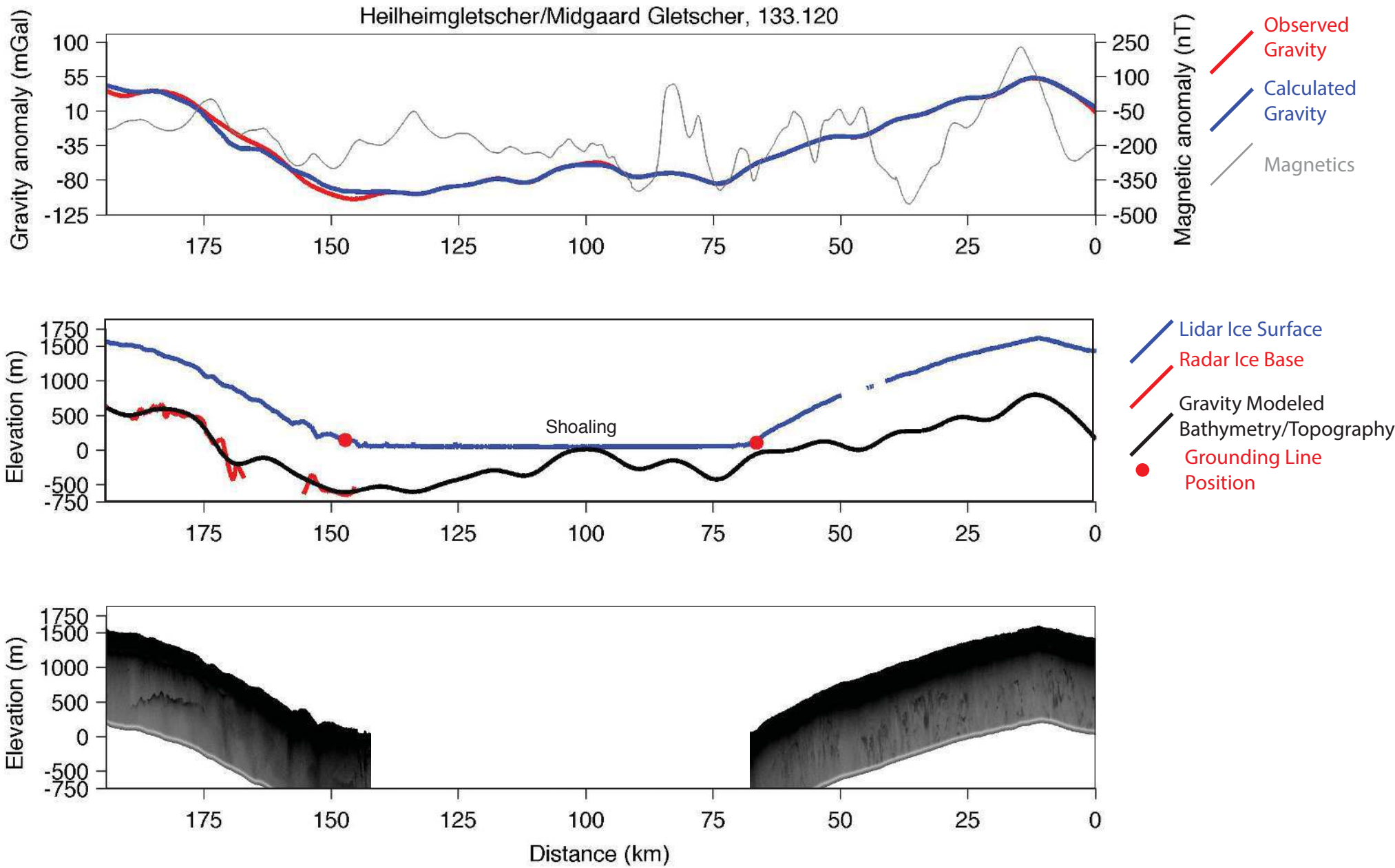
Heilheimgletscher/Midgaard Gletscher, 133.120
Gravity anomaly (mGal)
100
55
10
-35
-80
-125
Magnetic anomaly (nT)
250
100
-50
-200
-350
-500
175
150
125
100
75
50
25
0
Observed Gravity
Calculated Gravity
Magnetics
Elevation (m)
1750
1500
1000
500
0
-500
-750
Shoaling
Lidar Ice Surface
Radar Ice Base
Gravity Modeled Bathymetry/Topography
Grounding Line Position
Distance (km)

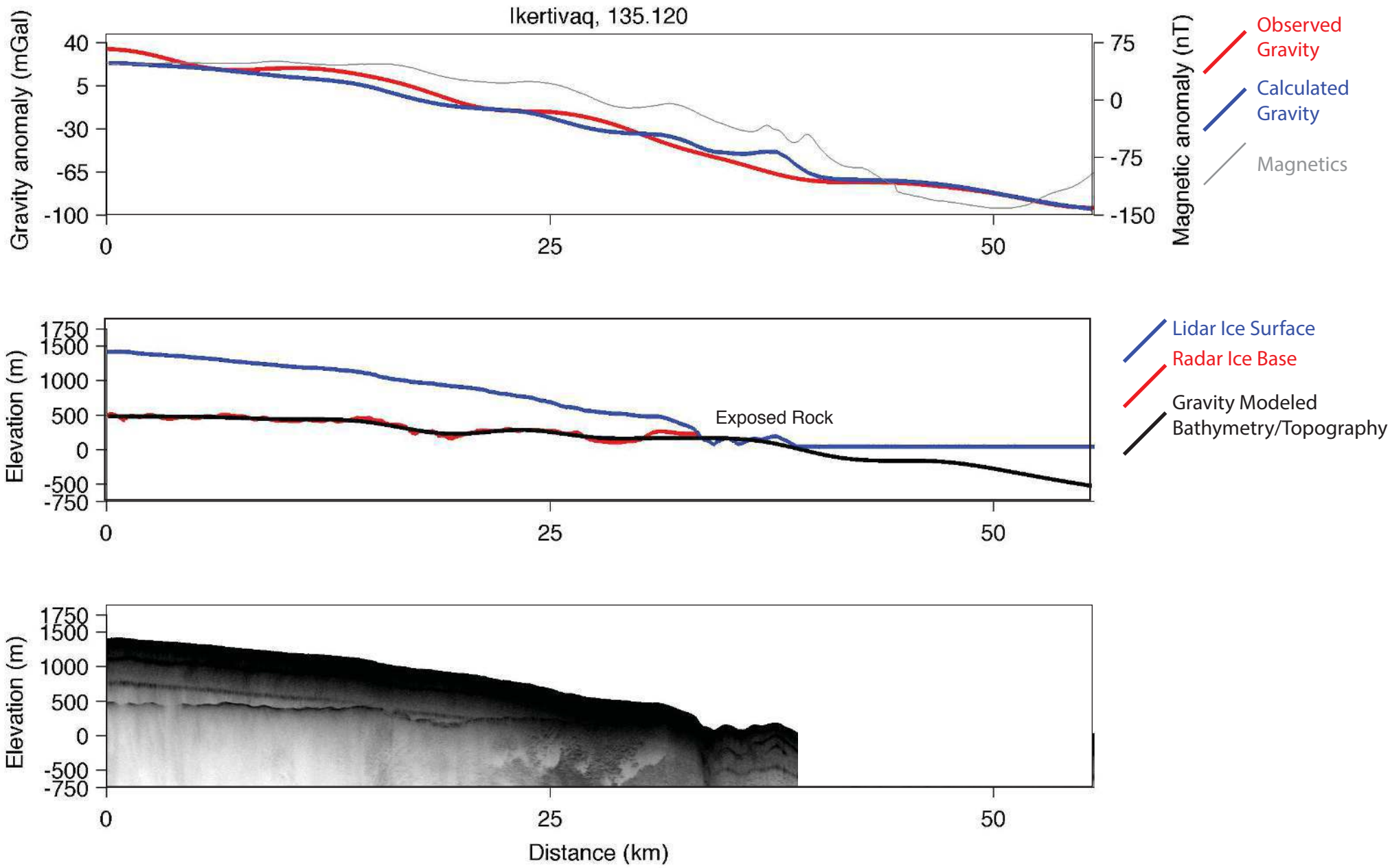
Ikertivaq, 135.120
Gravity anomaly (mGal)
40
5
-30
-65
-100
75
0
-75
-150
Magnetic anomaly (nT)
0
25
50
Observed Gravity
Calculated Gravity
Magnetics
Elevation (m)
1750
1500
1000
500
0
-500
-750
Exposed Rock
Lidar Ice Surface
Radar Ice Base
Gravity Modeled Bathymetry/Topography
Distance (km)

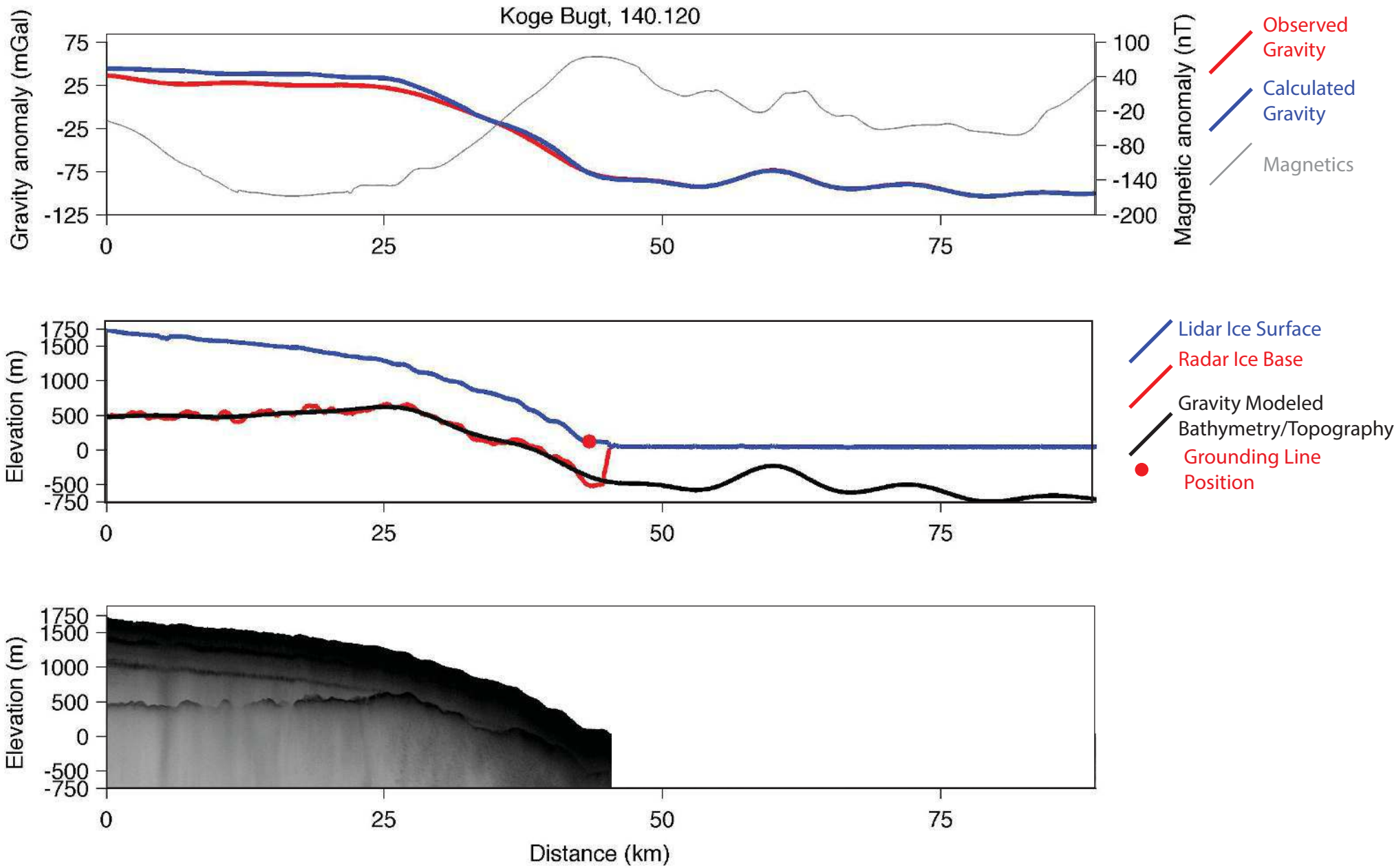
Koge Bugt, 140.120
Gravity anomaly (mGal)
75
25
-25
-75
-125
0
25
50
75
Magnetic anomaly (nT)
100
40
-20
-80
-140
-200
Observed Gravity
Calculated Gravity
Magnetics
Elevation (m)
1750
1500
1000
500
0
-500
-750
Lidar Ice Surface
Radar Ice Base
Gravity Modeled Bathymetry/Topography
Grounding Line Position
Distance (km)

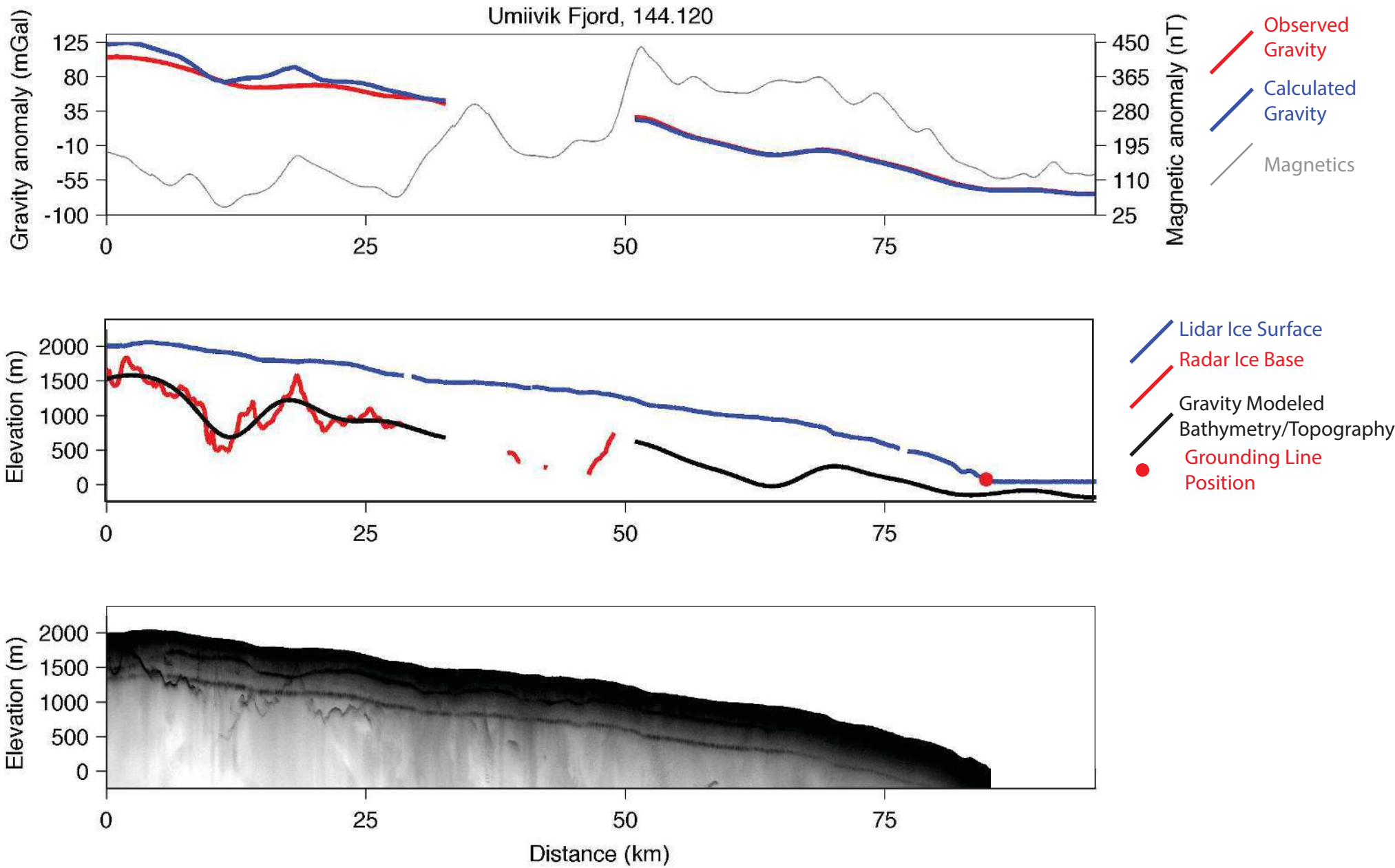
Umiivik Fjord, 144.120
Gravity anomaly (mGal)
125
80
35
-10
-55
-100
Magnetic anomaly (nT)
450
365
280
195
110
25
0
25
50
75
Observed Gravity
Calculated Gravity
Magnetics
Elevation (m)
2000
1500
1000
500
0
Lidar Ice Surface
Radar Ice Base
Gravity Modeled Bathymetry/Topography
Grounding Line Position
Distance (km)

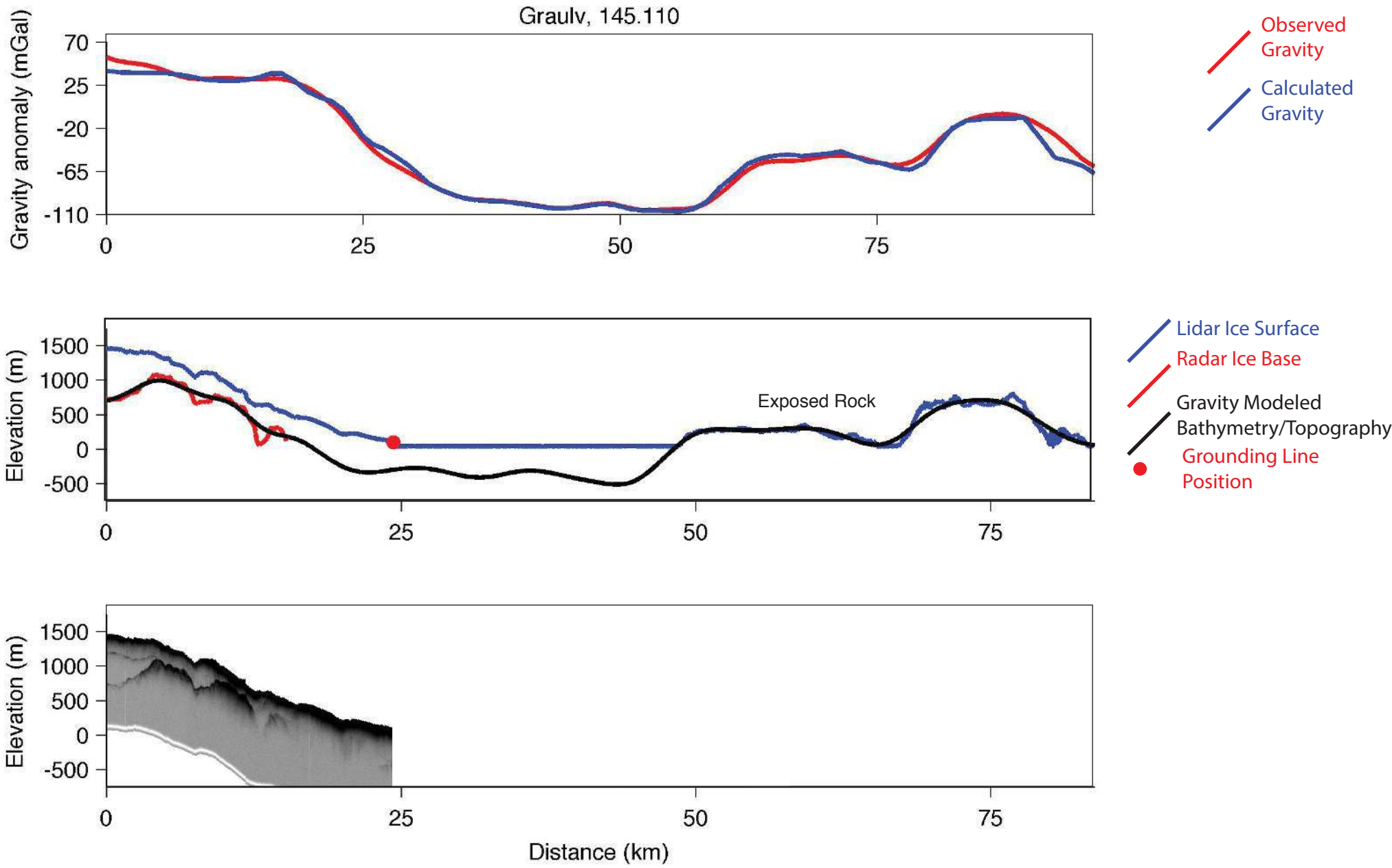
Graulv, 145.110
Gravity anomaly (mGal)
70
25
-20
-65
-110
0
25
50
75
Observed Gravity
Calculated Gravity
Elevation (m)
1500
1000
500
0
-500
Exposed Rock
Lidar Ice Surface
Radar Ice Base
Gravity Modeled
Bathymetry/Topography
Grounding Line Position
Distance (km)

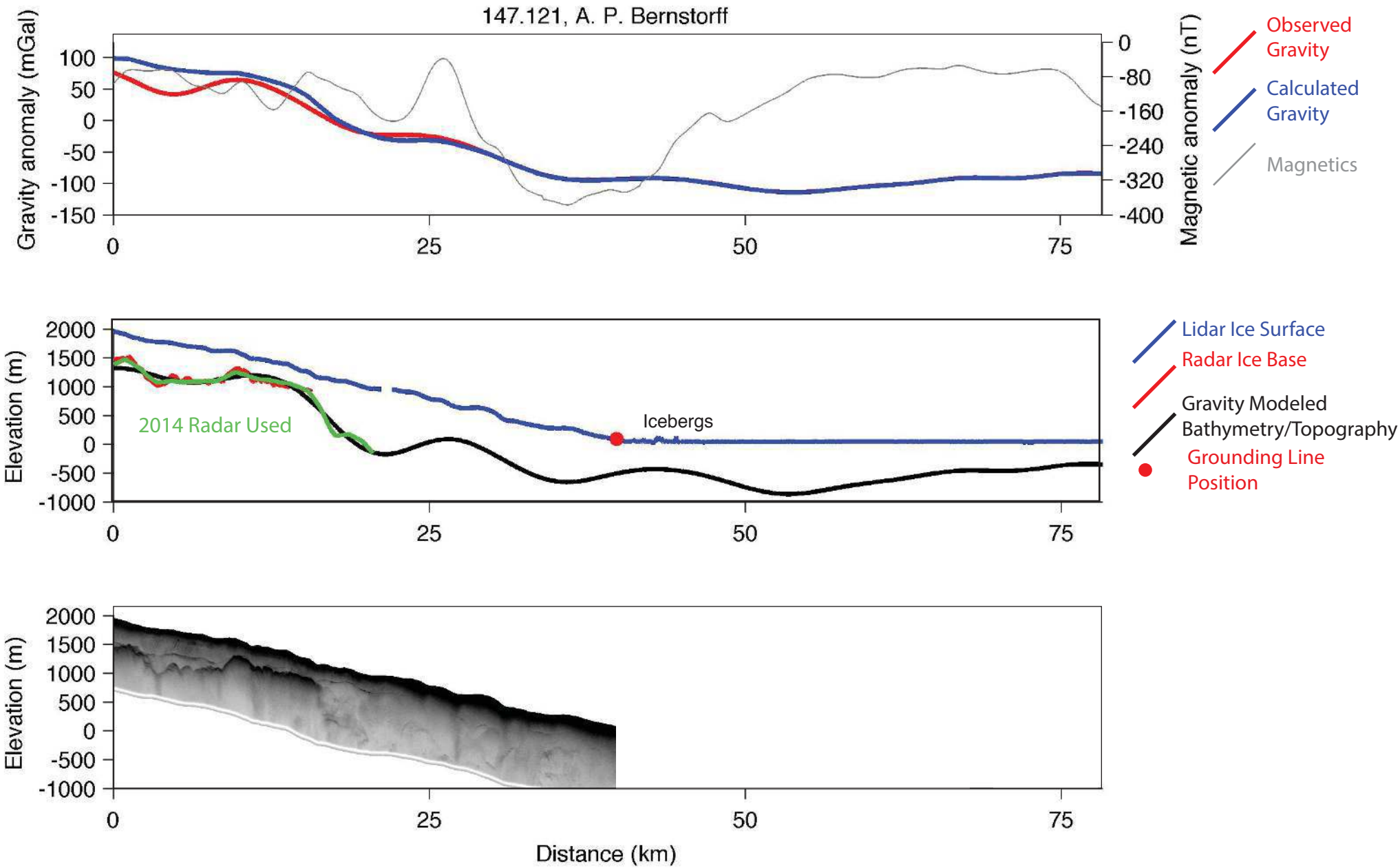
147.121, A. P. Bernstorff
Gravity anomaly (mGal)
100
50
0
-50
-100
-150
0
25
50
75
Magnetic anomaly (nT)
0
-80
-160
-240
-320
-400
Observed Gravity
Calculated Gravity
Magnetics
Elevation (m)
2000
1500
1000
500
0
-500
-1000
2014 Radar Used
Icebergs
Lidar Ice Surface
Radar Ice Base
Gravity Modeled Bathymetry/Topography
Grounding Line Position
Distance (km)

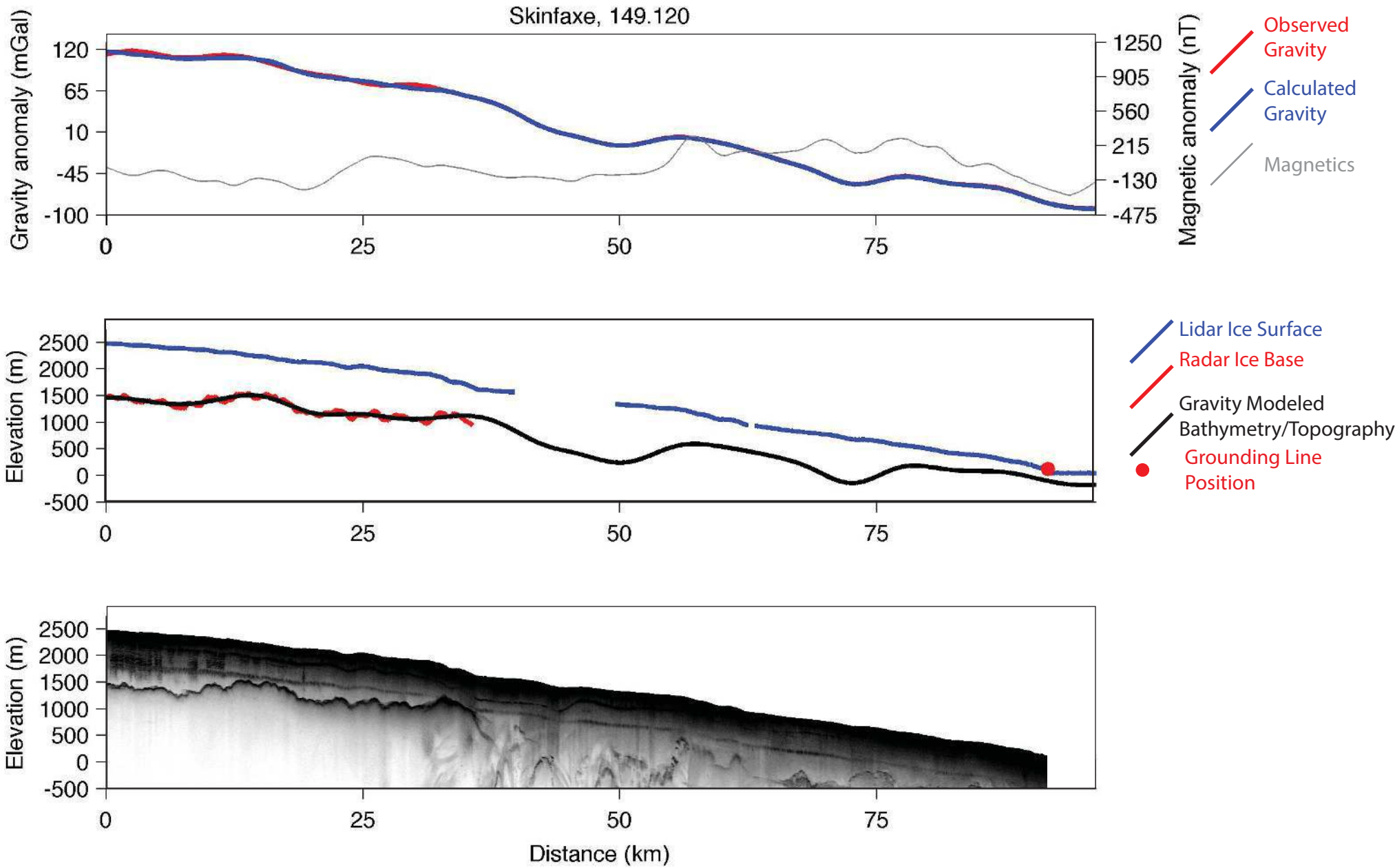
Skinfaxe, 149.120
Gravity anomaly (mGal)
120
65
10
-45
-100
0
25
50
75
1250
905
560
215
-130
-475
Magnetic anomaly (nT)
Observed Gravity
Calculated Gravity
Magnetics
Elevation (m)
2500
2000
1500
1000
500
0
-500
Lidar Ice Surface
Radar Ice Base
Gravity Modeled Bathymetry/Topography
Grounding Line Position
Distance (km)

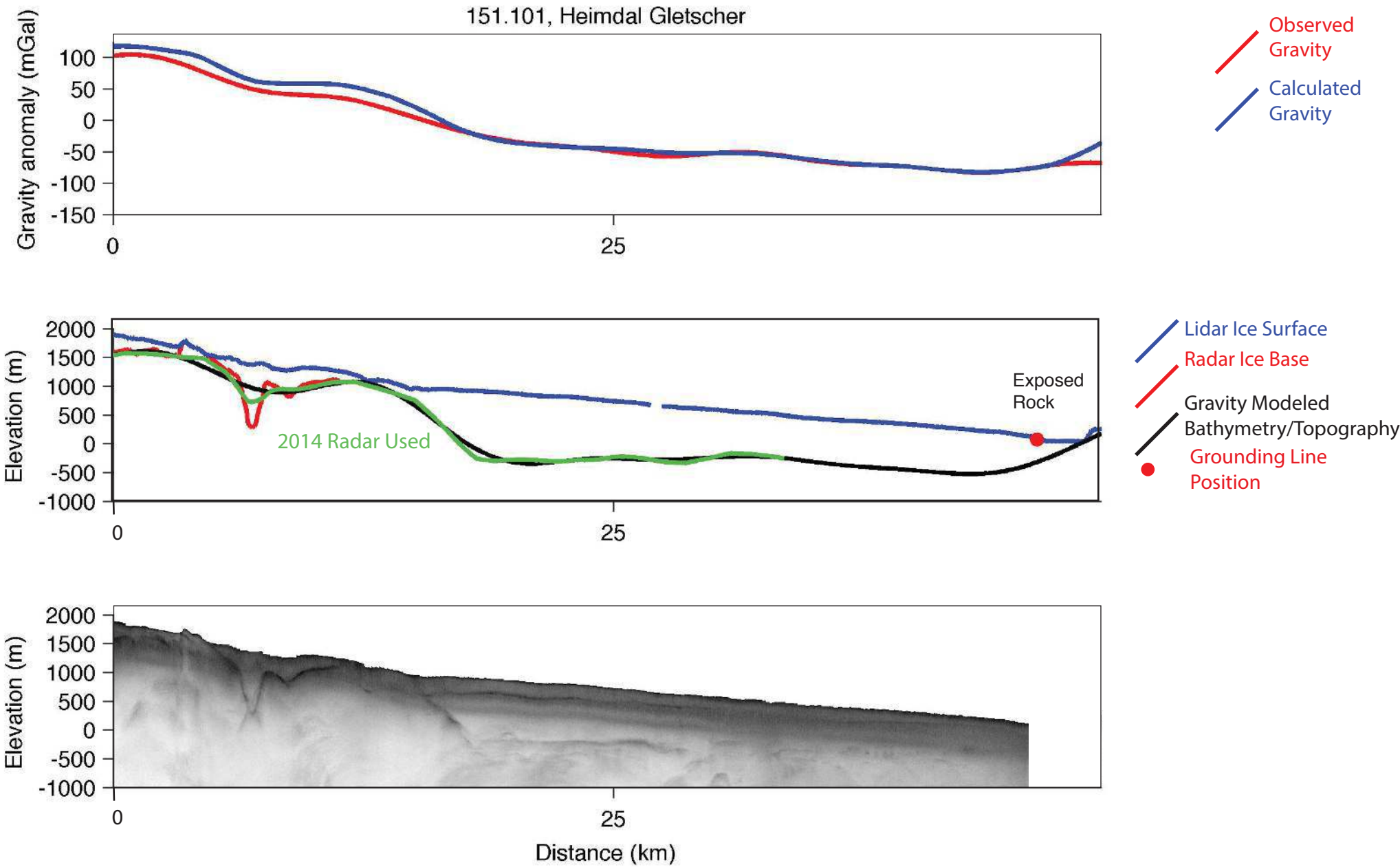
151.101, Heimdal Gletscher
Gravity anomaly (mGal)
100
50
0
-50
-100
-150
0
25
Observed Gravity
Calculated Gravity
Elevation (m)
2000
1500
1000
500
0
-500
-1000
2014 Radar Used
Exposed Rock
Lidar Ice Surface
Radar Ice Base
Gravity Modeled Bathymetry/Topography
Grounding Line Position
Distance (km)

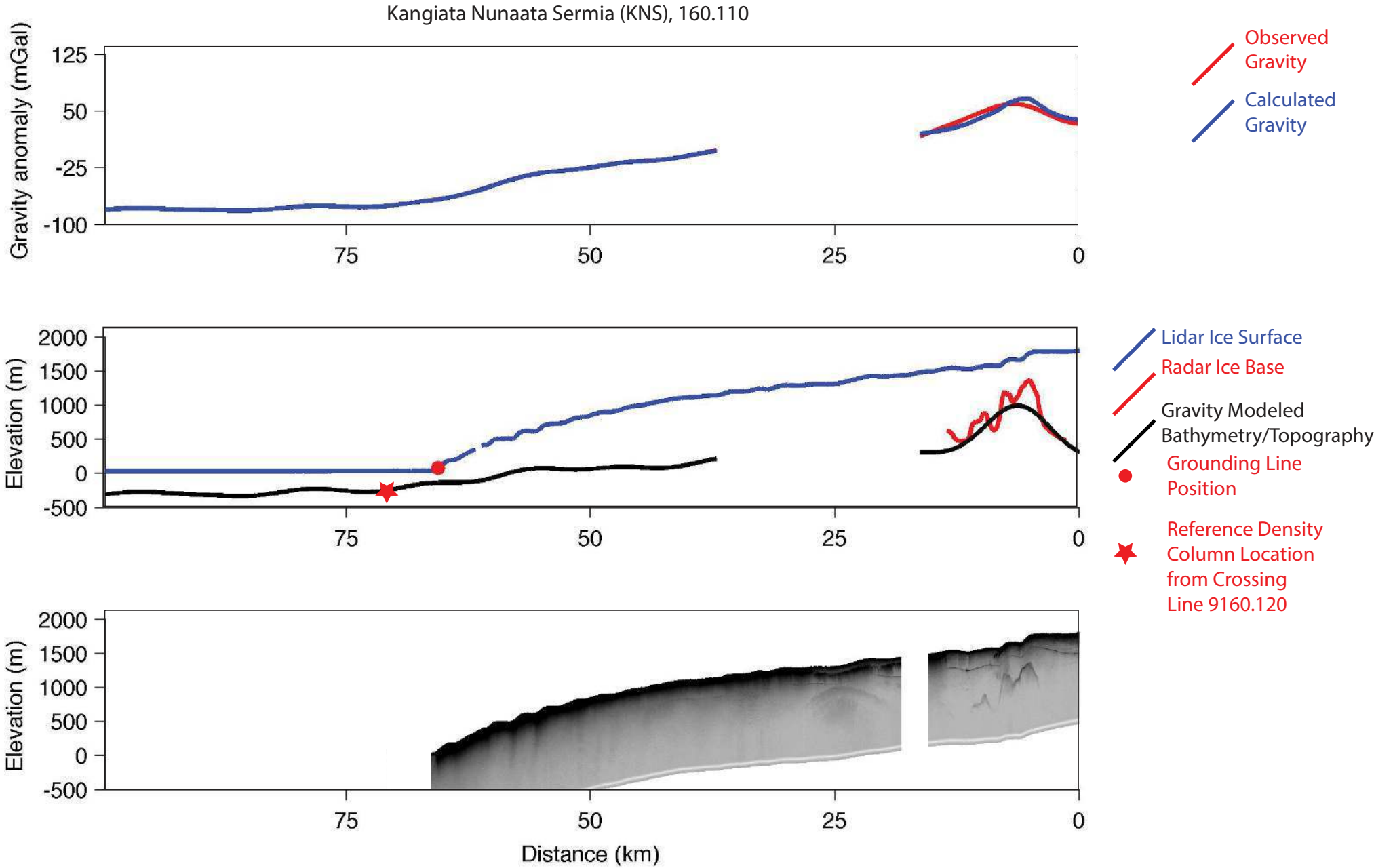
Kangiata Nunaata Sermia (KNS), 160.110
Gravity anomaly (mGal)
125
50
-25
-100
75
50
25
0
Observed Gravity
Calculated Gravity
Elevation (m)
2000
1500
1000
500
0
-500
Lidar Ice Surface
Radar Ice Base
Gravity Modeled Bathymetry/Topography
Grounding Line Position
Reference Density Column Location from Crossing Line 9160.120
Distance (km)

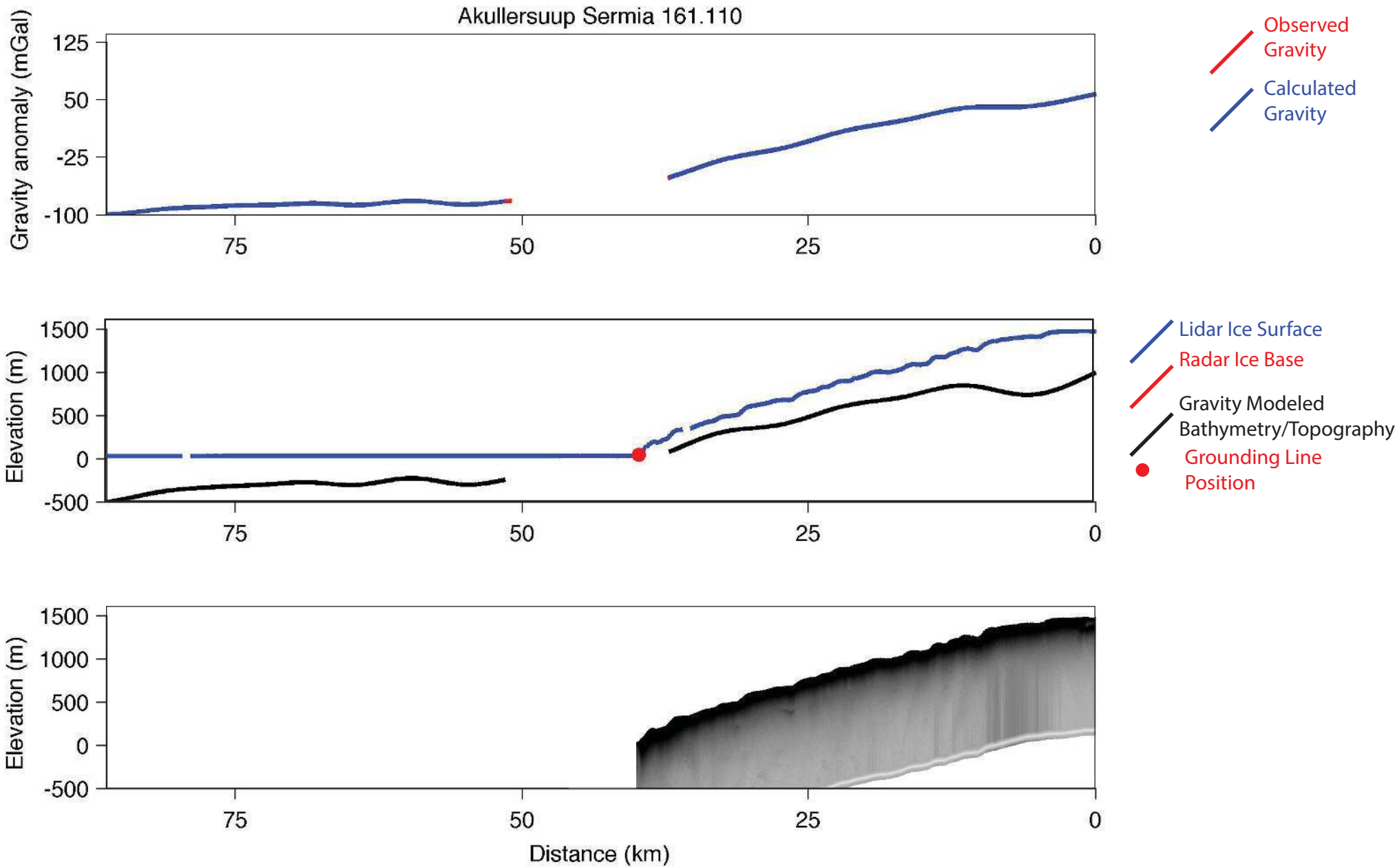
Akullersuup Sermia 161.110
Gravity anomaly (mGal)
125
50
-25
-100
75
50
25
0
Observed Gravity
Calculated Gravity
Elevation (m)
1500
1000
500
0
-500
75
50
25
0
Lidar Ice Surface
Radar Ice Base
Gravity Modeled Bathymetry/Topography
Grounding Line Position
Elevation (m)
1500
1000
500
0
-500
75
50
25
0
Distance (km)

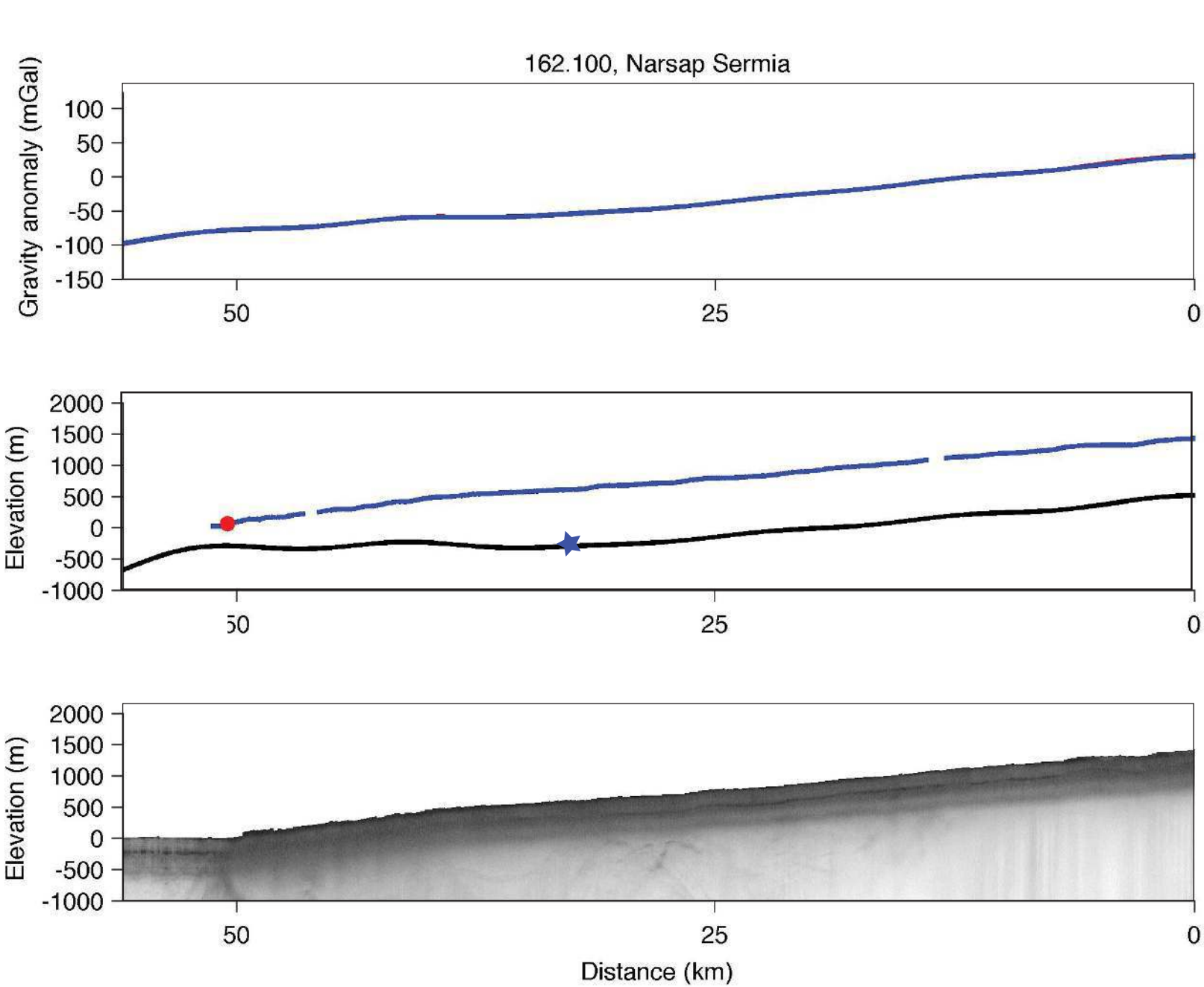
162.100, Narsap Sermia
Gravity anomaly (mGal)
100
50
0
-50
-100
-150
50
25
0
Elevation (m)
2000
1500
1000
500
0
-500
-1000
50
25
0
Elevation (m)
2000
1500
1000
500
0
-500
-1000
50
25
0
Distance (km)
Observed Gravity
Calculated Gravity
Lidar Ice Surface
Radar Ice Base
Gravity Modeled Bathymetry/Topography
Grounding Line Position
Reference Density Column Location from Crossing Line 9160.120

Petermann Gletscher, 193.110

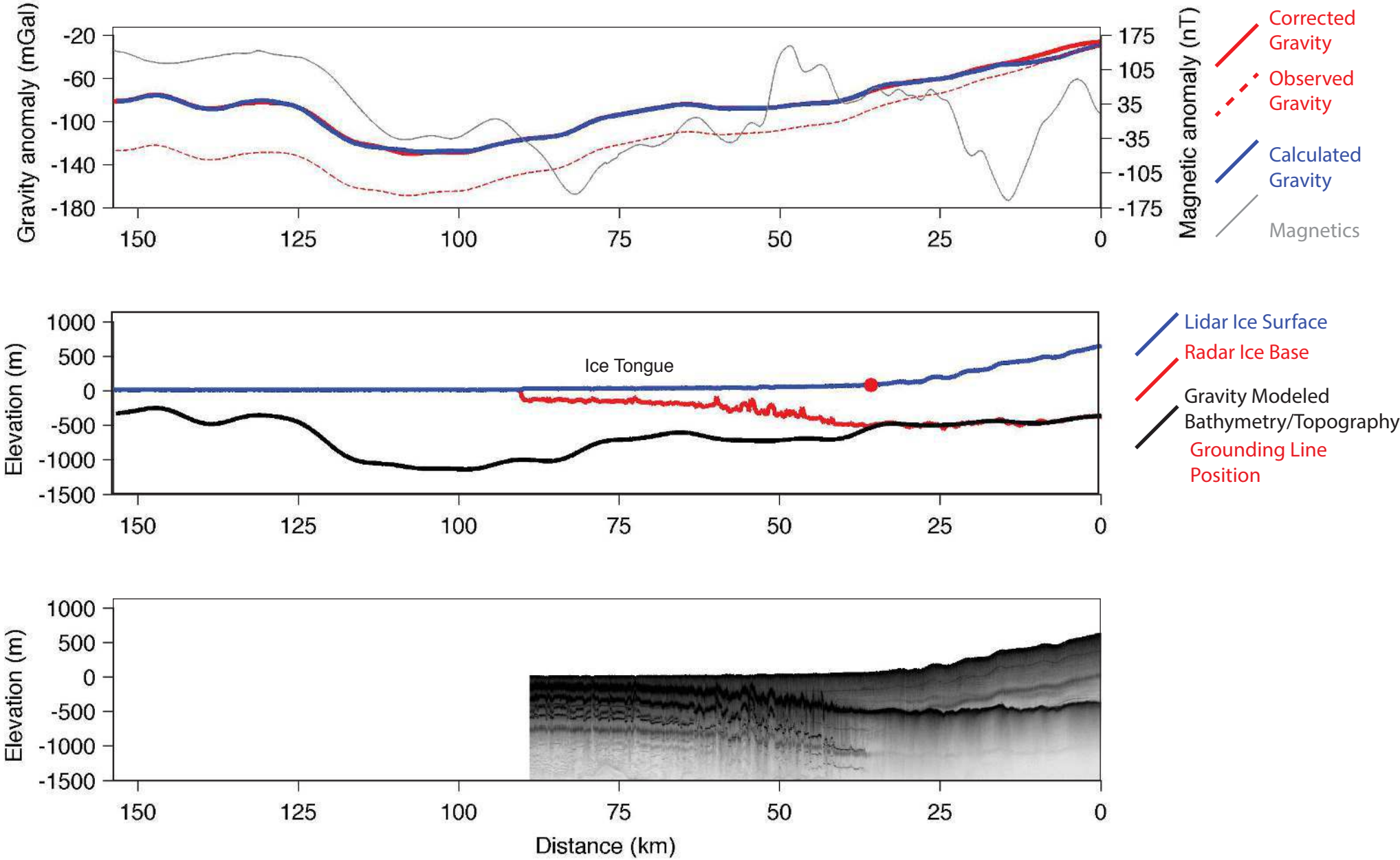

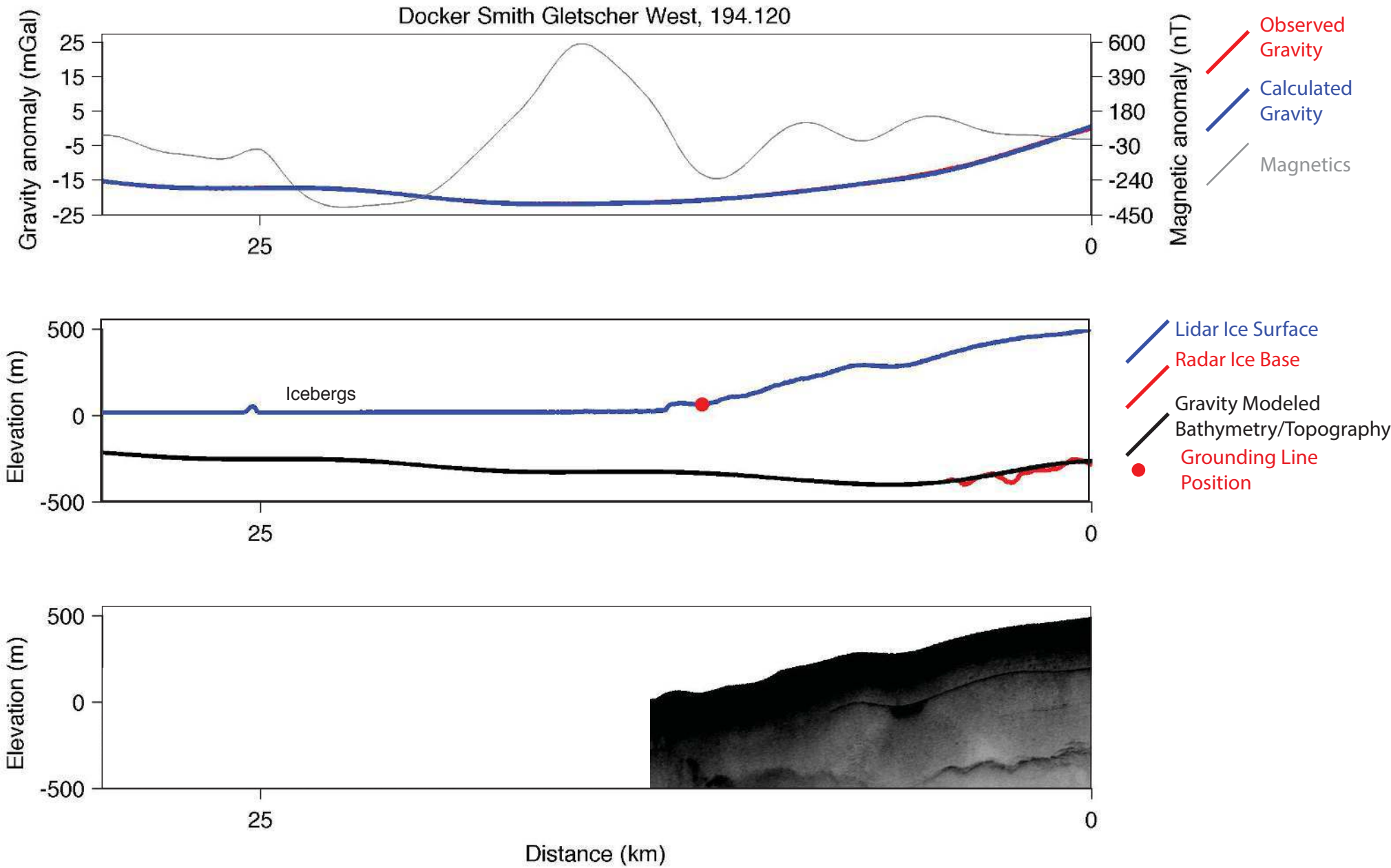
Docker Smith Gletscher West, 194.120
Gravity anomaly (mGal)
25
15
5
-5
-15
-25
25
0
600
390
180
-30
-240
-450
Magnetic anomaly (nT)
Observed Gravity
Calculated Gravity
Magnetics
Elevation (m)
500
0
-500
Icebergs
25
0
Lidar Ice Surface
Radar Ice Base
Gravity Modeled Bathymetry/Topography
Grounding Line Position
Elevation (m)
500
0
-500
25
0
Distance (km)

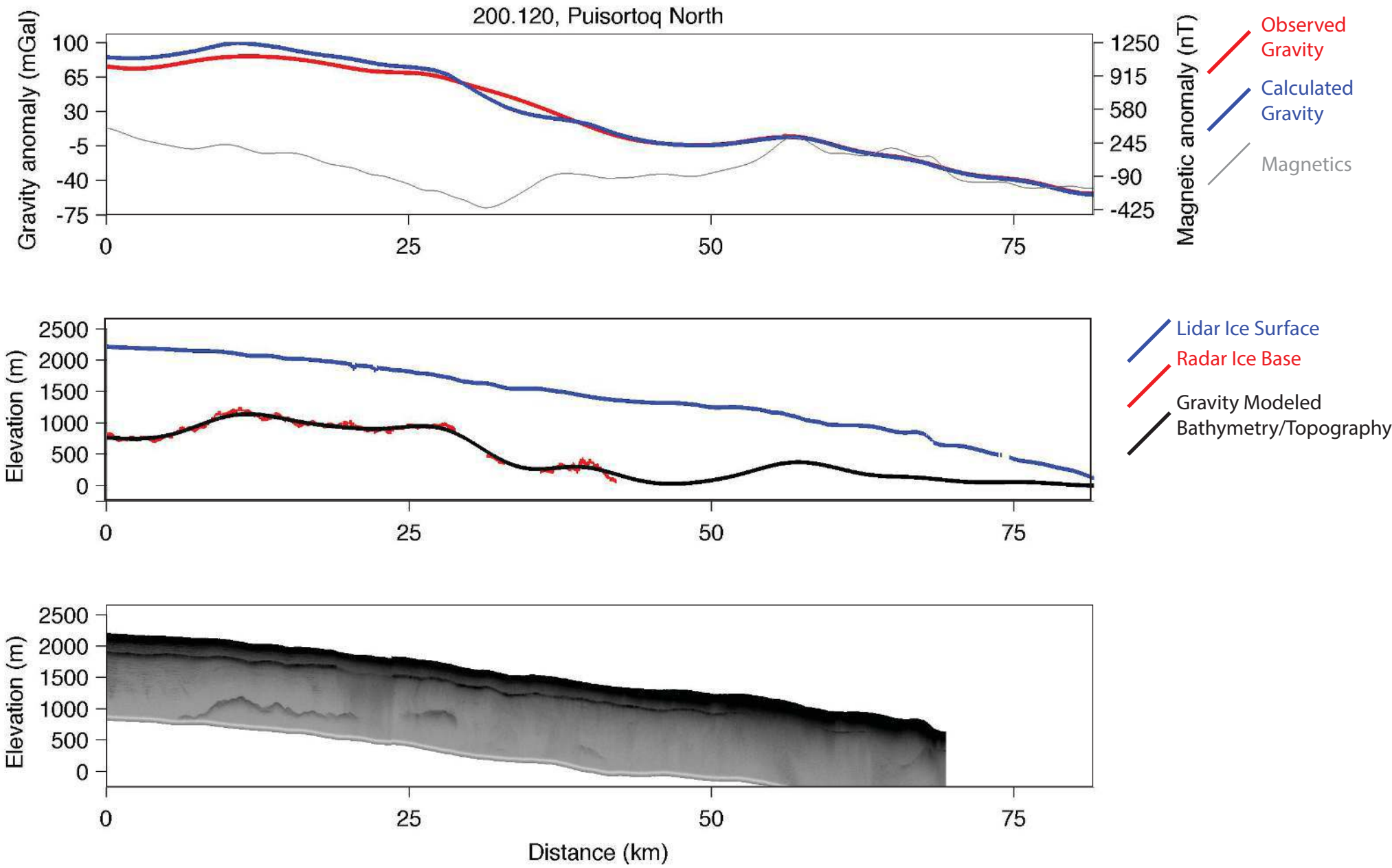
200.120, Puisortoq North
Gravity anomaly (mGal)
100
65
30
-5
-40
-75
1250
915
580
245
-90
-425
Magnetic anomaly (nT)
0
25
50
75
Observed Gravity
Calculated Gravity
Magnetics
Elevation (m)
2500
2000
1500
1000
500
0
Lidar Ice Surface
Radar Ice Base
Gravity Modeled Bathymetry/Topography
Distance (km)

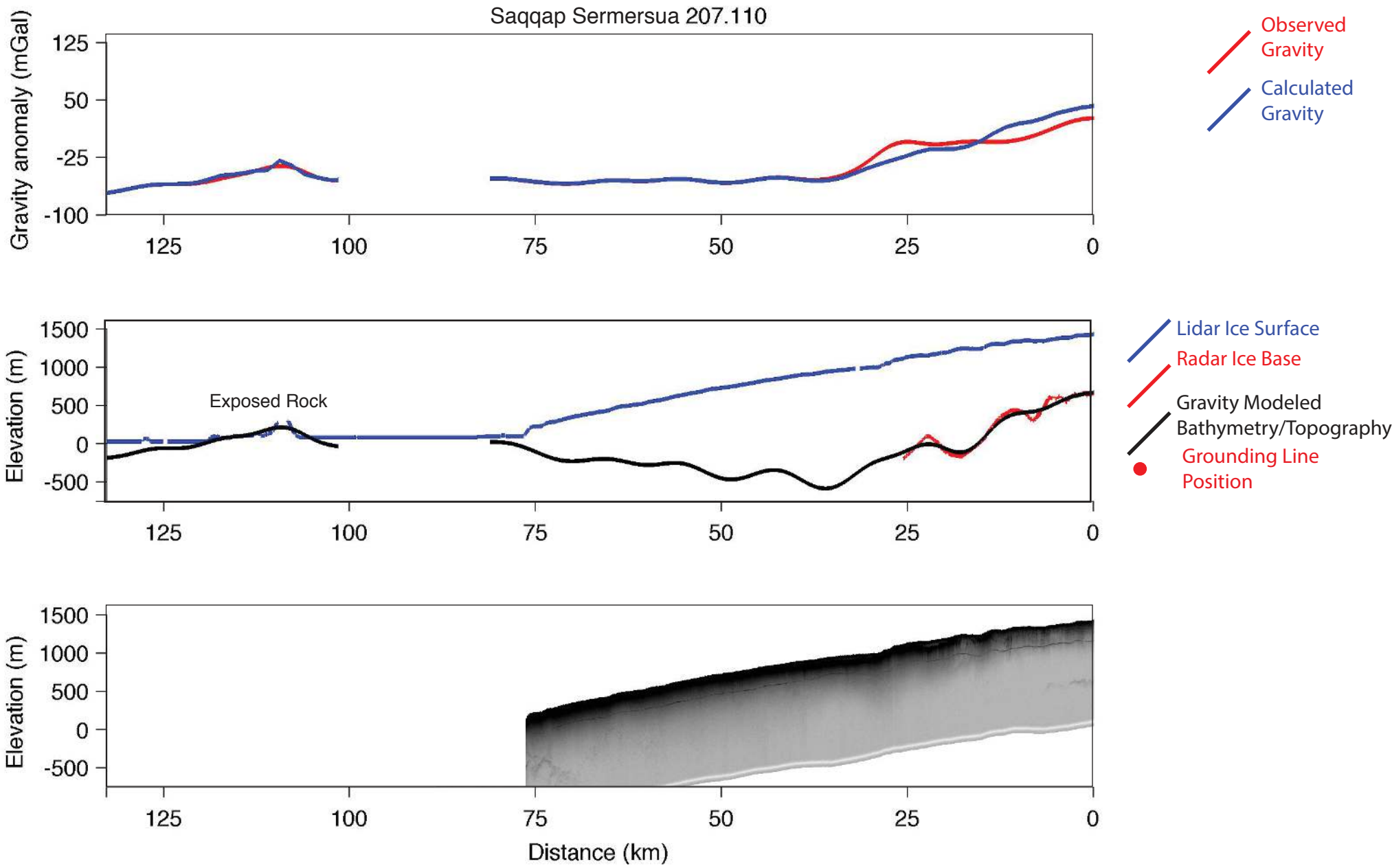
Saqqap Sermersua 207.110
Gravity anomaly (mGal)
125
50
-25
-100
125
100
75
50
25
0
Observed Gravity
Calculated Gravity
Elevation (m)
1500
1000
500
0
-500
Exposed Rock
Lidar Ice Surface
Radar Ice Base
Gravity Modeled Bathymetry/Topography
Grounding Line Position
Distance (km)

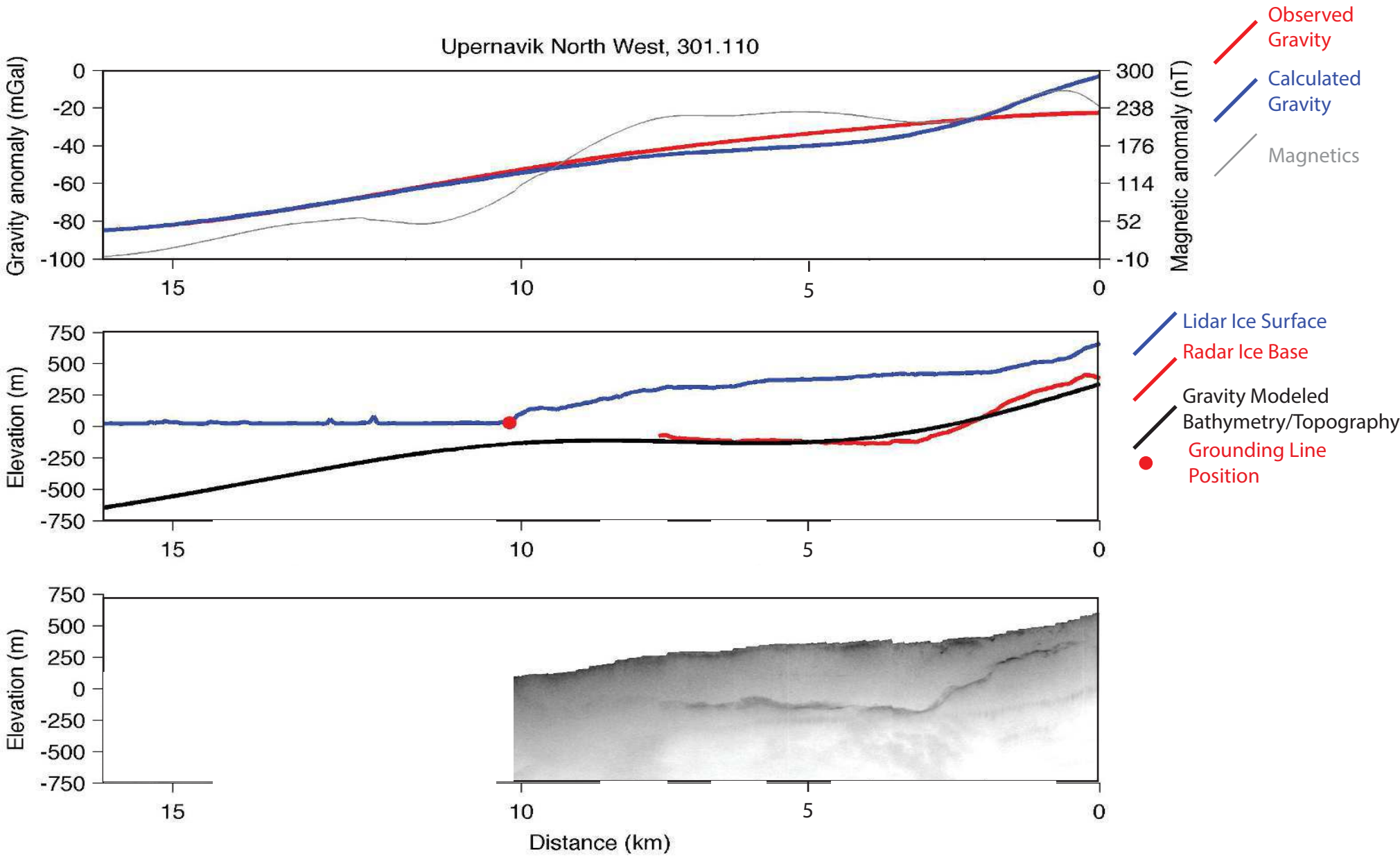
Upernavik North West, 301.110
Gravity anomaly (mGal)
0
-20
-40
-60
-80
-100
Magnetic anomaly (nT)
300
238
176
114
52
-10
15
10
5
0
Observed Gravity
Calculated Gravity
Magnetics
Elevation (m)
750
500
250
0
-250
-500
-750
Lidar Ice Surface
Radar Ice Base
Gravity Modeled Bathymetry/Topography
Grounding Line Position
Distance (km)

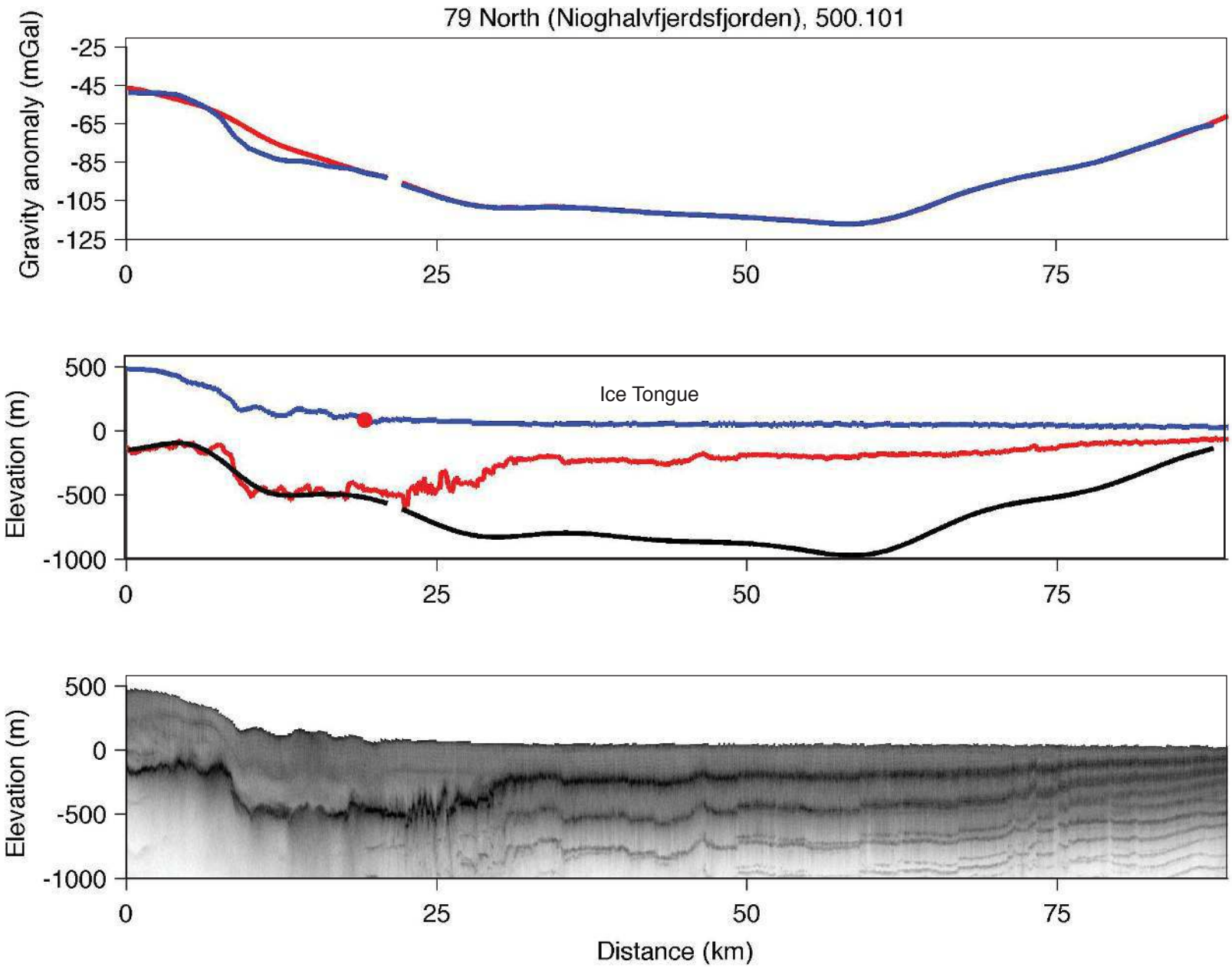
79 North (Nioghalvfjerdsfjorden), 500.101
Gravity anomaly (mGal)
-25
-45
-65
-85
-105
-125
0
25
50
75
Observed Gravity
Calculated Gravity
Elevation (m)
500
0
-500
-1000
Ice Tongue
Lidar Ice Surface
Radar Ice Base
Gravity Modeled Bathymetry/Topography
Grounding Line Position
Distance (km)

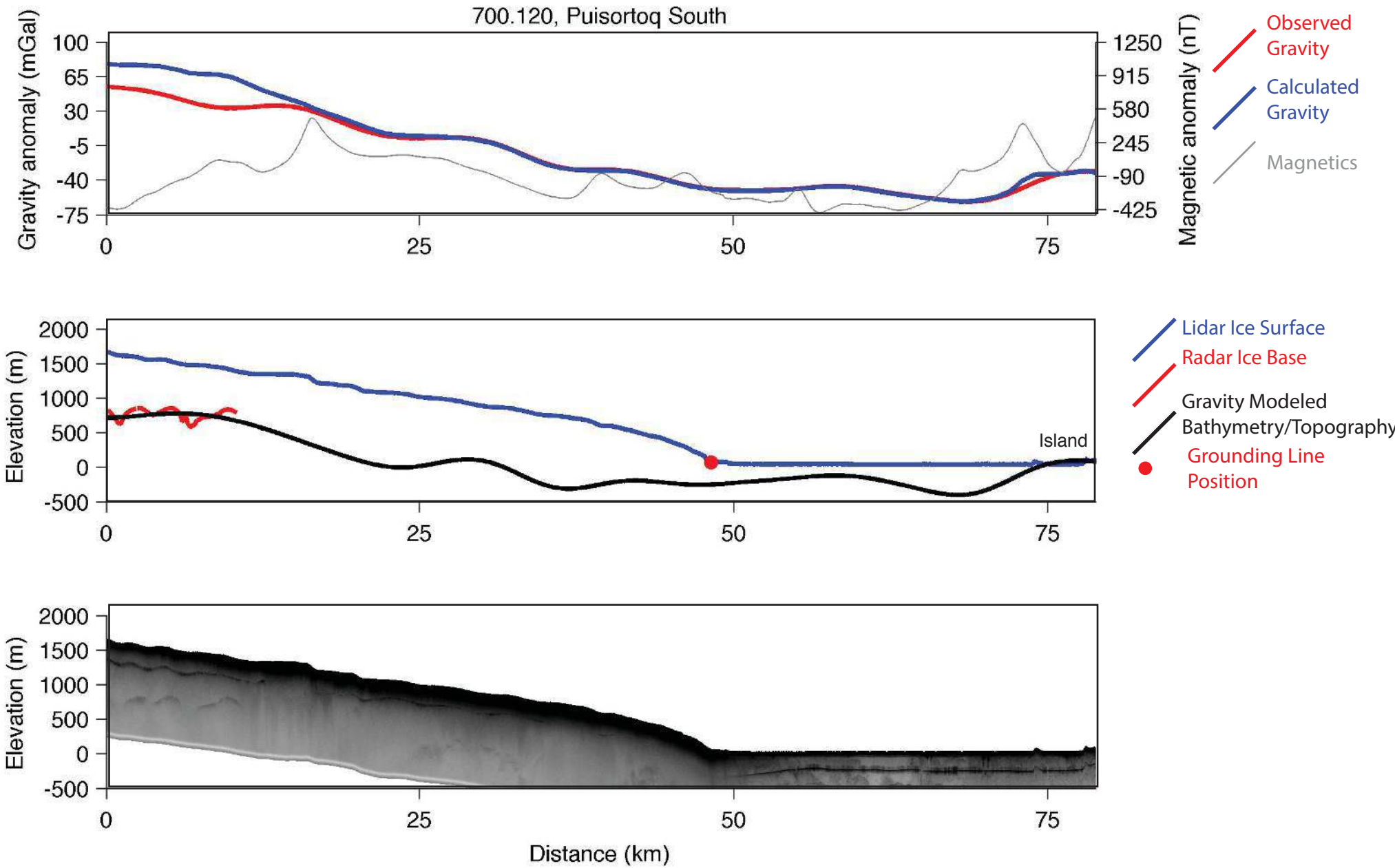
700.120, Puisortoq South
Gravity anomaly (mGal)
100
65
30
-5
-40
-75
0
25
50
75
Magnetic anomaly (nT)
1250
915
580
245
-90
-425
Observed Gravity
Calculated Gravity
Magnetics
Elevation (m)
2000
1500
1000
500
0
-500
Island
Lidar Ice Surface
Radar Ice Base
Gravity Modeled Bathymetry/Topography
Grounding Line Position
Distance (km)